Mechanics and Durability of Fiber Reinforced Porous Ceramic Composites

Xinyu Huang

Dissertation submitted to the Faculty of the
Virginia Polytechnic Institute and State University
in partial fulfillment of the requirements for the degree of

Doctor of Philosophy
in
Engineering Mechanics

K. L. Reifsnider, Chair
R. C. Batra
D. P. H. Hasselman
R. Heller
John J. Lesko

December 19, 2001
Blacksburg, Virginia

Keywords: Hot Gas Filters, Porous Ceramics, Ceramic Matrix Composites, Mechanical Properties, Micromechanics, Durability

Mechanics and Durability of Fiber Reinforced Porous Ceramic Composites

Xinyu Huang

(ABSTRACT)

Porous ceramics and porous ceramic composites are emerging functional materials that have found numerous industrial applications, especially in energy conversion processes. They are characterized by random microstructure and high porosity. Examples are ceramic candle filters used in coal-fired power plants, gas-fired infrared burners, anode and cathode materials of solid oxide fuel cells, etc. In this research, both experimental and theoretical work have been conducted to characterize and to model the mechanical behavior and durability of this novel class of functional material. Extensive experiments were performed on a hot gas candle filter material provided by the McDermott Technologies Inc (MTI). Models at micro-/meso-/macro- geometric scales were established to model the porous ceramic material and fiber reinforced porous ceramic material. The effective mechanical properties are of great technical interest in many applications. Based on the average field formalism, a computational micromechanics approach was developed to estimate the effective elastic properties of a highly porous material with random microstructure. A meso-level analytical model based on the energy principles was developed to estimate the global elastic properties of the MTI filament-wound ceramic composite tube. To deal with complex geometry, a finite element scheme was developed for porous material with strong fiber reinforcements. Some of the model-predicted elastic properties were compared with experimental values. The long-term performance of ceramic composite hot gas candle filter materials was discussed. Built upon the stress analysis models, a coupled damage mechanics and finite element approach was presented to assess the durability and to predict the service life of the porous ceramic composite candle filter material.

Acknowledgments

- My advisor, Dr. Kenneth L. Reifsnider, for presenting me challenging problems and giving me the freedom to tackle them in my own ways; and for all the advice, encouragement, and support through these years.

- Dr. Romesh C. Batra, Dr. D. P. H. Hasselman, Dr. Robert A. Heller, Dr. Jack Lesko, and Dr. Dean T. Mook, for taking time out of their busy schedules and serving on my committee.

- McDermott Technologies Inc. and Virginia Center for Innovative Technologies, for providing the financial support on this research.

- Dr. Rich Wagner and Mr. Rich Goettler at the MTI Lynchburg research center, for many helpful discussions on the "empty" composite material they created.

- Dr. Lorna J. Gibson, Professor of Materials Science and Engineering at Massachusetts Institute of Technology, for kindly granting the permission to use some of her experimental results on the honeycomb materials.

- Dr. Robert Carter, for performing the majority of the tube testing and SEM work.

- Dr. Scott Case and Dr. Howard Halverson, for many constructive discussions and advices on ceramic composites.

- Marshall McCord, Bob Simmonds, George Lough, and David Simmons, for their assistance with the experimental work.

- Shelia Collins, for taking care of many invisible chores in the office and keeping everything working smoothly.

- Loretta Tickle, for taking care of my academic record and keeping me from being "blocked" many times.

- Buo Chen, Jia Qi, Shu Guo, and Shuangyan Xu at the Adhesion Lab, for their friendship and many timely helps.

- The rest of the current and graduated MRG students: B. K. Ahn, Wenlung Liu, Michael Pastor, Blair Russell, Fred MacBagonluri-Nuuri, Nadia Obechu, Vinayak Pankey, Joe South, Aixi Zhou, Tozer Bandorawalla, Axinte Ionita, for their countless helps and advices.

- My parents, Guozhu and Xiujuan, for their enduring love and encouragements.

- My wife, Huiying, for her love and patience.

Contents

List of Figures

List of Tables

Chapter 1

Introduction

1.1 Porous Ceramic Composites

Porous materials refer to solids possessing pores. The porosity is the fraction of the pore volume to the total volume. Pores inside the solids can be classified into open pores and closed pores. Open pores are connected to the outside of the material surface and can be penetrated by fluids; closed pores are isolated holes. Porous materials with pore size ranging from sub-microns to sub-millimeters are routinely manufactured and used in various industrial applications. The application usually takes advantage of one or several of the following characteristics of porous materials:

- large specific surface area $\Longrightarrow$ catalyst bed for chemical reactions
- penetrable by fluids $\Longrightarrow$ filters
- poor conductor of heat and acoustic wave $\Longrightarrow$ thermal/acoustic insulation
- radiation properties resemble black body $\Longrightarrow$ radiant burner

In many applications requiring resistance to high temperature or resistance to aggressive chemical environments, only porous ceramics can be used or have a reasonable life expectancy. Porous ceramics are manufactured with similar processing routes as those of dense ceramics. Usually, the processing starts with ceramic powders or chopped ceramic fibers; they are mixed with various additives including plastilizers, pore forming agents (fugitive elements), and bonding agents; the mixed material is formed into the desired shape, called a green body or green compact; then it is fired; the powders and chopped fibers are sintered together, at the same time the fugitive elements are driven out, leaving distributed pores inside the volume. The morphology of the pores in the porous material can be modified by changing the size, shape of the starting powder or fibers; or the size, shape, and weight fraction of the fugitive elements. The orientation of the pores can also be changed in the shape forming process. For example, uniaxial compression of the green compact can cause pores to elongate and align in certain directions.

Monolithic porous ceramics are weak and brittle under tensile loading. They are also vulnerable to thermal shock. These insufficiencies have greatly limited the application of porous ceramic materials. The recent success in developing high strength, high stiffness ceramic fibers opens the door for the emergence of fiber reinforced ceramic composite materials. The introduction of strong ceramic fibers into the porous ceramics brings about three desirable reinforcing mechanisms—crack bridging, fiber sliding, and matrix crushing. Effective stress intensity factors around the micro/macro cracks are decreased because of the fiber bridging effect; as a result, the global strength is increased. In the failure process, more energy is dissipated because of the irreversible losses associated with fiber sliding and matrix crushing; as a result, the fracture toughness is increased.

Ceramic composites with high porosity have a variety of applications in modern industry. Coal fired power generation plants use porous ceramic tubes as a barrier filter to control particles in a hot gas stream. Porous ceramic panels are under development as gas-fired

infrared-emitters in the paper industry. Fibrous porous ceramic thermal shielding tiles are used on the space shuttle to protect the structure from overheating on reentry. Porous ceramic materials are used as filtration media for some highly corrosive molten metal/chemicals and porous conductive ceramics are used in solid oxide fuel cell (SOFC) as fuel and air electrodes. In the next section, the application of porous ceramics in hot gas filtration will be introduced in detail.

Porous ceramics or porous ceramic composites are characterized by random heterogeneous microstructures. The size, shape, spacial distribution, and orientation of pores are essentially stochastic. They can only be described by probabilistic distributions and spacial correlation functions. It is very tedious, if not impossible, to obtain the exact distribution function of these microstructure features. Effective properties of porous ceramic composites are of great technical interest in all applications. For example, knowing the stiffness and strength of porous ceramic filters are very important in the design against mechanical failures; the effective thermal expansion coefficients of the porous electrodes are required to match that of the electrolyte material in a SOFC to minimize thermal stresses. Currently, the only practical way to obtain these effective properties is through experiments. It is well known that the effective properties depend on the properties of the constituent materials and their microstructures. There is a lack of theoretical or numerical tools that can predict the effective properties of these porous ceramics composites based on the properties of the constituent materials and their microstructures. These tools are of great importance in guiding the material design and processing. One goal of this work is to fill in this gap by developing analytical and numerical tools for a specific class of porous ceramic composites.

Hot Gas Candle Filter

The author has investigated a novel porous ceramic composite hot gas filter material manufactured by McDermott Technology Inc. (MTI). In this section, a brief introduction is given to the MTI hot gas candle filters used in coal-fired power generation plant.

Coal-fired Pressurized Fluidized Bed Combustion (PFBC) and Integrated Gasification Combined Cycle (IGCC) power generation plants use hot gas filters to remove particles from the hot gas stream. A pressurized fluidized bed combustor produces a hot pressurized gas stream that expands through a gas turbine to generate power. This particulate-laden stream is generated by directly burning coal and other solid sorbent (e.g., limestone) in pressurized air. The particulates in the hot gas stream must be controlled to meet turbine protection specifications and particle emission regulations. Hot gas candle filters are used as barriers to screen out particulates in the hot gas stream before it hits the turbine. The required particulate size distribution in the outlet stream is typically 20 *ppmw*[1] for particles greater than 2 *microns* and less than 10 *ppmw* for particles greater than 5 *microns*. Besides this requirement, the pressure drop and temperature loss need to be minimized for efficiency considerations.

Figure 1.1 schematically illustrates the function of the hot gas filter and Figure 1.2 shows candle filter arrays arranged in modules in a power plant. During operation, dust particles accumulate on the outer surface of the candle filter; to remove these particles, a pressurized air stream is ejected from the inside of filter to the outside, i.e., reverse to the normal gas flow direction. This process is carried out periodically and is often referred to as back-pulse cleaning.

Hot gas candle filters are required to withstand an aggressive mechanical, thermal, and chemical environment. The basic service condition is summarized in Table 1.1. Additional

[1]Parts per million weight.

Table 1.1: Typical service environment of hot gas candle filters.

Service Temperature	870 °C(1600 °F)
ΔP (high pressure outside)	20-50 inches of water
Back-pulse pressure (high pressure inside)	5–10 psi
Mounting load (axial bolt load on flange)	1000–2000 lbf

load conditions include thermal shock during start-up, shut-down, and mechanical loads related to excessive dust accumulation and ash bridging. The hot gas filter must be able to withstand all of these possible conditions without fracture or other catastrophic failure. Another important performance requirement for candle filters is the durability or service life. The degradation of candle filter material is unavoidable due to high temperature exposure, chemical attack, repeated thermal shocks, and other mechanical loads. The knowledge of service life is critical for the safe operation of the power plant. Table A.1 in appendix A summarizes the short-term and long-term failure mechanisms and their sources.

Traditional clay-bonded monolithic filters often suffer from catastrophic failure. For this reason, recent attention has been focused on the development of ceramic composite filters, which have much better thermal shock resistance and damage tolerance. Ceramic composite hot gas filters are typically made by filament winding or braiding. The continuous fibers are used as reinforcements. The author has investigated a ceramic composite hot gas filter material developed by MTI. It is manufactured by a filament winding process, as shown in Figure 1.3. Nextel-610[2] ceramic fiber tows are wound on a mandrel with a $\pm$ 45° winding angle while a chopped Saffil[3] fiber slurry is sprayed on. The preform is then dried and fired to form a structure. The expanded tube flange is made by introducing a rolled filler at the open end of the filter tube. The MTI candle filter tube is 1500-mm long with a 60-mm outer

[2]A high strength, high stiffness, small diameter alumina fiber commercialized by 3M.

[3]A low grade alumina fiber commercialized by ICI.

diameter and a 50-mm inner diameter.

1.2 Mechanical Testing

Experiments are the primary means for the design and evaluation of porous ceramic composites. Many testing methods have been developed to study the the global response of porous ceramic composites under thermo-mechanical loading conditions. Some of the existing mechanical testing methods for ceramic candle filters are schematically illustrated in Figure 1.4.

To evaluate the mechanical performance of hot gas candle filters, Westinghouse [3, 4] developed a C-ring/O-ring tension and compression test, an internal pressure burst test, and a four-point bend test. The C-ring/O-ring test (Figure 1.4-a,b) is performed on either a 15-mm or a 25-mm wide ring segment with or without a 25-mm cutout. Load and deflection are measured. This test can be conducted at both room temperature and elevated temperature. In their internal pressure burst test (Figure 1.4-d), a water-filled bladder is inserted into a tube specimen, water is then pumped into the bladder until the specimen fails at a critical pressure level. To obtain creep properties, Westinghouse uses a 4-point bend test (Figure 1.4-c) on a slender bar cut from the wall of a filter tube. All of these methods have been used to evaluate both monolithic and composite candle filters. It needs to be pointed out that for composite materials, the specimen size in these tests is too small to allow the effective transfer of load from the matrix to the reinforcing phase; the resulting data might not reflect the actual strength of composite filter tube as an integral part.

Singh *et al* [57] studied fracture behavior of advanced ceramic candle filters. He developed a rubber plug internal burst test (Figure 1.4-e). A solid rubber plug in a cylinder shape is inserted into a segment of ring-shaped specimen. Pressure is then applied to the top and

bottom surface of the rubber plug. Under pressure, the rubber plug tends to expand circumferentially in order to maintain its volume. The ring segment imposes a hoop constraint on the rubber plug, so an internal pressure is generated. Compared to the water bladder technique, the rubber plug test is simpler to setup and is safer to run. But the rubber plug tends to induce an undesirable axial force due to the friction on the contact surface between the plug and the specimen. The axial friction may cause an over-estimation of the global Poisson's ratio.

Singh *et al* [57] also studied the effect of thermal shock and thermal cycles on the strength of ceramic candle filters. He heated a sealed filter segment to high temperature and then quenched it to 25 °C oil bath. The quenched specimens were then tested in diametral compression. The loss of strength was observed for some ceramic composite filters only when the temperature difference exceeds about 900 °C. Singh also evaluated the in-situ strength of the alumina reinforcing fibers of thermal-exposed and as-fabricated filter tubes by using a fracture mirror technique. The in-situ strength of Nextel-610 fibers in the exposed tubes was shown to be about 50% of the fiber strength in the as-fabricated tubes.

Chen *et al* [10, 11] developed a NDE technique to evaluate the status of a filter tube by measuring its free vibration response. The vibration signatures of the candle filter were used to quantify the structure stiffness, to assess the degradation levels, and to locate the damage sites. Finite element analysis was employed to obtain the theoretical modal information.

None of the above tests are standardized. Many of the reviewed experimental techniques need to be modified to deal with composite specimen. For necessary stress calculation, formulas with implicit isotropic assumptions were often used for anisotropic composite specimen. Widely scattered property data have been reported for one material system using these testing techniques.

1.3 Hierarchical Modeling

Composite material systems usually have hierarchical micro-structures. The mechanical behavior of such a material system is determined by the response of its constituent materials and their interactions at a number of geometric scales. For example, the global failure behavior of dense CFCCs has been shown to highly depend on the nature of the fiber-matrix interface/interphase at the microscopic scale. Strong fiber/matrix bonding promotes brittle failure modes, while a weak bonding promotes less brittle failure modes characterized by fiber pull-out and fiber sliding. These interactions need to be modeled to fully understand the material response of a composite material system and to help design the composites to achieve an optimum mechanical performance at a given cost.

For complex composites, it is generally impractical to perform an analysis on a "flat" model incorporating the architectural information of all hierarchies. The prevailing strategy for modeling such a material system is a multilevel "abstraction", in which models are built according to some abstract structural hierarchy. Lower level models generate material properties, which are used by the high-level models. For example, in classical laminate theory [33, 28], a laminated plate is naturally decomposed into a series of lamina, which is assumed to be a homogeneous layer of orthotropic material, the elastic properties of a lamina can subsequently be estimated as functions of fiber and matrix properties using micromechanics models such as the rule of mixture, the concentric cylinder model [23, 25], the cell model [1], etc.

For composite materials with more complicated microstruture, for example, 3D braided composites and woven composites, the structural hierarchy may not be as obvious as that in a laminate and there could be more than one way to decompose the structure into several geometric levels; how to choose and how to interface between levels of models are matters of engineering judgment. Nakai and Hamada, *et al* [41, 16, 17] analyzed a braided composite

tube. Their objective was to reveal the relationship between the braiding structure and the torsion stiffness, and the dependence of the bending properties on the damage state inside the tube. They modeled the braided composite at five levels: fiber bundle model, cross part model, weaving structure model, basic structure model, and structural model. Tan *et al* [61] proposed a 3D multi-scaled modeling technique for predicting the linear elastic properties of open-packing woven fabrics. A number of 3D macro and micro blocks were included in the model. Dimitrienko [18] proposed a hierarchical model to evaluate high temperature mechanical properties of a composite material. The composite material was divided into six structural levels, which included matrix block, monofibre, micro composite, UD material, layer with curved fiber, and layer. Elastic properties and coefficient of thermal expansion (CTE) were calculated by averaging elastic constants and CTEs of constituent blocks.

Although there may be many different ways to break a composite material into structural hierarchies. The models are typically classified into three categories, i.e., the micro-, meso-, and macro- mechanics models. The macro-mechanics model deal with component (coupon) level entities, and micromechanics model concerns entities about the size of reinforcing fibers. Usually, the modeling of entities in between micro- and macro-scale is named meso-mechanics, for example, the fiber tows and yarns in the textile composites.

The MTI ceramic composite candle filter material has a natural hierarchical structure shown in Figure 1.5 as a result of the MTI vacuum winding process. The author has attempted to model this composite material system at three levels. At the macro-level, technical beam theory was used to estimate the transverse vibration frequencies of the candle filter. At the meso-level, an energy method and finite element analysis were used to get effective tensile, torsion, and flexure stiffness of the filter tube. At the micro-level, a bonded fibrous network model was used to estimate the effective properties of the chopped fiber matrix; a unidirectional composite model was used to estimate the effective properties of the fiber tows. Each model utilized effective properties provided by the lower level models. The complex

modeling task was thus divided into smaller problems, which were dealt with separately.

1.4 Statement of Problems

The author conducted research on porous ceramics and porous ceramic composites, specifically the MTI ceramic composite candle filter material with the following goals:

1. To characterize the stiffness and strength of the MTI ceramic composite hot gas candle filter material.
2. To investigate mechanics modeling approaches for highly porous materials with stochastic microstructures, and their composites.
3. To investigate modeling approaches to address the durability and life prediction problems associated with porous ceramic composites.

Porous ceramic composites are usually multi-functional materials. Some are used as barrier filters, others are used as catalyst beds, some are used as porous electrodes. In these cases, their primary performances are measured by permeability, surface area, and conductivity, etc. Besides these functional performance metrics, their stiffness, strength, and mechanical durability are also critical to the safe and cost-effective operation of the functional material systems. The goal of our research was to develop a methodology to determine and to predict the stiffness, strength, and life of these porous ceramic composites. In order to perform a stress analysis, stiffness of the porous ceramic composites has to be determined either by experiments or by analytical models and results need to be translated into tensor values. To tackle the durability problem, various degradation mechanisms need to be determined by experiments and quantitatively modeled to make the life prediction. To accomplish these tasks, the research was conducted in a natural progression listed below:

1. Conducting mechanical experiments on both as-fabricated and thermal-cycled tube specimens, collection of stiffness data and identification of failure modes.

2. Development of analytical and numerical modeling techniques which incorporate necessary micro-/meso-structure information.

3. Identification of damage mechanisms of the MTI composite candle filter material and development of modeling techniques capable of incorporating various sources of material degradation.

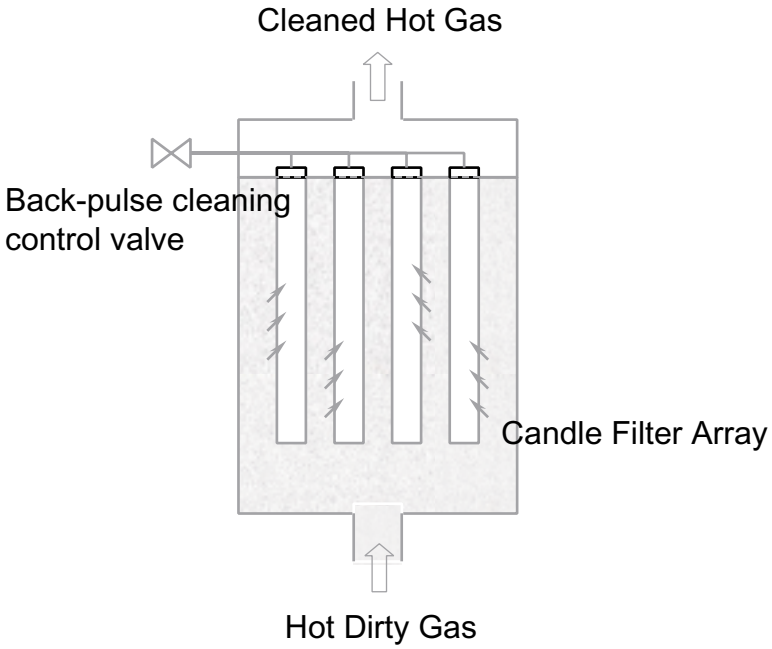

Figure 1.1: Schematic of candle filters at work.

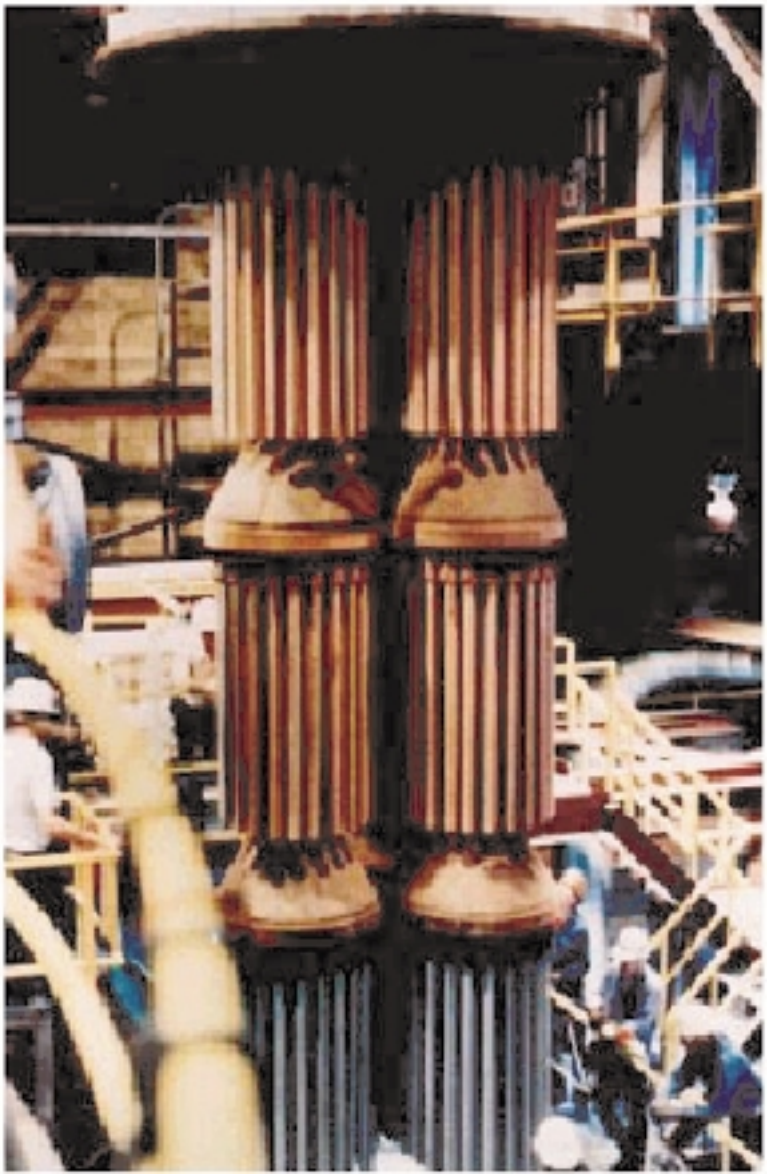

Figure 1.2: Westinghouse advanced particle filter system at the Tidd Pressurized Fluidized-Bed Combustion demonstration facility in Brilliant, Ohio. [59]

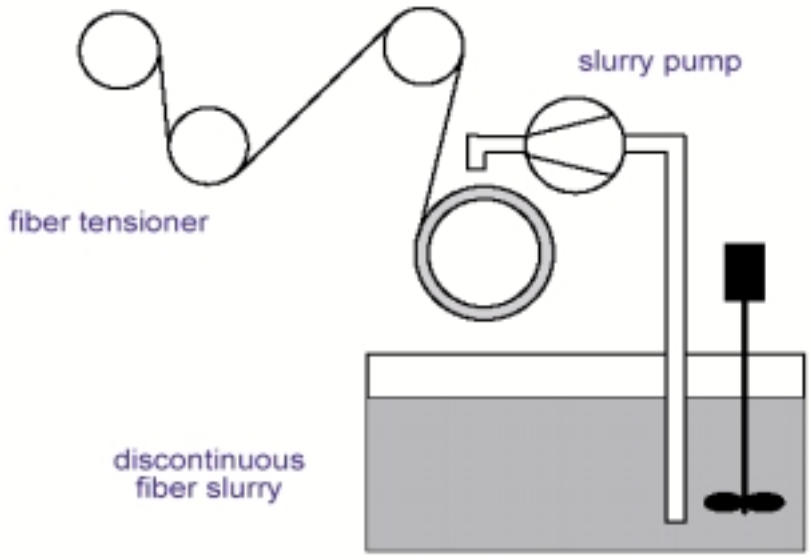

Figure 1.3: Schematic of the MTI vacuum winding process. [66]

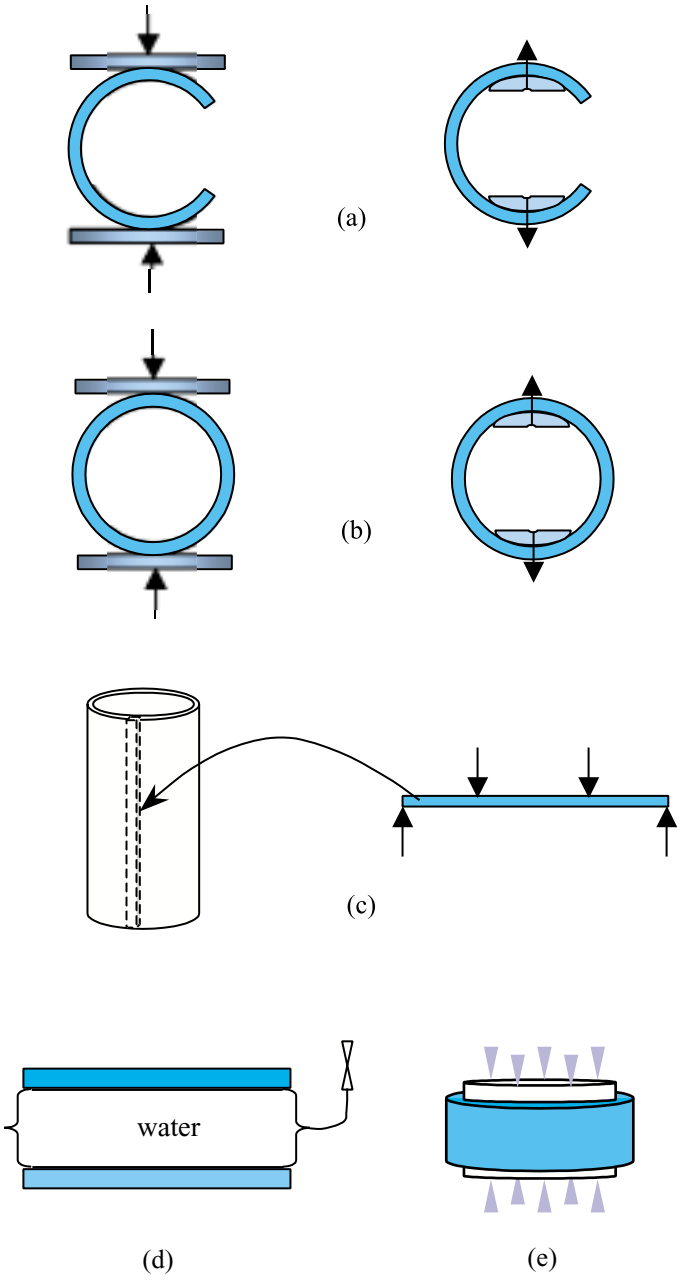

Figure 1.4: Mechanical testing methods applied to hot gas candle filters.

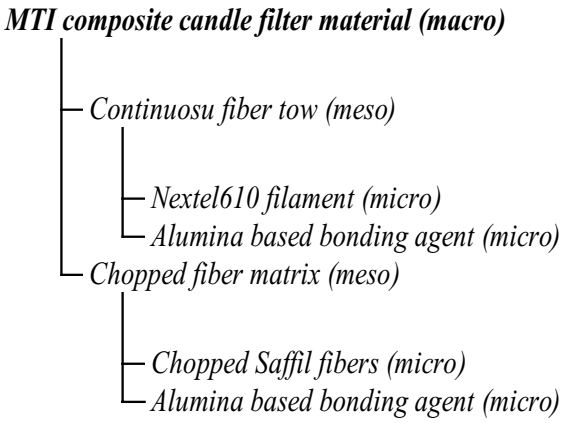

Figure 1.5: Hierarchical structure of the MTI composite candle filer material.

Chapter 2

Experimental Characterization

The objective of experimental characterization is two-fold: firstly to measure the stiffness of a composite material and secondly to identify its failure modes and their associated critical load levels. Extensive tests were performed on the MTI hot gas candle filter material at room temperature and elevated temperature. Tests were also performed on thermal-cycled[1] specimens to investigate the effect of repeated back-pulse cleaning cycles on the mechanical properties of the MTI candle filter material. Functional porous ceramic composites possess several distinctive features compared with structural materials, proven experimental techniques applicable to structural composites sometimes cannot be applied directly to the porous material; special treatments are needed during several testing stages, such as sample preparation, strain measurement, and result interpretation. The author and his co-workers have devised a number of experimental techniques to characterize porous ceramics composites. The details are presented in following sections. Test results for the MTI candle filter material are tabulated and discussed in Section 2.2. Scanning electron microscopy (SEM)

[1]Refers to a simulated back-pulse cleaning cycles. The temperature of the back-pulse steam is significantly lower than the temperature of the specimen; as a result, the specimen experiences repeated thermal transients.

investigations were performed on the MTI candle filter material to obtain its microstructure information, the SEM procedure and results are summarized in Section 2.3.

2.1 Experimental Techniques

Porous ceramic composites are a novel functional material; mechanical testing methods for this type of functional material have not been standardized. A variety of experimental methods have been developed by several material manufacturers and a number of private research institutions. They are reviewed in Section 1.2. The author has adopted some of the existing techniques and made improvements on these methods in order to obtain objective material responses.

Functional porous ceramic composites are different from structural composites in many ways. Firstly, porous ceramics are considerably weaker and more brittle than most structural materials, so that typical gripping methods used on structural materials would inevitably cause the local material to collapse near the gripping site. Reinforcement of the gripping section and the loading section are required to ensure the desired uniform load transfer from the actuator to the bulk of the specimen. Secondly, fiber reinforced porous ceramics composites show significant "edge effect" because of the ineffectiveness of load transfer between the reinforcing fiber and the highly porous matrix phase.[2] Cutting of such materials is unavoidable in preparing test samples but it needs to be minimized and the cut section needs to be set far enough away from the gage section. For the same reason, it is impractical to cut these composite materials into small test coupons; in such cases, the load transfer between the matrix and the reinforcements may not even occur and the material behavior would be completely different from the un-cut composite behavior. And thirdly, the use of regular

[2]This is partly due to the large difference in modulus and strength between reinforcement and the porous matrix.

adhesive to bond foil strain gages to the surface of the porous ceramic specimen was shown to cause problems. The adhesive infiltrates into the bulk of the micro-porous specimen near the strain gage and forms a chunk of material that is stiffer and stronger than surrounding materials. This results in an over-estimation of the stiffness and may also create artificial failure modes. The extent of such "local reinforcing effect" needs to be assessed to ensure objective interpretation of the test data based on the regular strain gage measurements.

In characterizing the MTI ceramic composite candle filter material, the author and his co-workers have devised a number of experimental techniques to test the tubular-shaped candle filter specimen. According to the applied loading conditions, these tests can be classified into three types: internal pressure test, axial loading (tension/torsion) test, and bend test. They are discussed in details in following sub-sections.

2.1.1 Internal Pressure Test

To generate an internal pressure, a pressurizing medium is required. The most commonly used pressurizing media are fluids, such as water and oil. Deformable solids, such as elastomer's, can also be used. The use of a solid pressurizing medium eliminates the sealing problem encountered when using fluids as the pressurizing media. Also, the test can be run with only a regular load frame without the requirement of complicated fluid pumps, valves, and pressure gages, etc. The downside of using solid media is the undesirable frictions that are induced between the pressurizing medium and the specimen. This friction may result in a non-uniform distribution of the internal pressure.

For its simplicity, the author has used a rubber plug to generate the internal pressure. Figure 2.1 shows our testing configuration. A rubber plug is inserted into a tubular specimen and is compressed axially by two plungers that are driven by the actuator on a loading frame; the rubber plug expands radially due to Poissons effect and the enclosing tubular specimen

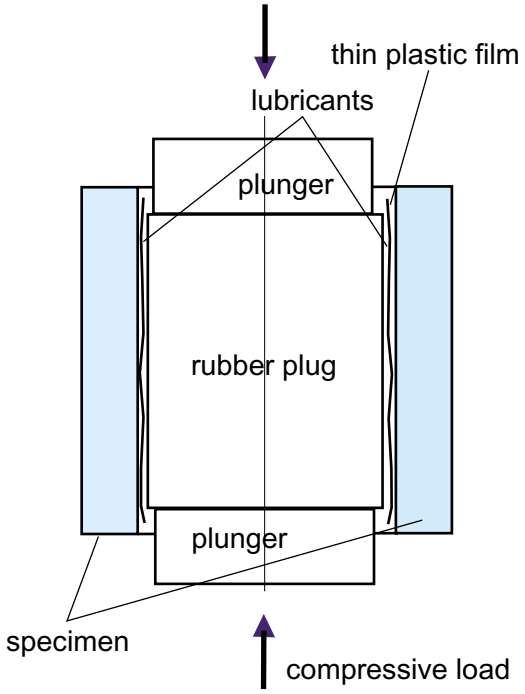

Figure 2.1: Schematic of the rubber plug test setup.

prevents the rubber plug from free expansion and thus an internal pressure is generated. To minimize friction between the rubber plug and the internal surface of the specimen, the author applied a lubricant[3] between the rubber plug and the specimen, a thin plastic film is used to isolate the lubricant and to prevent it from contaminating the specimen. By monitoring the applied load and the axial deformation of the rubber plug, the pressure on the inner surface of the ring can be estimated by the following equation:

$$p_i = \frac{p_a - E_r \epsilon_z}{2\nu_r} \tag{2.1}$$

where p_i is the internal pressure exerted by the rubber plug on the ring, p_a is the applied axial pressure on the top and bottom surface of the plug, E_r, and ν_r are the Young's modulus and Poisson's ratio of the rubber plug, and ϵ_z is the axial strain of the plug. ϵ_z can also be calculated from apparent modulus E_a and applied pressure p_a by the following equation:

$$\epsilon_z = \frac{p_a}{E_a} \tag{2.2}$$

Substituting equation 2.2 into equation 2.1, p_i yields:

$$p_i = \frac{1}{2\nu_r}\left(1 - \frac{E_r}{E_a}\right) p_a \tag{2.3}$$

The plug material was made from Silastic T-2 silicone rubber[4]. It was cast into a cylinder shape by using a Plexiglas (PMMA) mold. To determine the elastic properties of the rubber plug, the author tested it under compression in displacement control and measured the hoop and axial strains on the surface of the plug. The result is shown in Table 2.1. Several test runs were performed using four different loading rates and with lubricated[5] and un-

[3]Liquid soap.

[4]A two-component, high strength, silicone mold-making rubber from Dow Corning.

[5]To lubricate the contact surfaces between rubber plug and steel compression platens

Table 2.1: Elastic properties of the Silastic T-2 rubber plug.

without end lubrication					
cross-head rate (mm/min)	2	3	5	10	average
Young's modulus (psi)	301.24	301.62	303.27	305.65	302.95
Poisson's ratio	0.47	0.4612	0.4599	0.4602	0.463
with end lubrication					
cross-head rate (mm/min)	2	3	5	10	average
Young's modulus (psi)	294.57			299.31	296.94
Poisson's ratio	0.4416			0.4467	0.444

lubricated ends. The Young's modulus and Poisson's ratio were calculated. It was found that the Young's modulus and Poisson's ratio of rubber plug does not change significantly with cross-head rates from 2 mm/min to 10 mm/min, the typical range of loading rates in quasi-static test. The Young's modulus and Poisson's ratio decrease a little when using lubricated plug ends.

Tubular samples with 1-in, 2-in, and 3-in length were tested. The rubber plugs used for each sample size were a little shorter than the sample length to avoid over-loading the free edge. Tests were conducted on MTS and Instron load frames under displacement control. Load and displacement were recorded. On some specimens, foil strain gages were used to measure strains on the surface.

2.1.2 Axial Loading Test

A large number of quasi-static tension/torsion/compression tests on approximately 7-in long tube segments were performed to generate a base material property dataset for the MTI

candle filter material. Axial loading tests were also performed on thermally-cycled samples to assess the effects of back-pulse cleaning cycles on the mechanical properties. Hoop and axial strains on the tube outer surface were measured by both extensometer and strain gage.

test sample design

A schematic of the axial test sample is shown in Figure 2.2. The fixture on the MTS system used two pins to load the sample. The two pins were arranged perpendicularly to minimize bending moment induced by potential grip misalignments. Two methods have been used to create a uniform load transfer from the pin to the sample test section. First, a ceramic foam end plugs were inserted into and bonded to the two ends of the sample at its inner surface using high temperate cements. This helped the load to be evenly distributed and to reduce the notch effect of the pin hole. The second method was to pot the ends of the sample with epoxy. The potting epoxy infiltrated into the bulk of specimen at the two ends and essentially eliminated the notch effects of the pin holes. It also helped distributing applied load more uniformly in the test section.

strain measurement

Two methods were used to measure the strain on the outer surface of the tube. Strain gage rosettes were used to measure and calculate strain in several different directions, while extensometers were used to measure strain that is not affected by local reinforcement problems. The strain gages were bonded to the surface using the M-bond adhesive system supplied by the Micro-Measurements Group. Due to the porous nature of the material, instead of the recommended procedure, a different procedure contrived by Robert Carter was used. In the modified procedure, the catalyst, rather than being applied to that gage itself, is dropped onto the material. The adhesive is placed in a thin layer on the back of the gage. The

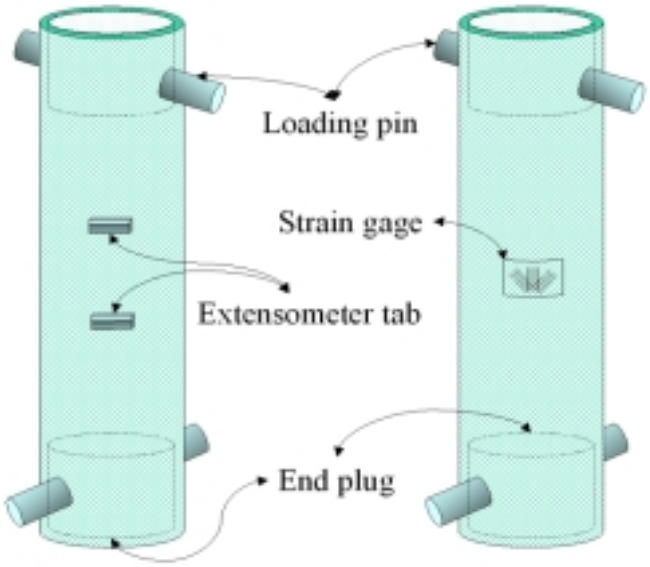

Figure 2.2: Schematic of tube samples for axial loading tests.

advantage of the modified procedure lies in that the adhesive will not be able to permeate deep into the filter material due to the catalyst content. This would help minimizing the penetration depth and still allow for a good bond to the sample. Extensometers were used to measure axial stiffness without the local effects caused by an adhesive. The tabs (see Figure 2.2) were bonded onto the surface of the filter using a silicon rubber cement giving a 25-mm gage length. Since the material is uniform between the extensometer tabs, this allow for more accurate measurement of the axial strain.

test procedures

To obtain tube tension and torsion stiffness, uniaxial tension and torsion tests were performed. The load used in most axial tests was -222 to 444 N. Torque limits were set to be $\pm$ 11.29 $N \cdot m$. To find the axial strength of the filter material, the MTS controller was

programmed to run in displacement control up to 6.25-mm at 0.0125 mm/s. The range was controlled by the length of the tube since the load frame is close to its maximum range due to a secondary actuator system. The loading rate used was very low to give the data acquisition systems enough time to sample data prior to the initial failure.

2.1.3 Bend Test

During operation, candle filters are clamped onto a flat tube sheet by their open ends—the flanges, as shown in Figure 1.1 and 1.2. This configuration resembles a cantilever beam in a structural sense. It is likely that filter tubes are loaded in bending during installation and maintenance. Besides, ash accumulation and bridging could also cause a side load on the tube. Because of the slender cantilever configuration, a small side load near the tip of a filter will generate a large bending moment at its fixed end. It is important to know the bend failure mode and the critical bend failure moment of the candle filter tube to ensure that it has enough strength to survive any potential side loadings.

Three types of bend tests were performed to evaluate the bend failure modes and critical bend failure moments: the 3-point bend test on 7-in tubes, the cantilever bend test on 18-in tubes with flanges, and the 4-point bend test on 14-in tubes.

three-point bend test

The 3-point bend test configuration is shown in Figure 2.3. To avoid local crushing at the loading and supporting points, three Plexiglas (PMMA) disks were inserted inside the tube at the three locations where concentrated loads were applied, two outside supporting points were hardened with potting epoxy. An extensometer was used to measure the strain at the point with the maximum tensile stress.

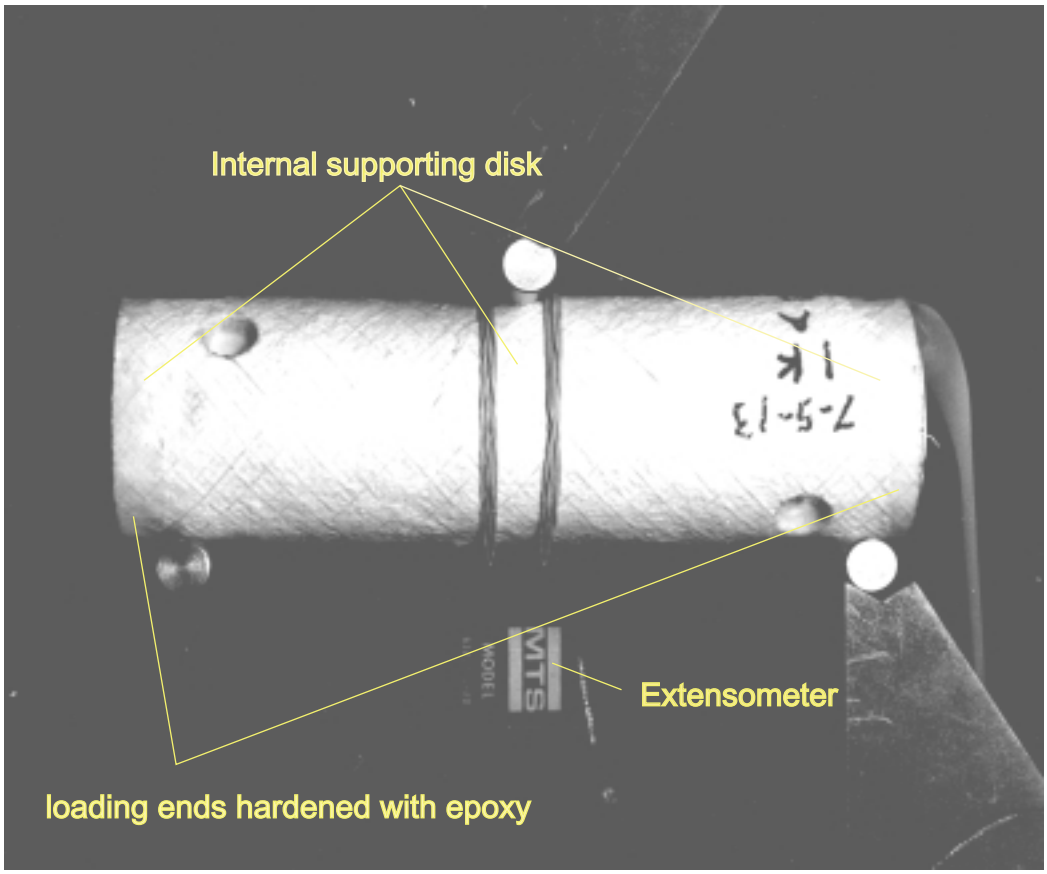

Figure 2.3: Configuration of the three-point bend test.

The test was performed on an Instron load frame under displacement control. The loading rate was 2-mm/min; load, displacement, and axial strain at the center of the specimens were recorded.

cantilever bend test

Cantilever bend tests were performed on 18-in tubes with flanges. Cantilever bending is the most severe case among all possible loading conditions in operation. The test configuration is shown in Figure 2.4. A tube sheet was clamped onto one of the posts of a testing frame. The tube specimen with flange was bolted on to the tube sheet. The bolt force was controlled to

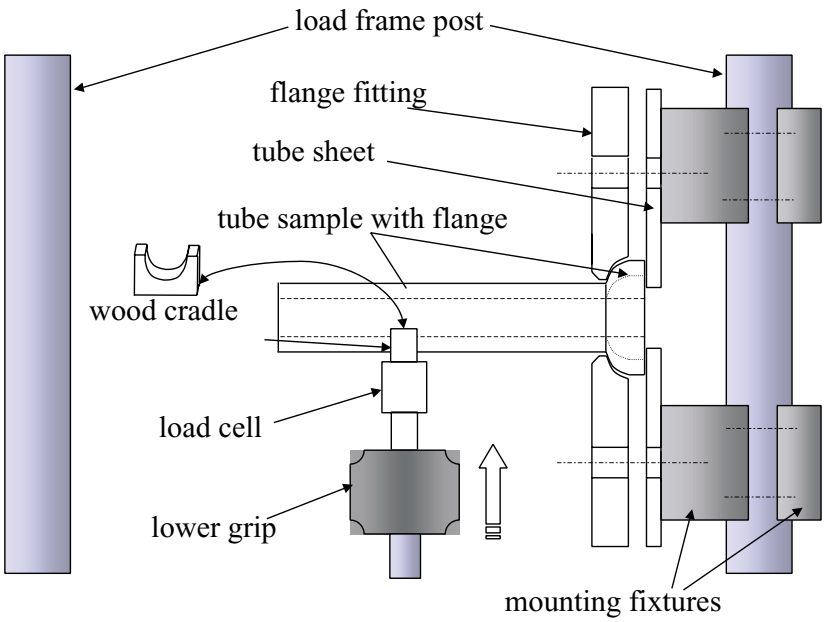

Figure 2.4: Configuration of the cantilever bend test.

be approximately 60-$in \cdot lbf$. The specimen was loaded by the lower grip with a home-built load cell. In order to avoid local material crushing at the loading point, a piece of wood cradle with a concave surface that matches the tube diameter was put in between the specimen and the load cell. The loading point was approximately 8 inches away from the clamping collar. Tests were performed under displacement control; load and actuator stroke were recorded. A total of three samples were tested. They were one as-fabricated alumina-bonded sample, one as-fabricated phosphate-bonded sample, and one thermally-aged sample.

four-point bend test

Four-point bend tests were performed on 14-in tube samples at room temperature and elevated temperature. A high temperature bend testing rig was designed and built in our material testing lab. The schematic of the system is shown in Figure 2.5. It consisted of following components: a temperature feedback controller, three heating elements, a water

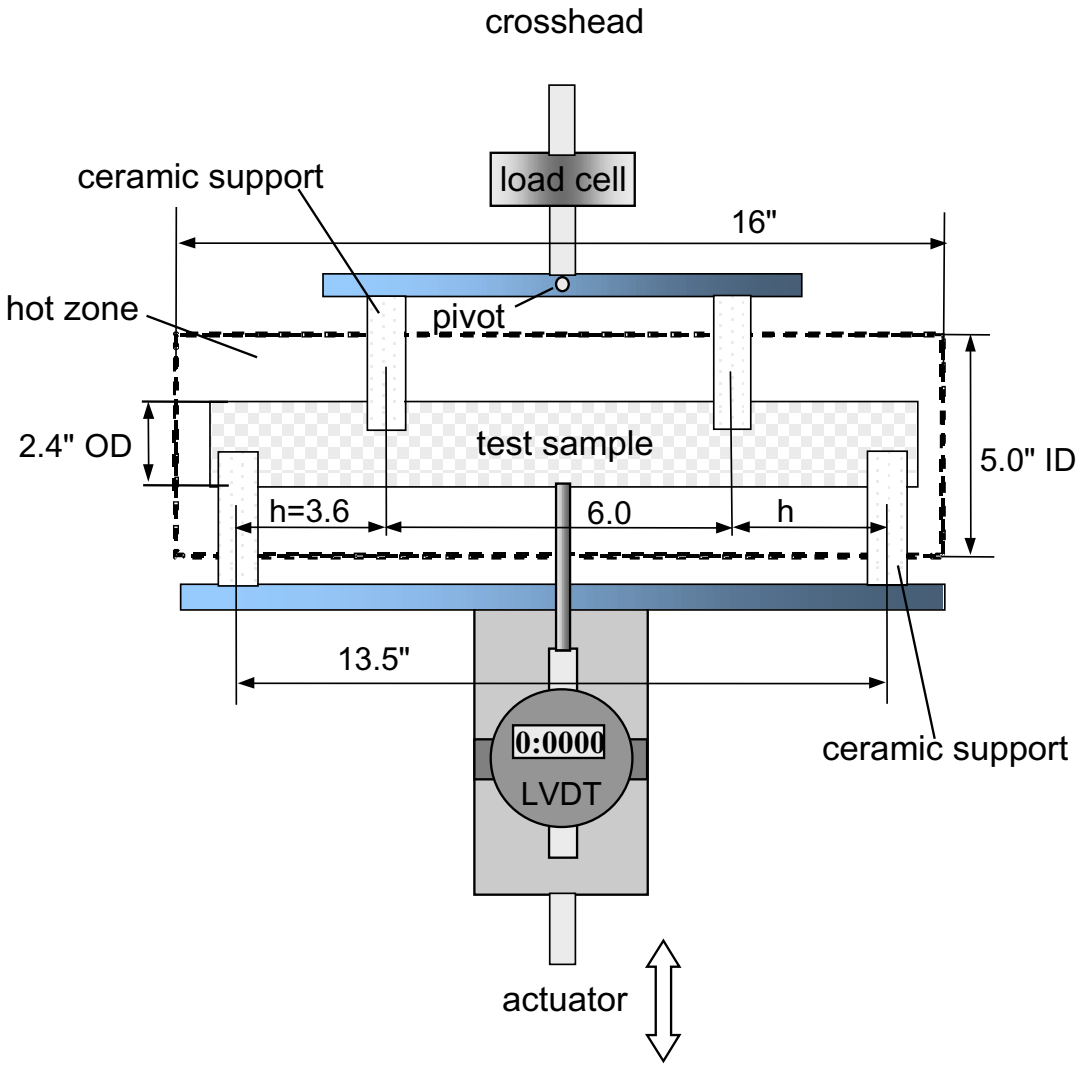

Figure 2.5: Configuration of the four-point bend test.

cooling system, ceramic felt insulations, ceramic loading and supporting cradles, a digital indicator, and a computer data acquisition system. The structural elements and their dimensions are also shown in Figure 2.5. The loading and supporting cradles were made of ceramic foam, which maintains its mechanical properties at temperatures well above 1500 °C and is also easily carved into any desired shape. A digital indicator[6] with a resolution of one

[6]Mitutoyo IDF-150E

micron was rigidly mounted on the lower loading fixture to measure the center deflection of the tube specimen. The deflection and load data were recorded by a computer. The testing rig was mounted on a MTS-810 servo-hydraulic material testing frame.

The filter tube specimen is 355-mm (14-in) long and has an OD of about 60-mm. To avoid the local collapse of the material at the loading and supporting points, we reduced the contact stress at those areas by machining the loading and supporting cradles to a 61-mm ID and a 25.4-mm width.

The center deflection measured by the digital indicator includes the contribution of the lower loading fixture (the lower metal piece and ceramic supports shown in Figure 2.5) because of its finite rigidity, which has to be taken into account. To assess the compliance of the lower loading fixture, we tested a thick walled cast iron tube on the bend fixture. The bend stiffness of this dummy tube was estimated to be about thirty times greater than that of our specimen. This test result was used to calculate the compliance of the lower loading fixture. In later data reductions, we used this compliance value to subtract out the contribution of the lower loading fixture. Before testing, the rig was heated to the specified temperature and held for about 15 minutes for the whole system to settle down to a steady state. In the quasi-static tests, a load profile consisting of several repeated ramp cycles was then applied with a loading rate about 16-N/sec. In the bend to failure test, displacement control was used instead of load control.

2.2 Experimental Results and Discussion

Experiment results for internal pressure tests, axial loading tests, and bend tests are presented and discussed in following sections.

2.2.1 Burst Test Result

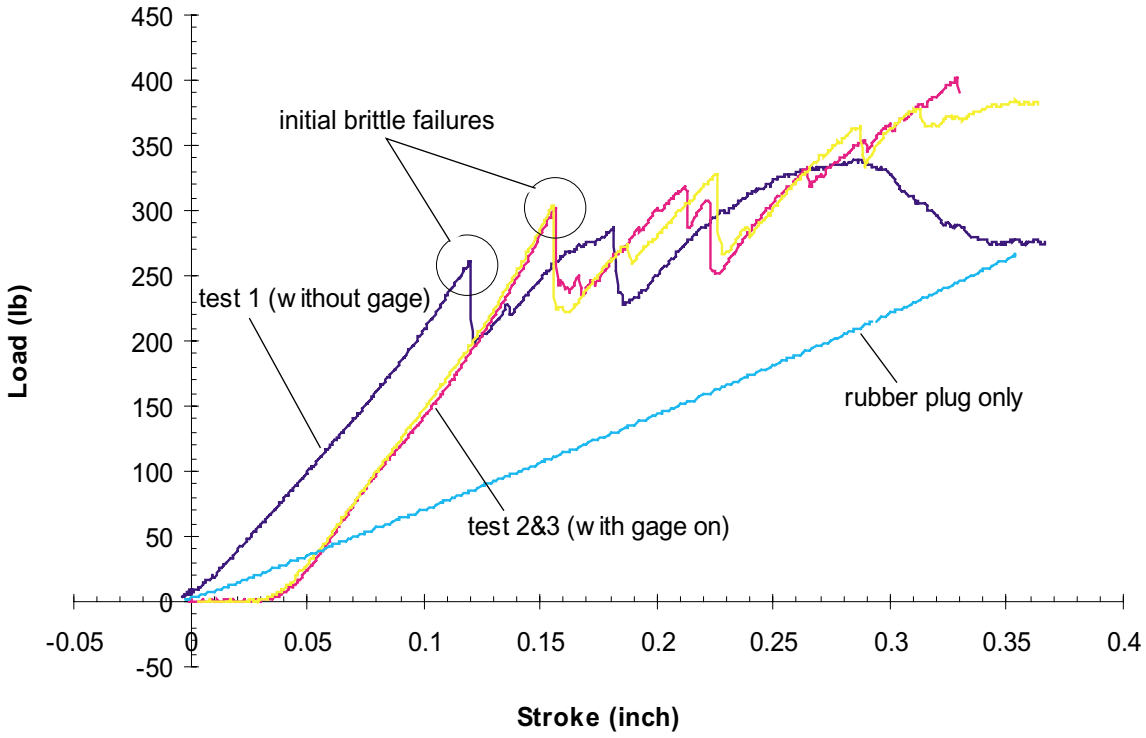

Figure 2.6: Typical burst test result: load v.s. displacement.

A typical load-displacement curve for an 1-*in* long sample is shown in Figure 2.6. The load displacement response is close to linear until the first sudden almost vertical load drop indicating a brittle damage event. The installation of a strain gage raises the critical load corresponds to the first damage events and this is clearly shown in Figure 2.6. With continued loading, more damages occur and the curve shows irregular fluctuations. A typical load-displacement curve for a 3-*in* long sample is shown in Figure 2.7. The overall behavior is non-catastrophic and significant amount of energy is dissipated.

Pictures shown in Figure 2.8 to 2.10 captured the failure sequence of a 3-*in* sample in an internal pressure test. All pictures were taken after the initial damage event (load drop). Initially, two cracks were identified: one crack started from the free edge and propagated

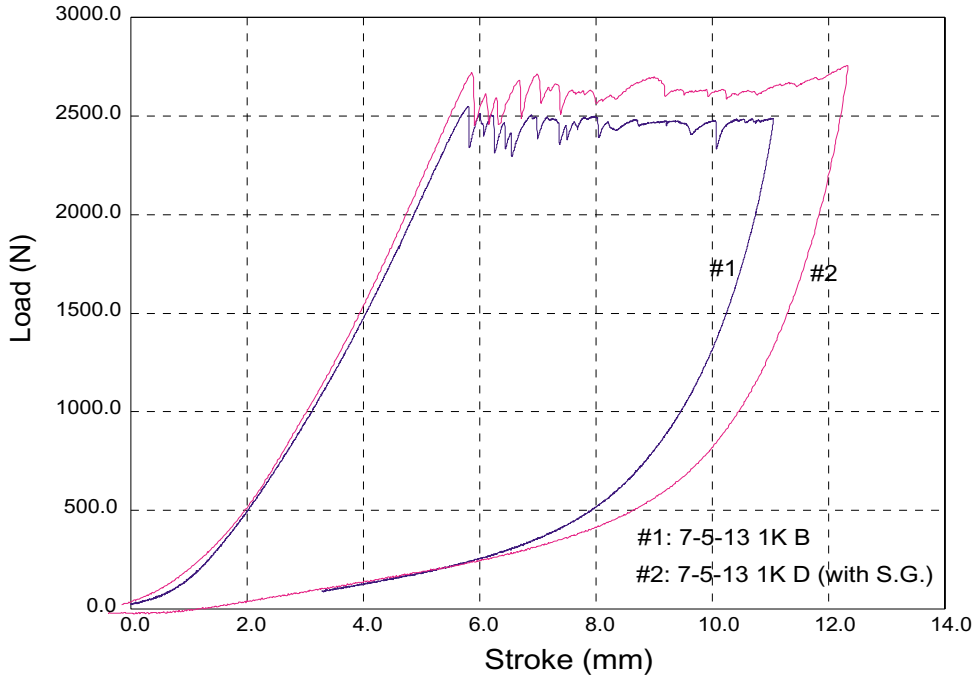

Figure 2.7: Burst test results on 3-in samples: load v.s. displacement.

along the direction of fiber tows, the other crack oriented roughly perpendicular to the previous crack and extended through the loaded section. Matrix material chipped off along the two cracks. At the later stage, matrix material chipped off from multiple sites distributed on the outer surface and more cracks formed and fiber tows debonded and fell off the surface.

All burst test results are tabulated in Table 2.2. It shows that the burst pressure strongly depends on the length of the test sample. The burst pressure v.s. sample length is plotted in Figure 2.12. Short specimens gave much smaller burst pressures than specimens that are twice or three times as long. On the cut surface, the axial stress in the fiber tow is zero; the stress increases with increasing distance from the surface by load transfer from the matrix material. It takes a certain length for a fiber tow to pick up full axial stresses because of "shear lag". This renders an ineffective load carrying region near the cut surface. For short specimens, this ineffective region is a higher percentage of the total specimen volume which

Figure 2.8: Failure sequence in a burst test: No. 1

Figure 2.9: Failure sequence in a burst test: No. 2

Figure 2.10: Failure sequence in a burst test: No. 3

Figure 2.11: Failure sequence in a burst test: No. 4

Table 2.2: Internal pressure burst test results.

I.D.	cycles	length (mm)	burst load (N)	burst pressure (MPa)	strain
7-2-28	0	25	1164	0.372	
7-2-28	0	25	1347	0.449	s.g.
7-2-28	0	25	1349	0.456	s.g.
7-5-13-B	10^3	76	2540	1.090	
7-5-13-D	10^3	76	2720	1.183	s.g.
7-6-12-H	10^4	51	1889	0.697	
7-6-12-B	10^4	76	2266	0.977	
7-6-12-D	10^4	76	2348	1.067	s.g.
7-6-12-F	10^4	76		1.154	s.g.
7-6-12-G	10^4	76		1.193	s.g.
7-6-16-B	10^5	76		1.138	s.g.
7-6-16-D	10^5	76		1.127	s.g.
7-6-16-H	10^5	76		1.055	s.g.

causes a lower nominal burst strength.

2.2.2 Tube Axial Test Result

A typical tensile load-displacement curve is shown in Figure 2.13. Again, the response is almost linear before the first damage event. Then the material stretched out to about 5 mm and still did not break into two parts, which is phenomenal for a material that is entirely made of ceramics.

Two failure modes were observed. The first failure mode (see Figure 2.15) is characterized

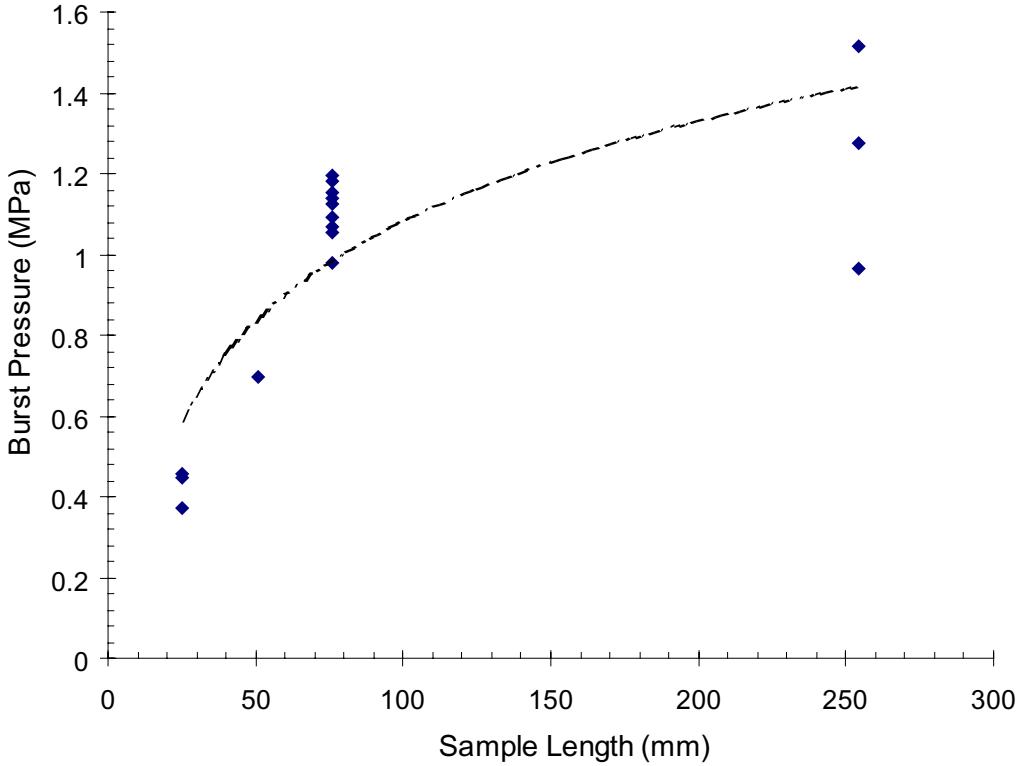

Figure 2.12: Dependence of burst pressure on sample length. The last three data points correspond to a 250-*mm* sample length were bladder test results reported by Alvin [4].

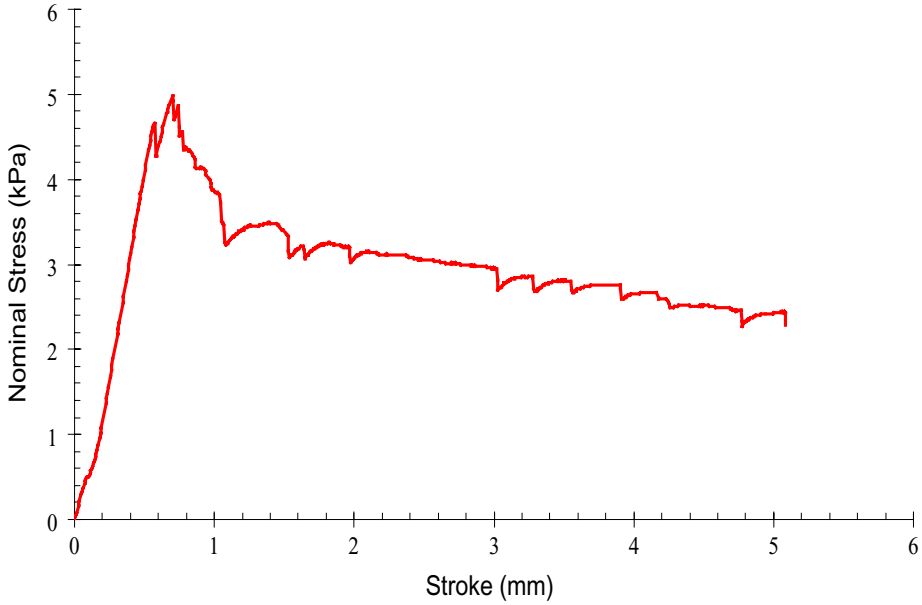

Figure 2.13: Typical load v.s. displacement curve of a tensile test.

by matrix crushing, tow scissoring, and the necking at the gage section of the sample. The second failure mode (see Figure 2.16) is characterized by long localized spiral crackings. The author also noticed that the first mode tends to occur when the sample is prepared with epoxy potted end and the second mode tends to occur when bonded ceramic foam ends are used. And the critical load associated with the first failure mode is consistently higher than the critical loads associated with the second failure mode, as shown in Figure 2.14. The ceramic foam end plug only bonded with tube internal layers; the epoxy potted end plug actually bonds all of the layers together near the tube ends. This is one of the reason why the strength of the tubes with epoxy end plugs were found to be higher than the strength of those tubes with ceramic foam ends.

All axial test results are summarized in Table 2.3. The columns are the average stiffness value for tension, compression, and torsion measured by strain gage (SG) and extensometer (Ext). The tubes are identified in two different ways, tube ID and tube number. Tube

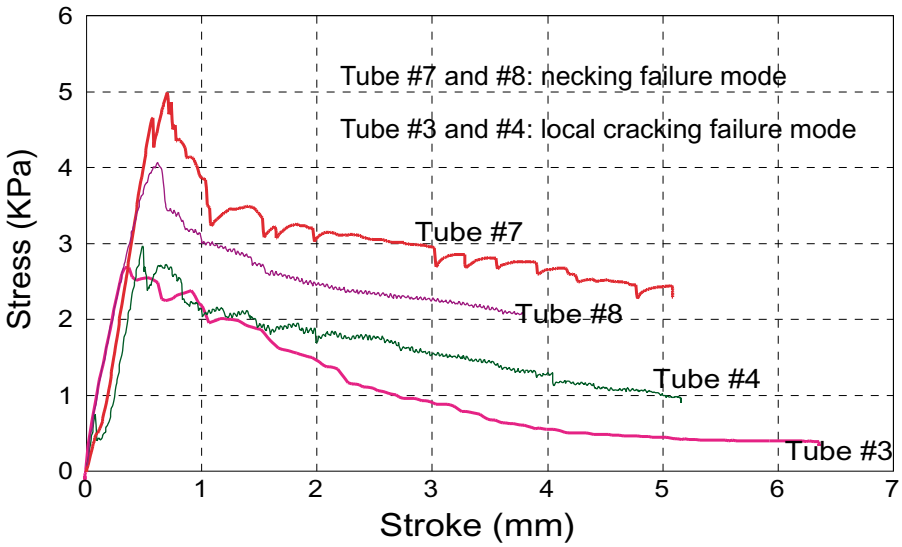

Figure 2.14: Tube tensile test results: stress v.s. stroke

number is the local system of identification. It is used as a simple system to record the order of the tests and organization of the data files. It should be noted that Tubes 3-6 used the ceramic end plug to distribute load, while 7-10 were potted in epoxy.

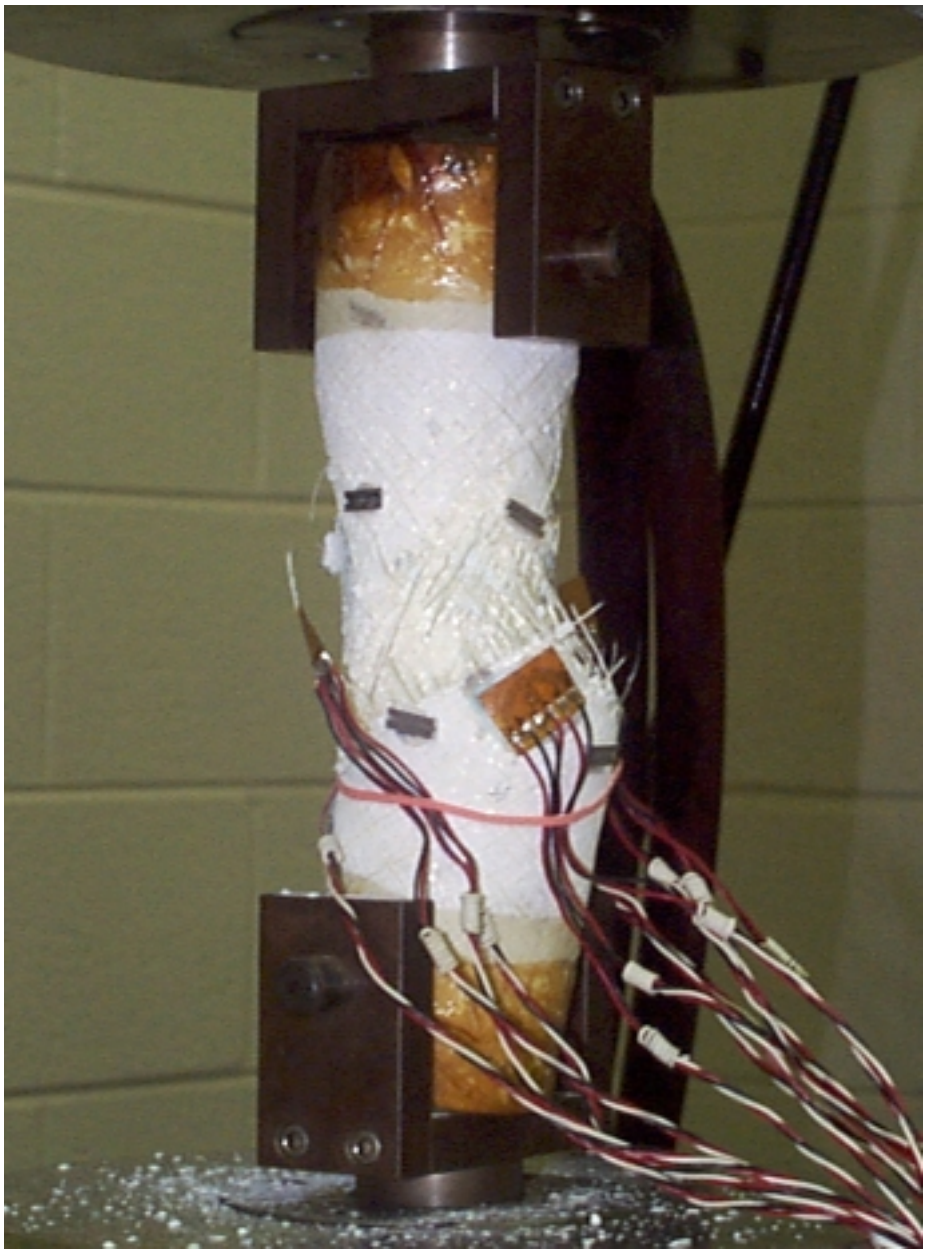

Figure 2.15: Tube tensile failure mode: *necking and stretching*

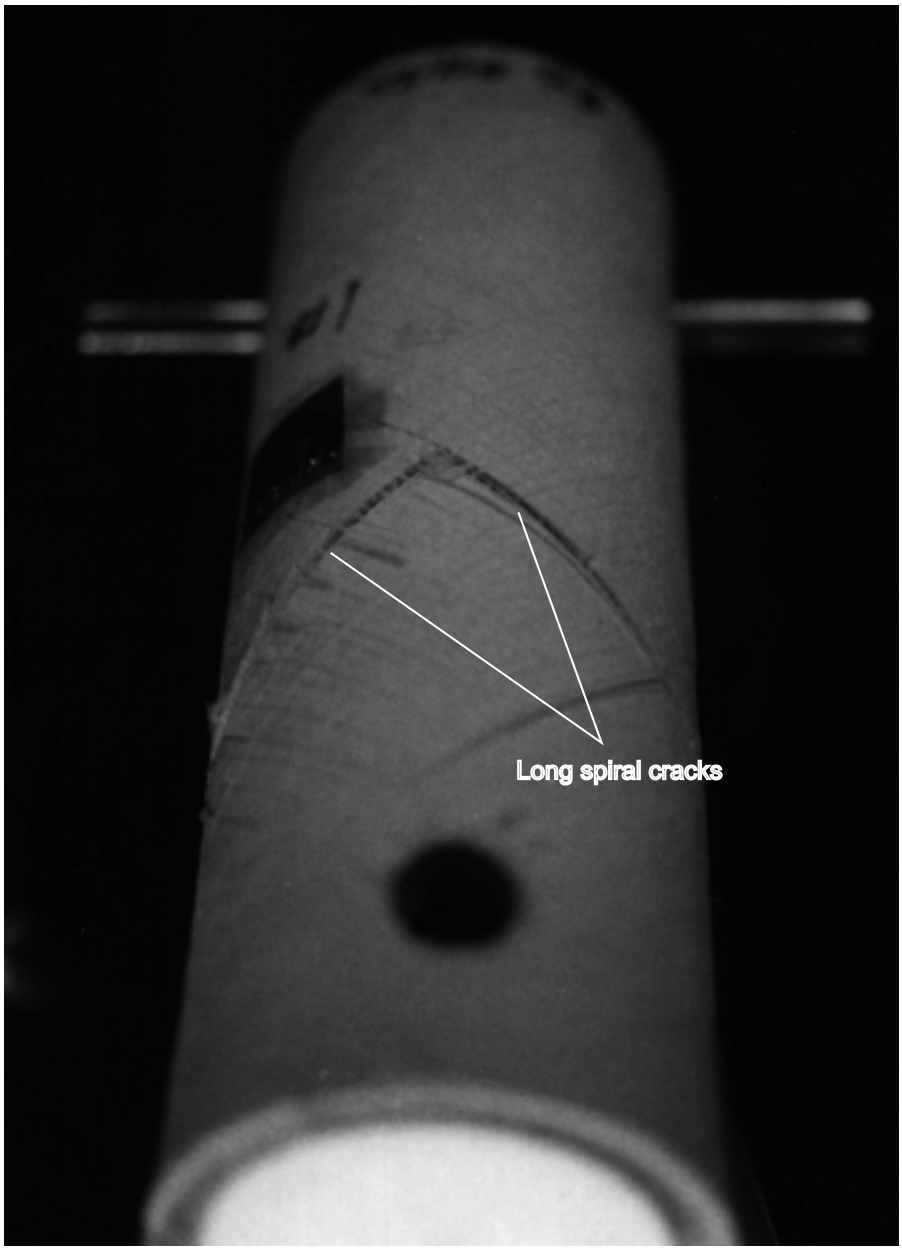

Figure 2.16: Tube tensile failure mode: *localized cracking*

Table 2.3: Measured tensile and torsional stiffness of 7-in tube specimens.

ID	Tube #	cycles	SG Tension (GPa)	Ext Tension (GPa)	Torsion (GPa)
7-2-28-3	3	0	3.948	3.300	7.581
7-2-28-4	4	0	4.100	3.379	7.855
7-5-13-C	7	10^3	4.216	3.441	6.985
7-5-13-E	6	10^3	4.011	3.324	
7-5-13-NH	8	10^3	3.747	3.504	7.853
7-6-12-A	10	10^4	4.519	4.323	7.516
7-6-12-C		10^4	4.481	3.498	8.661
7-6-12-E	5	10^4		3.458	7.961
7-6-12-NH		10^4	4.396	3.244	8.567
7-6-16-A		10^5	4.550	3.260	8.986
7-6-16-C	11	10^5	4.454	3.848	9.428

Figure 2.17 and 2.18 have the stiffness and strength plotted as a function of the the back-pulse cycles. The result shows that the stiffness is not adversely affected by the simulated back-pulsing cycles, while the strength has shown noticeable degradation.

2.2.3 Bend Test Result

A typical load deflection curve is shown in Figure 2.19. Following an initial linear range, the curve turned and has a smaller slope when the load reaches about 50 lbf. As the load increase, the instantaneous load-strain slope kept decreasing unstill almost horizontal. The failure process is captured by the pictures shown in Figure 2.20 to 2.22. Local delamination and bucking formed in the region near the top loading point. Continued loading produced shear failure which happened right along the continuous fiber tow direction on the tube outer surface.

The cantilever bend result is shown in Figure 2.23. In one of the test runs, the load reading did not come back to zero after the end of the test. It may be caused by the the excessive drifting of the strain gage amplifier as part of a home-made load cell. The result shows that the strongest of the three sample is the phosphate bonded tube. And the field-tested tube is stronger than the as-fabricated one among the two tubes with alumina bonding system. All tubes did not fail at the point with the maximum bending moment; instead, they failed at about one and half inches away for the root of the cantilever. The failure modes were similar to those in three point bend tests. Fiber tows buckled on the compression side and shear occurred on both sides along a roughly 45° line to the tube axis. The failure behavior remains non-catastrophics even at very large applied displacement. Figure 2.24 shows a cantilever bend sample at a total displacement of one inch.

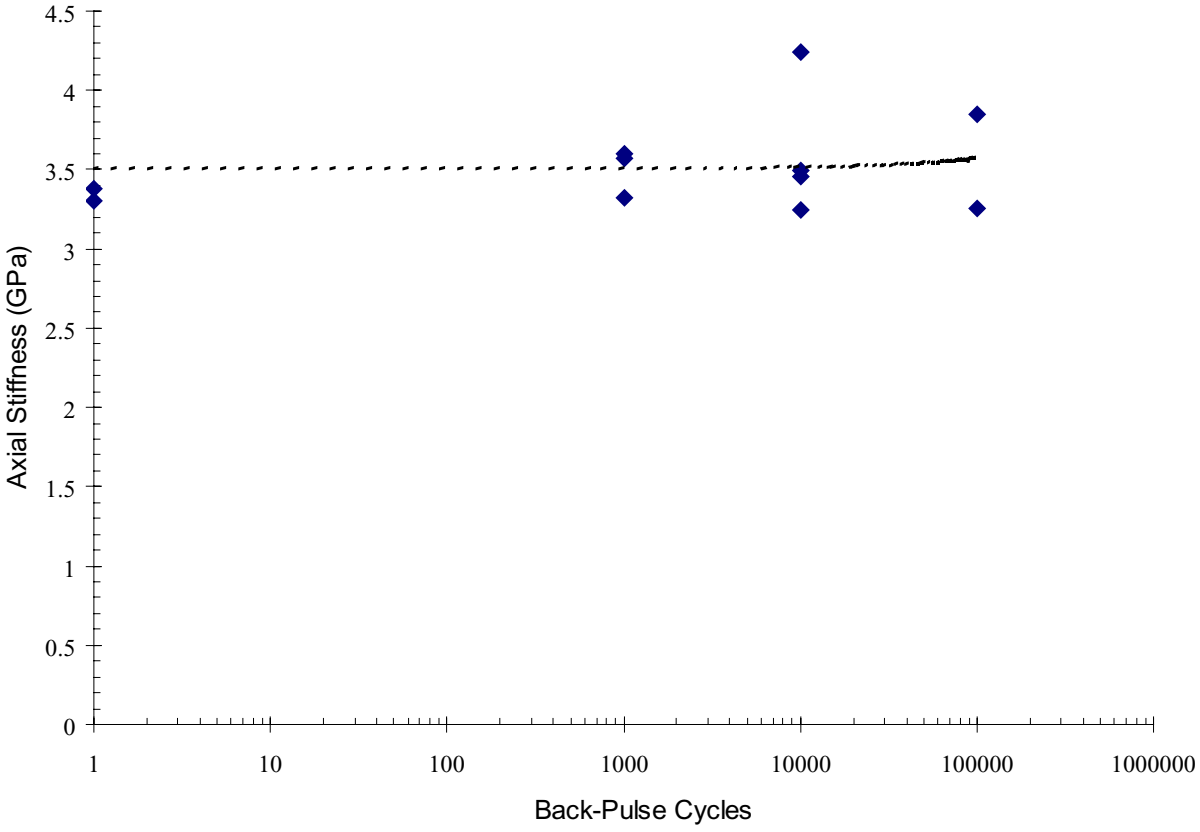

Figure 2.17: Effect of simulated back-pulsing on tube axial stiffness.

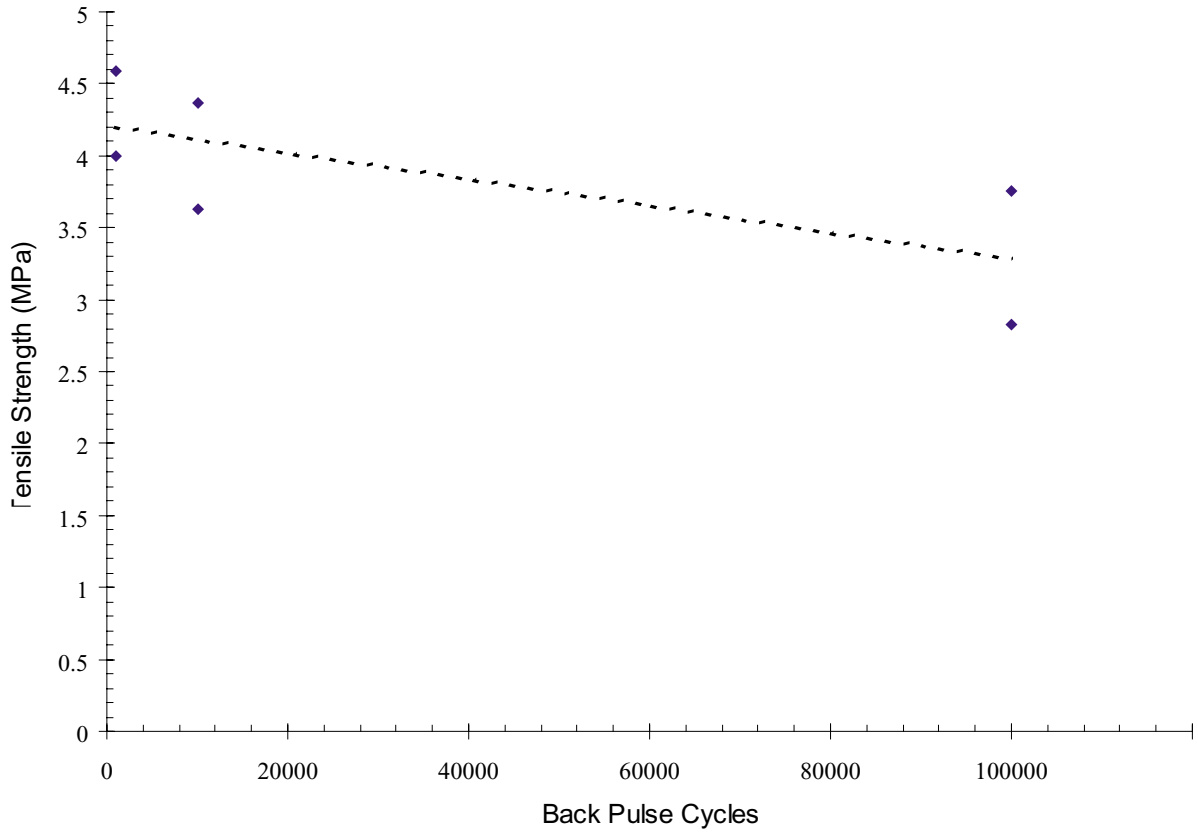

Figure 2.18: Effect of simulated back-pulsing on tube tensile strength.

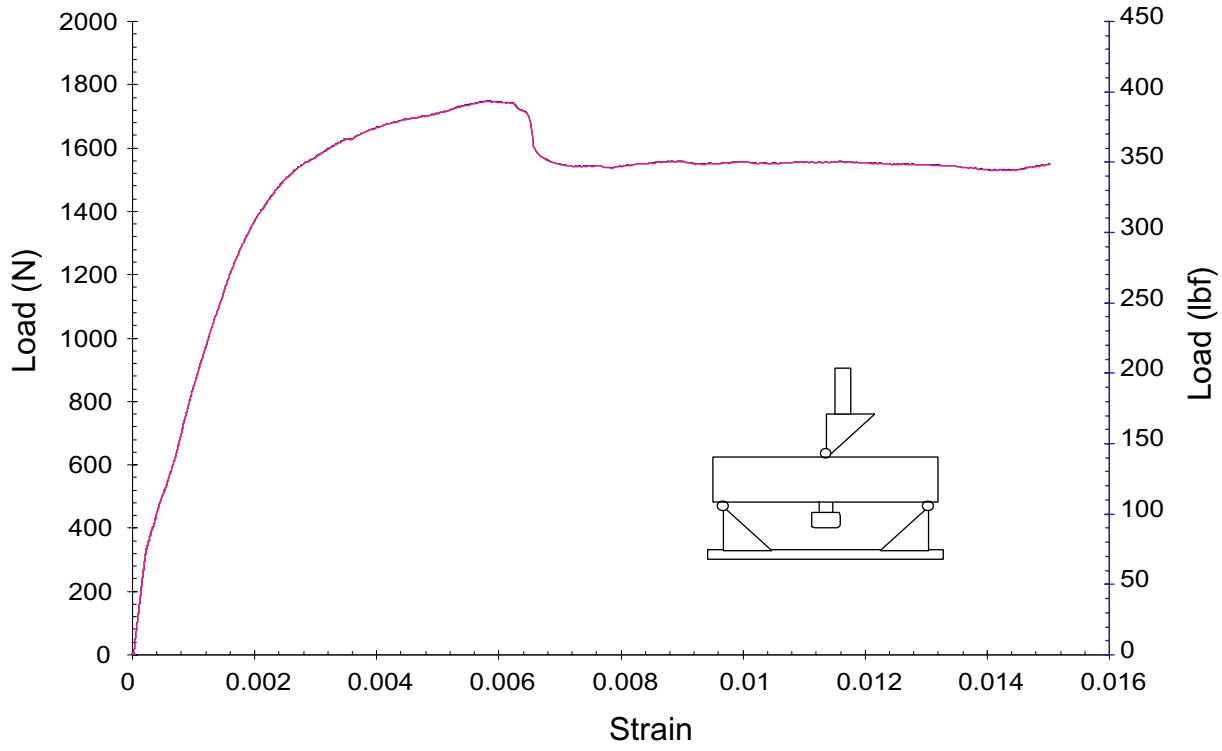

Figure 2.19: Three-point bend result: load v.s. strain.

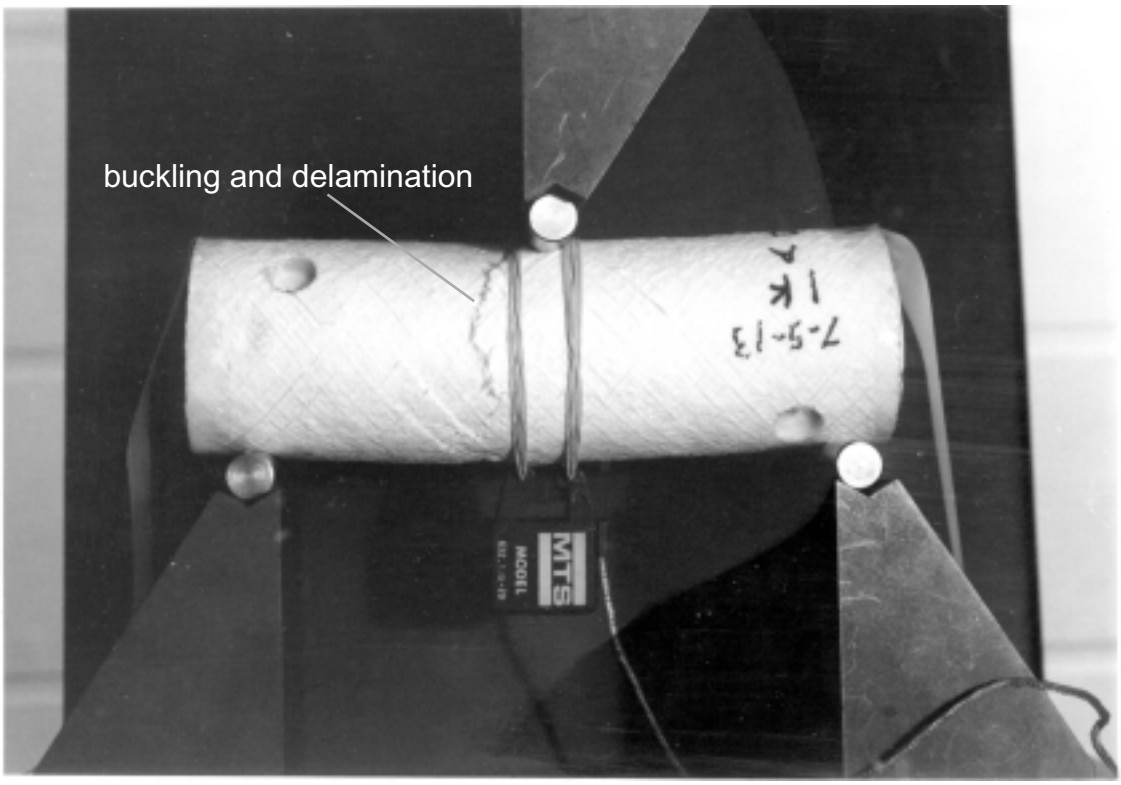

Figure 2.20: Three-point bend failure sequence: No. 1

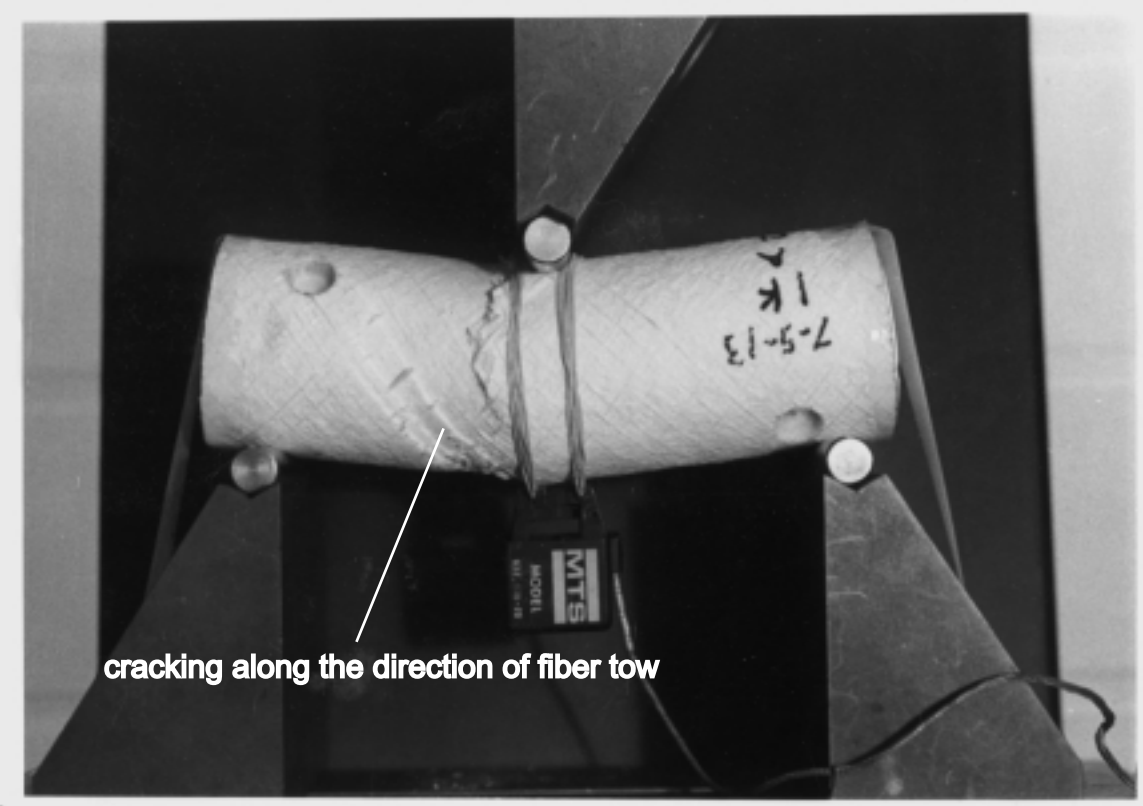

Figure 2.21: Three-point bend failure sequence: No. 2

Figure 2.22: Three-point bend failure sequence: No. 2 (side view)

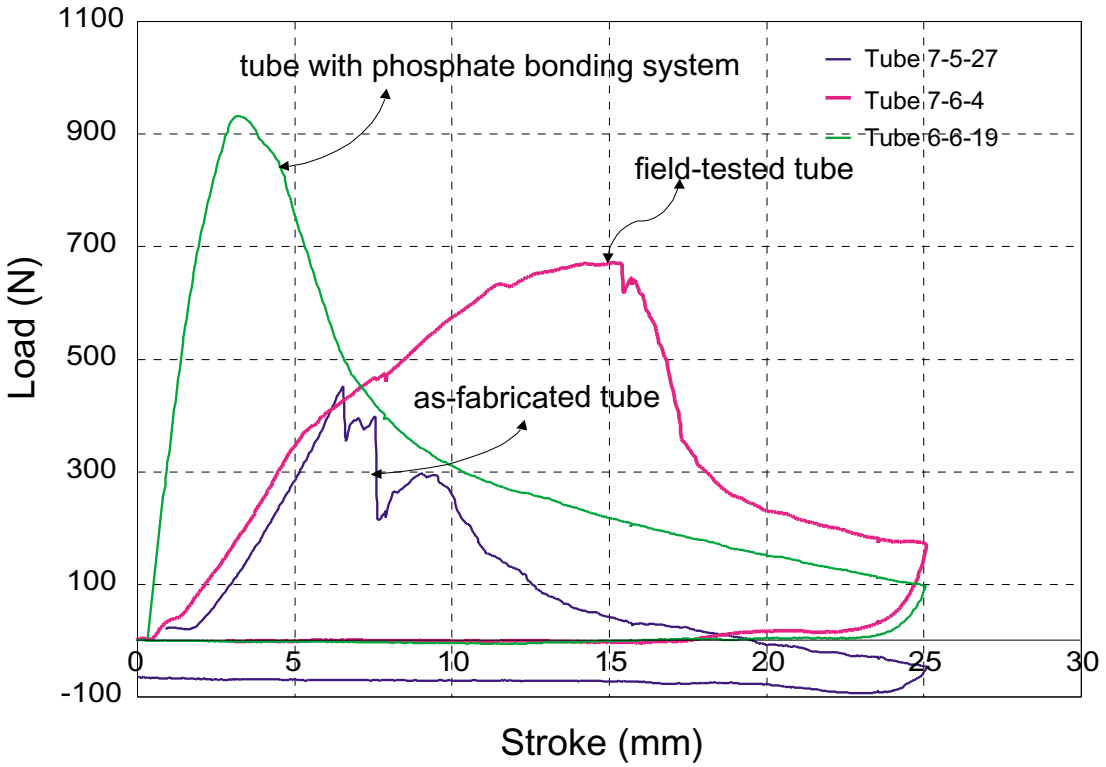

Figure 2.23: Cantilever bend test result.

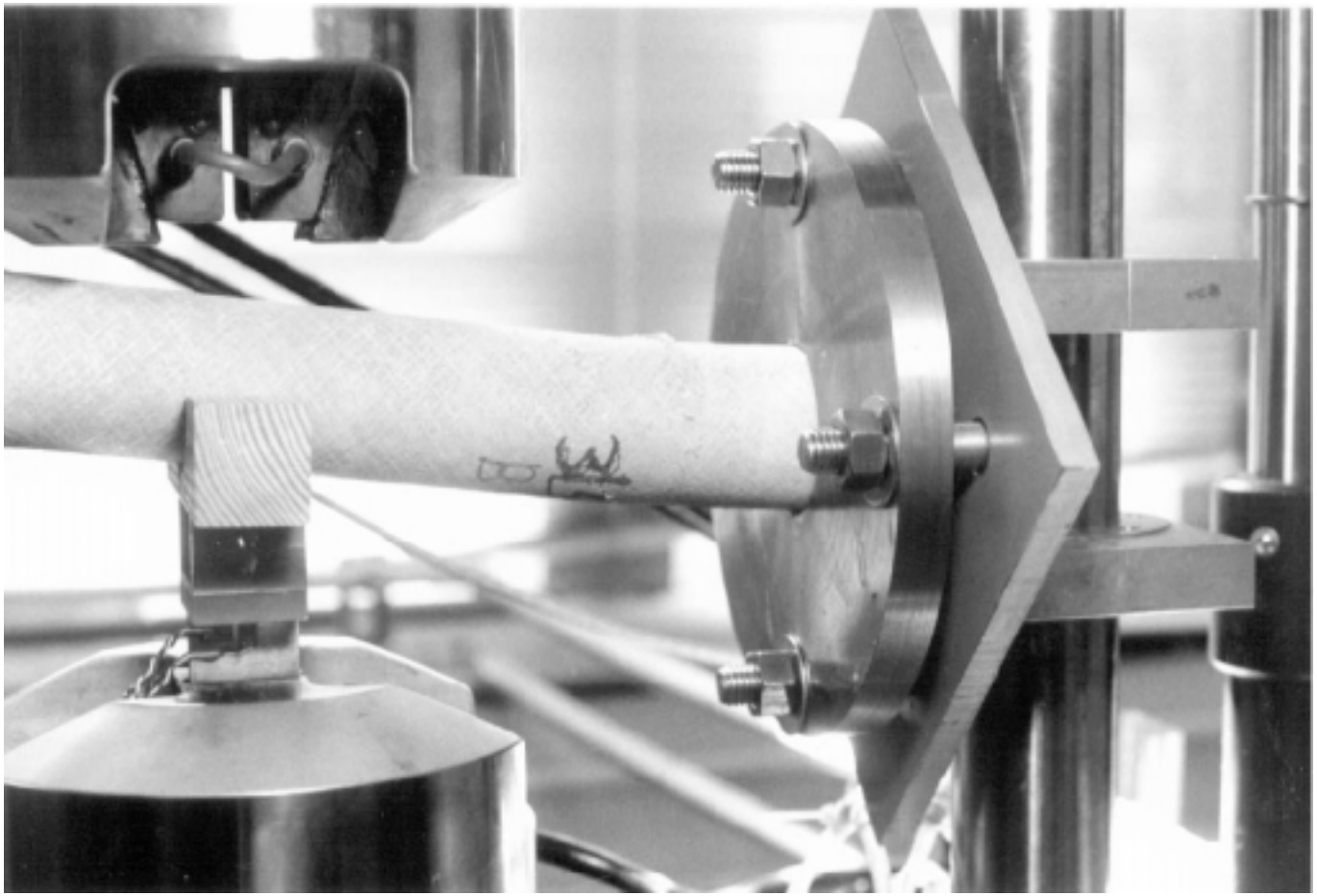

Figure 2.24: Photograph of a cantilever bend sample at 1-inch displacement.

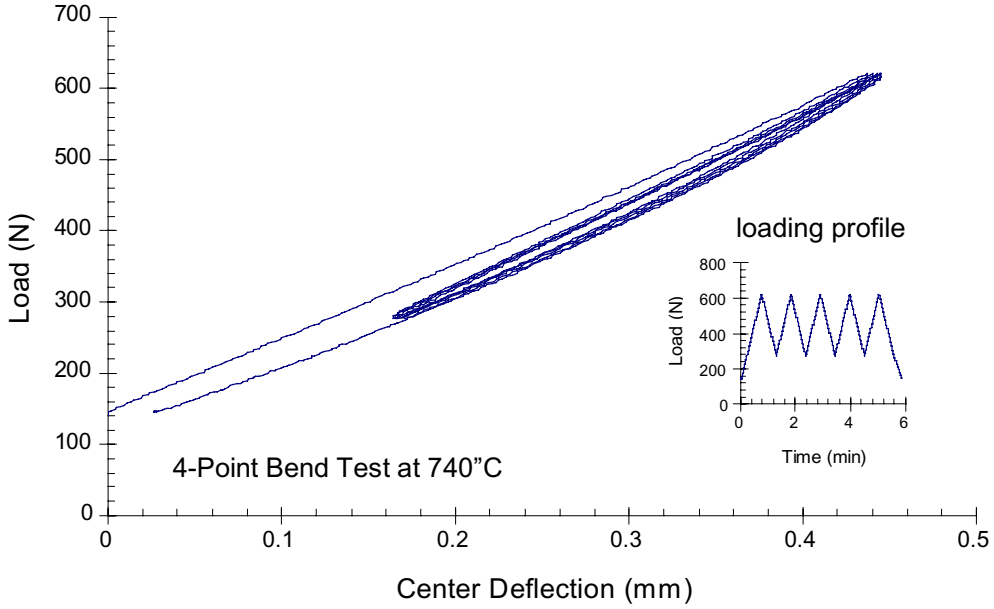

Figure 2.25: Four-point bend test result at 740 °C.

A typical 4-point bend curve is shown in Figure 2.25. The curve is slightly non-linear. It also has a hysterisis loop and a residual deflection. The exact source for those behavior is not clear and could be the caused by the test fixture or by some measurement instruments.

One specimen was tested at a series of temperatures. At each temperature, the upper portions of the unloading curves were fitted to a straight lines and their slopes were calculated and shown in Figure 2.26. The curve indicates a slight decrease of flexure stiffness with increasing temperature.

A 4-point bend to failure test was performed at room temperature, and the tube failed at one of the loading points instead of at the center, as shown in Figure 2.27. The failure was non-catastrophic. Due to the complex stress state at the failure point, we were unable to obtain reliable material strength data. To induce a failure at the center of the tube in the 4-point bend test, we would have to use a much longer tube. No further high temperature 4-point bend to failure tests were performed.

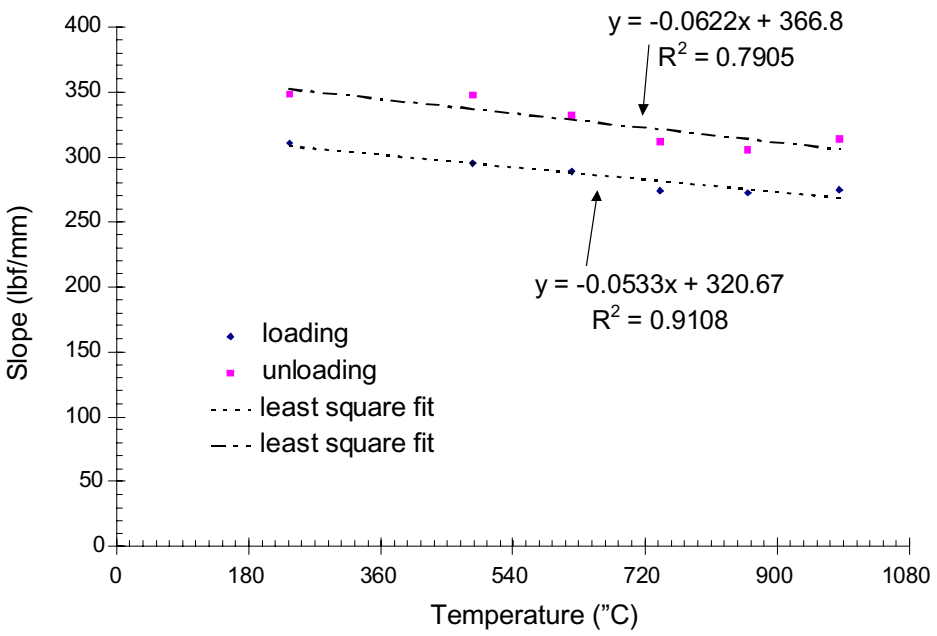

Figure 2.26: Dependence of unloading slope on temperature.

2.3 Microstructure Characterization

To reveal the microstructure of the MTI candle filter material, scanning electron microscopy was performed on sections of the test samples. Porous ceramic composites have delicate microstructure, and the constituent materials are brittle. Unprotected cutting with a diamond saw would inevitably destroy the original microstructure of the cut surface. A special procedure was adopted in the sample preparation. Before the specimen was cut, the sample was impregnated with an acetone-soluble thermoplastic resin. After the resin is cured, the specimen is cut and the cut surface is polished. Then the specimens is soaked into acetone to dissolve the resin. To remove the residues of the resin, the specimen is baked at 400 °C in a furnace for one hour. Then the specimen is sputtered on with a thin gold layer and examined under scanning electron microscope. Some microscopic features of the interest are: the distribution of chopped fibers, the distribution of bonding agents, the shape and area of

Figure 2.27: Failed four-point bend test specimen.

Table 2.4: Tow cross-section shape measurement results.

	$2a$ micron	$2b$ micron
average	510.2	237.8
std.	48.9	20.1

the fiber tow cross section, the cross-over point of fiber tow, the waviness of fiber tow, etc. Cuts were made both perpendicular and at 45°to the tube axis to allow the visual access of all above features. Selected SEM images are shown in Figures 2.28 to 2.34.

It was suspected that the bonding agent may cluster near the cross-over point of fiber tow, but the SEM observations on many such cross-over points showed the contrary result. Figure 2.28 is a typical tow cross-over point, where there is little bonding agent between the tows. Figure 2.31 is a higher magnification observation at a longitudinal fiber tow near a transverse tow. The distribution of bonding agent appears higher within the tows and among the Saffil fibers rather than forming thick bonds at cross-overs. The filaments in the fiber tows are almost fully bonded with very few voids. The cross-section shape of the fiber tow is the typical lenticular shape as seen in many textile composites. The length of the long axis and the short axis of the lenticular cross-sections were measured and the result is summarized in Table 2.4.

Figure 2.29 is a picture taken at about 45° to the tube axis and the shape of the fiber tow along its axis is shown. It was observed that there is large spacing between the tow cross-overs and the fiber tow is fairly straight between the two cross-overs. At a cross-over point, fiber tow bends a little towards the perpendicular tow it touches. Figure 2.31 to 2.33 are magnified view of chopped fiber matrix. The chopped-fiber matrix around a fiber tow is shown in Figure 2.31. Large open space can be seen clearly inside the chopped-fiber matrix while the fiber tow is relatively solid. It was observed that the chopped fibers take preferred

orientations that are parallel to the surface of the filter tube as a result of the filament winding process. In Figure 2.32, the orientation distribution of chopped fibers near a fiber tow is shown, the orientation of chopped fibers are significantly affected by the fiber tow and taking a orientation parallel to the surface of the nearby fiber tow. The distribution of bonding agent inside the chopped fiber matrix in shown in Figure 2.33. It was observed that the bonding agent is distributed fairly uniformly with few large clusters form at the the point where many fibers cross over. To get a panorama view of the microstructure, multiple pictures were assembled to get a through-the-thickness image, as shown in Figure 2.34. The assemble had to be done because the field size of the SEM is limited at large magnifications. It was observed that the bonding agent has a non-uniform distribution through the thickness. The content of bonding agent increases towards the outer surface. Regions near the inner surface have little or no bonding agent, while regions near the outer surface have a high concentration of bonding agent.

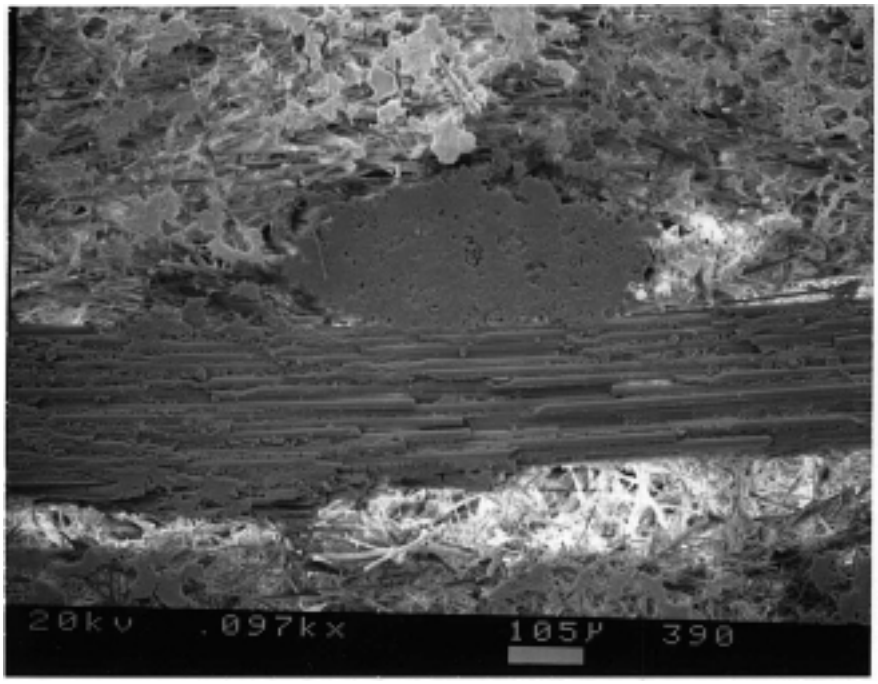

Figure 2.28: SEM picture of tube cross-section: *a tow cross-over point*

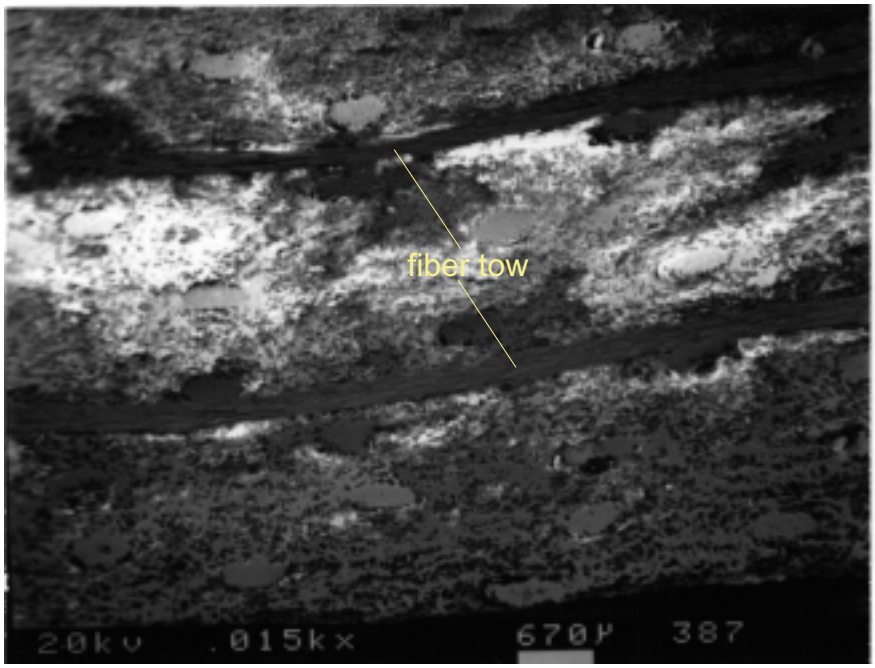

Figure 2.29: SEM picture of tube cross-section: *wavy tows*

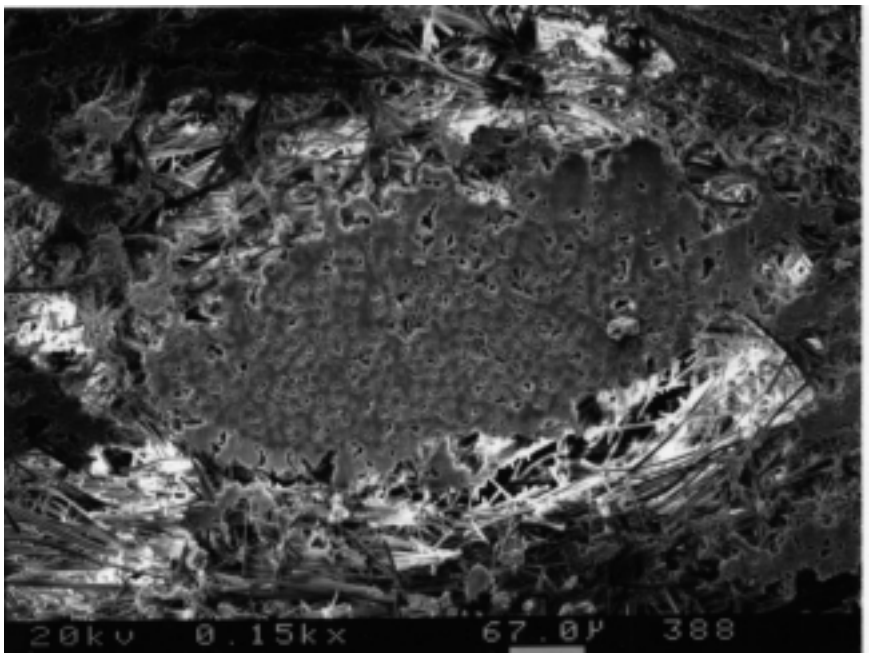

Figure 2.30: SEM picture of tube cross-section: *a tow cross-section*

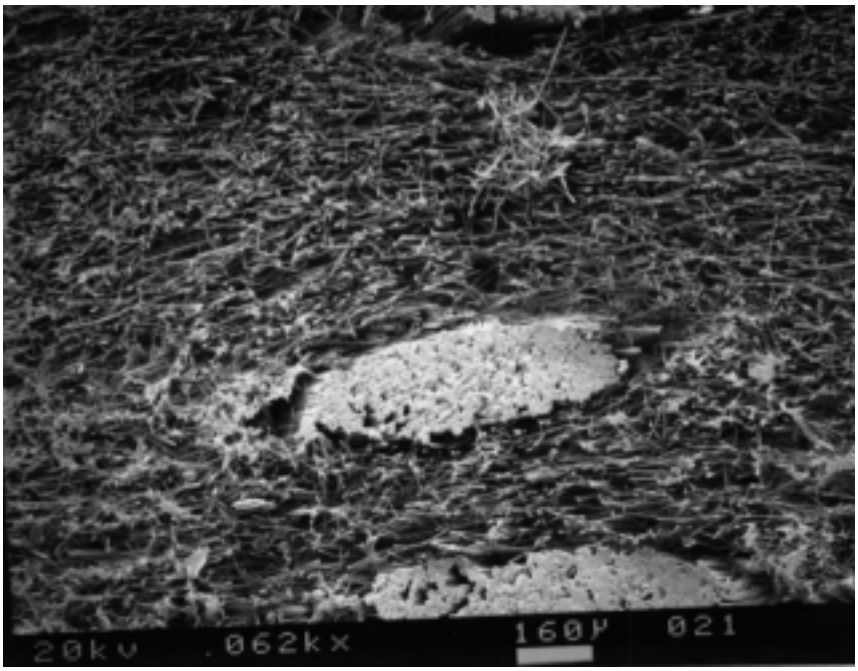

Figure 2.31: SEM picture of tube cross-section: *chopped fiber distribution around tow*

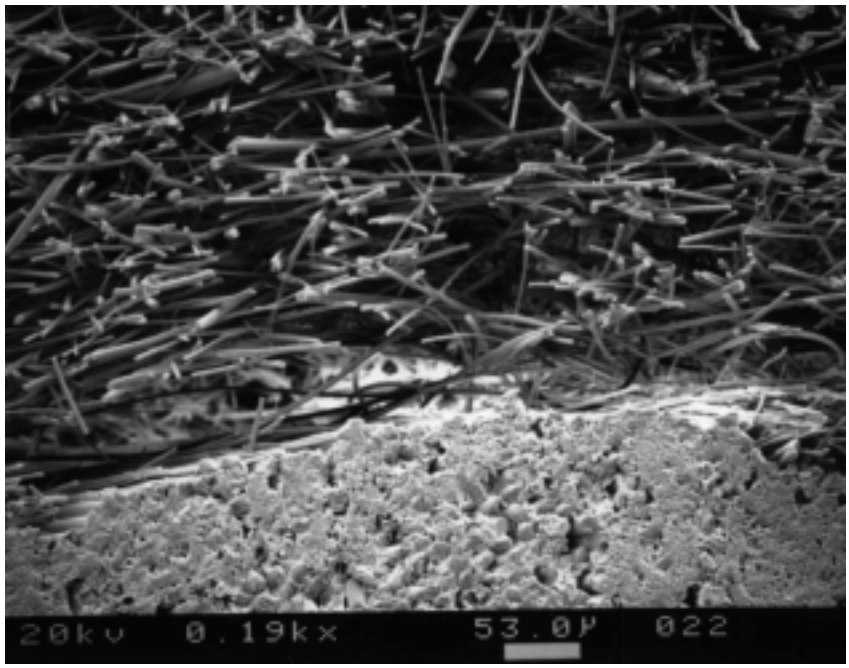

Figure 2.32: SEM picture of tube cross-section: *tow-matrix interface*

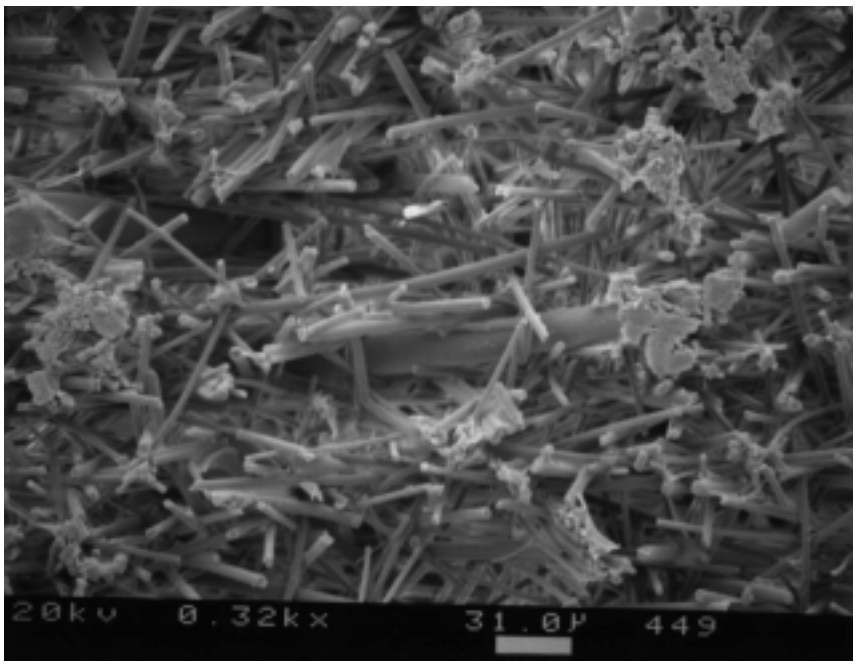

Figure 2.33: SEM picture of tube cross-section: *orientation of chopped fibers*

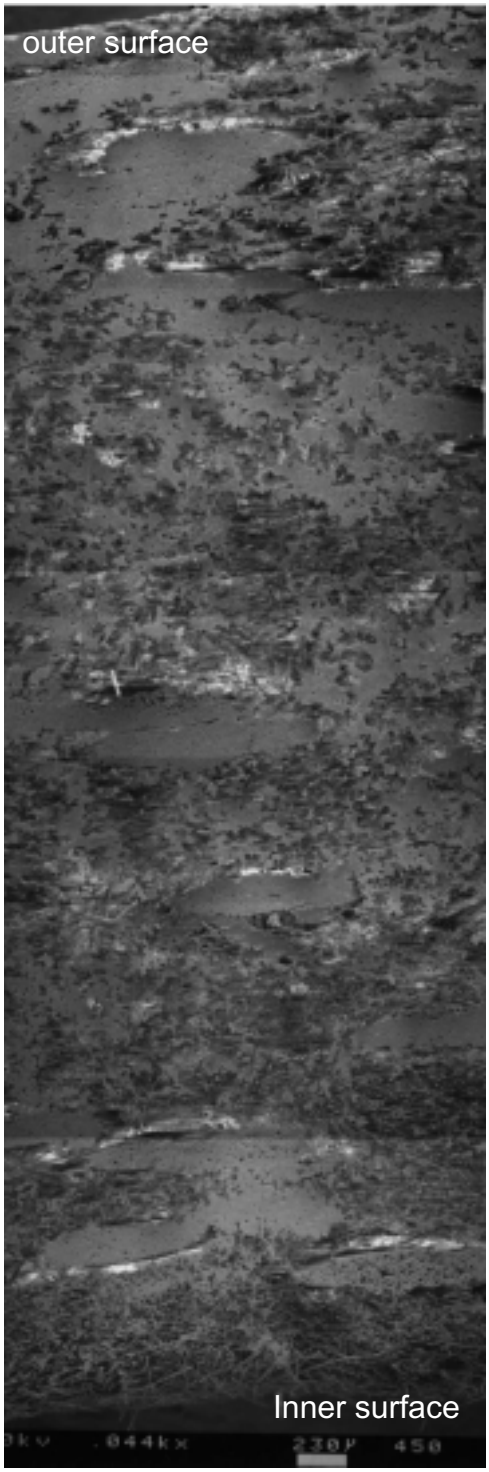

Figure 2.34: SEM picture of tube cross-section: *panaroma view across tube wall*

Chapter 3

Micromechanics of Porous Materials with Stochastic Microstructures

Micromechanics concerns the stress and strain response of a heterogeneous material at the microstructural level. One objective of micromechanics modeling is to determine the effective (overall) properties of a heterogeneous material as a function of its microstrucrual details. This is also one of the fundamental problems in both mechanics and composite material field. To express overall properties of a composite material as a function of the properties of its constituents, simple empirical models (e.g. rule of mixture) have been widely used. Hashin and Shtrikman [23, 25, 24] derived explicit variational bounds for a homogeneous material with dilute spherical and cylindrical inclusions. The only geometric information required in these simple closed-form predictive equations is the volume fraction for each constituents. These predictions are only acceptable in a number of special cases. In more general cases, the effective properties are found to depend not only on the volume fractions of the constituent materials but also on their morphological details. Additional microstructural information needs to be incorporated into the micromechanics model in order to make a better prediction.

The two primary approaches to incorporate "higher-order" morphological information in predicting the effective properties of a heterogeneous material are: (i) the statistical approach [63, 64] and (ii) the micromechanics approach [42].

In the statistical approach, the"higher-order" microstructural information is described in the so-called multi-point correlation functions, which represent the probability of finding n arbitrary material points having the same material properties. With the help of variational principles, such as that of Hashin and Shtrikman, the upper and lower bounds of the overall properties can be expressed as integrals of the constituent material properties weighted by these n-point correlation functions. There are two major problems with this approach: firstly, for a lot of material systems, the bounds so-obtained are too widely apart to render any practically useful information; and secondly, the n-point correlation functions have been practically unobtainable through measurements.

The micromechanics approach relies on the concept of a representative volume element (RVE), which is a small volume of material but is statistically representative of the entire population of heterogeneities. Usually, boundary value problems (BVP) are formulated on the RVE and the effective properties emerge in the solution process of the BVP. The micromechanics approaches can be further classified into two varieties: the average-field theory [42] and the homogenization theory [27, 52]. The average field theory is based on the fact that the effective properties are relations between the volume average of the stress and stain at the microscopic level. The effective properties are determined as relations between the average micro-fields. In the homogenization theory, the relations between micro-field and macro-field are established by a multi-scale perturbation method. It best applies to the heterogeneous materials which possess periodic microstructures. In this case, only the smallest repetitive volume element—"a unit cell"—needs to be analyzed; models can be greatly simplified, sometimes, closed-form predictive equations can be obtained. For a completely stochastic material there is little hope to find closed-form solutions, so research efforts have

shifted to numerical simulations. With the rapid growth of computer performance, many seemingly computational intensive problems several years ago are now routinely solved with current state-of-the-art personal computers.

Porosity adds another level of complexity in the micromechanics modeling of heterogeneous material because of the large and tortuous internal surfaces and the lack of periodicity and symmetry in the microstruture. One objective of this research is to establish a general computational micromechanics foundation for the evaluation of the effective elastic properties of a highly porous material with stochastic microstructures. The methodology is presented in the first part (section 3.1) of the chapter; in the second part (section 3.2), it is applied to a special class of porous heterogeneous material with a microstructure that resembles a random fibrous network.

3.1 A Computational Micromechanics Approach

In micromechanics, traditional continuum mechanics theory is applied to microscopic heterogeneities. It is assumed that stress and strain as defined in continuum theory are still applicable at this length scale. This is justified by comparing the size of heterogeneities ($10^{-6}\ m$) to that of an atomic lattice ($10^{-10}\ m$). Even though the microscopic stress and strain do "exist", they are generally not very useful in engineering practice because they can neither be observed nor be measured conveniently. The linkage between microscopic quantities and macroscopic quantities are established in the average field formalism [42, 12], in which the macroscopic quantities are defined as the volume average of microscopic quantities. It can be shown that the volume averages of microscopic stress and strain as defined in Equation 3.1 and 3.2 are equivalent to the macroscopic stress and strain used in engineering practice under certain conditions including linear elastic and small deformation [42]. In this formalism, the macro-level elastic tensor, C_{ijkl}, is equivalent to the tensor that links the av-

erage strain to the average stress. Equation 3.1 to 3.3 show the basic definitions used in the average field formalism. The notation $\langle f \rangle$ indicates a volume average of the field variable, $f = f(x, y, z)$, inside the bracket.

$$\langle \sigma_{ij} \rangle = \int_V \sigma_{ij} dV \tag{3.1}$$

$$\langle \epsilon_{ij} \rangle = \int_V \epsilon_{ij} dV \tag{3.2}$$

$$\langle \sigma_{ij} \rangle = C_{ijkl} \langle \epsilon_{kl} \rangle \tag{3.3}$$

The purpose here is to find the macro-level material properties as functions of the composite microstruture. According to the average field formalism, to find the macro-level elastic properties is equivalent to finding the relationship between the average micro-stress and the average micro-strain. Before the calculation of micro-stress and micro-strain, an RVE has to be identified and proper boundary conditions on the RVE have to be assumed. The detail of the procedures is discussed in the next two sections.

3.1.1 Representative Volume Element

The central conceptual tool in micromechanics is that of an RVE, i.e., a small material element. To qualify an RVE, the volume of the material element identified must be small enough compared to the size of a structure component so that it can be viewed as a "material point" in the sense of traditional continuum theory working at the macro-scale; on the other hand, in order to be "representative", an RVE needs to be big enough so that it includes a large number of micro-level heterogeneities. Because of the mutually exclusive qualifications, the identification of the RVE is a relatively subjective matter and depends on the specific

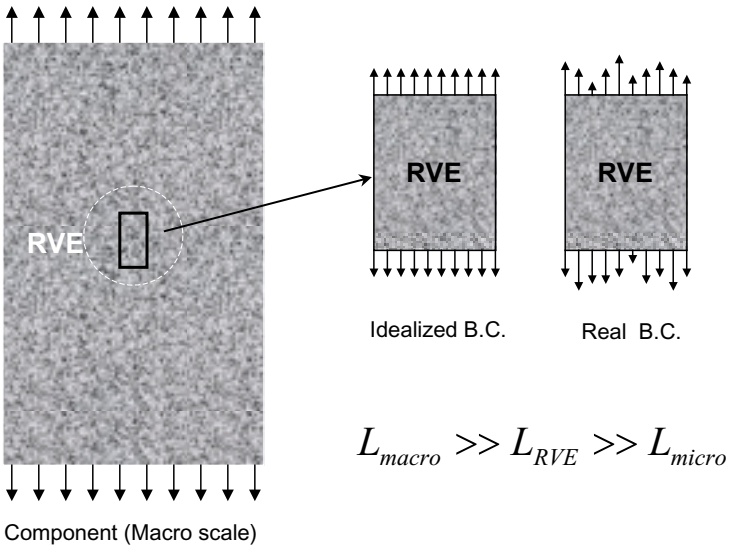

Figure 3.1: Concept of a representative volume element.

characteristics of the material system under examination. A rule-of-thumb for the size of the RVE is: 0.1 to 1 *mm* for metal and polymer, 1 *cm* for wood, and 10 *cm* for concrete [38].

In the domain defined by an RVE, micro-level heterogeneities are modeled explicitly and are considered continuum domains with different material properties. Usually, a BVP is formulated on the domain defined by the RVE. Certain boundary conditions are applied to the surface of the RVE and then the BVP is solved either analytically or numerically. The effective properties are typically derived from the solution process of the BVP.

The boundary conditions on the selected RVE are absolutely critical to the accuracy of the predictions of the effective properties, but the "real" boundary conditions on the RVE are essentially unknown. A number of simplifying boundary conditions have been used. These include: uniform displacement, uniform traction, affine deformation through out the volume, and periodic displacement. Figure 3.1 illustrates the "idealized" boundary conditions and the actual boundary conditions on an RVE. Among these assumptions, uniform and affine displacement conditions usually over-constraint the RVE and result in an over-prediction of

the moduli. Uniform traction usually causes an under-prediction of the effective moduli. The periodic boundary conditions result in moduli in between the two extreme, but it requires the RVE to possess certain geometric periodicity, which is not present in materials with stochastic microstructures.

To deal with this dilemma, the author has contrived a concept—"an observation window". It is schematically shown in Figure 3.2. The observation window is a fraction of the RVE; the average stress and strain are evaluated only inside the observation window instead of the whole RVE, a uniform boundary conditions are applied on the boundary of RVE. The argument is that when the boundary of the observation window is sufficiently away from the boundary of the RVE, artificial over-/under-constraints, which are caused by enforcing uniform boundary conditions, would be "damped" out. The use of an observation window would allow a better prediction for materials without any periodic or symmetric microstructures. The trade-off is that the RVE needs to be bigger than usual.

The solution of the BVP defined on an RVE usually calls for numerical methods, predominantly the finite element procedure. There are no essential difficulties in terms of finite element modeling *per se*. With current state-of-the-art finite element algorithms, BVPs defined on irregular domains with various nonlinearities are routinely solved by a number of commercial software packages. But the problem of numerical efficiency is still relevant. By judicious decisions on the level of details to model, the type of elements, the solution procedures, etc., the size of the numerical BVP and the cost of numerical solution can be significantly reduced while the essential behavior of the RVE can still be captured.

3.1.2 Calculation of Average Strain

Upon the solution of a BVP defined on the RVE, the deformation, micro-stress, and micro-strain inside the RVE are obtained. To estimate the effective elastic properties, the average

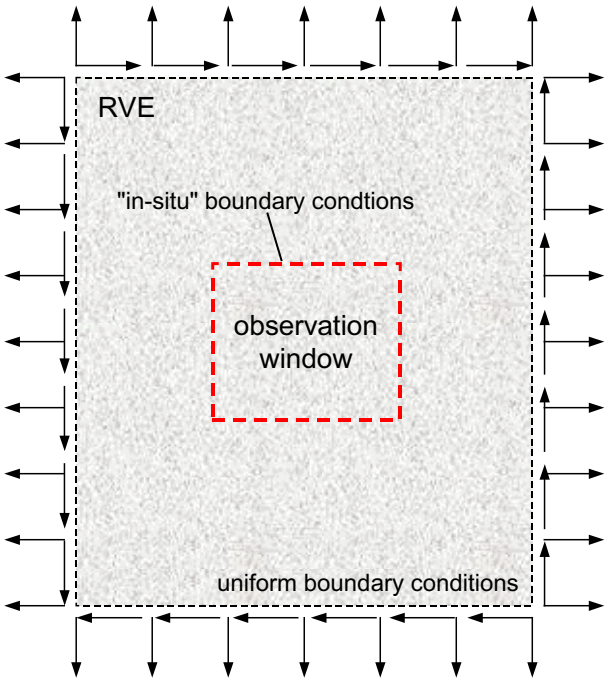

Figure 3.2: Concept of an observation window.

strain needs to be calculated. In the formalism of the average field theory, the average strain is defined as the volume average of micro-strains inside the RVE. The calculation of this average strain could be a very cumbersome task if the definition (Equation 3.2) is used directly. Alternatively, the average strain is related to the surface displacement by Equation 3.4. In which, S_2 is the external surface of a dense RVE. For a porous RVE, S_2 also includes the internal surfaces. Equation 3.4 is proved to be valid for heterogeneous dense materials as long as the displacement is continuous in the solid domain [60]. For a porous material with very large and irregular internal surfaces, this approach can become very tedious too. To use either of the above methods, the morphological details of the load bearing skeleton of the porous RVE have to be modeled in order to get an accurate result.

$$\langle \epsilon_{ij} \rangle = \frac{1}{V} \int_V \epsilon_{ij}\,(x, y, z)\, dV = \frac{1}{V} \int_{S_2} (u_i n_j + u_j n_i)\, dS \tag{3.4}$$

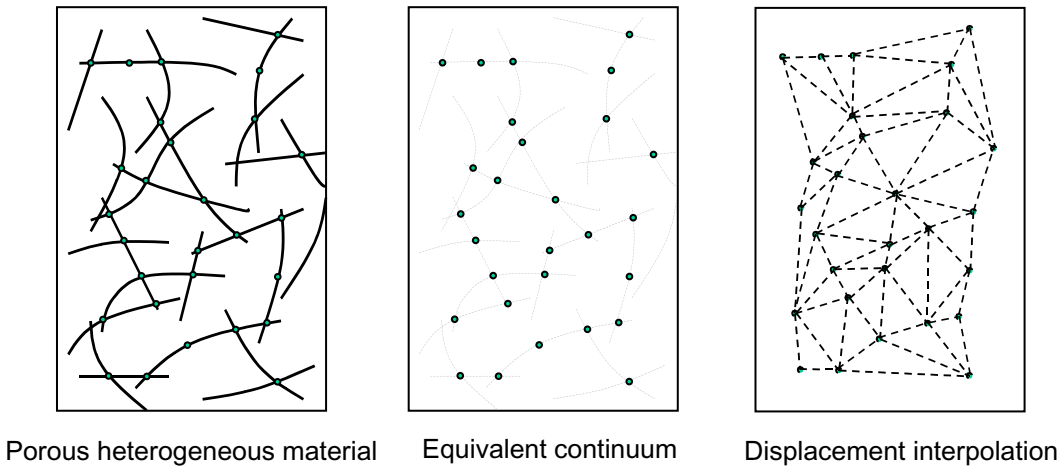

Figure 3.3: Calculation of average strain for a porous heterogeneous material.

To circumvent this difficulty in calculating the average strain, the author has developed an intuitive approach based on the analogy shown in Figure 3.3. As a comparison material, an equivalent homogeneous medium—equivalent continuum—is assumed to have the effective properties of the porous heterogeneous material. For every point on the load bearing skeleton of the porous RVE, there corresponds a point in the equivalent continuum. Suppose the displacement values of a set of points on the porous skeleton are assigned to the corresponding points in the equivalent continuum, we argue that the average strain of the porous RVE is approximated by the average strain of the equivalent continuum. This can be understood as if the porous RVE is bonded to an overlapping continuum through those points. In this way, the problem of finding the average strain in a porous heterogeneous RVE is converted to finding the average strain of a dense continuum given the displacement of a number of key points that are randomly distributed inside the continuum.

Given the displacements of a set of key points, the displacement field inside the volume can be approximated by triangular (in 3D case, tetrahedron) tessellation and displacement interpolation. By triangular tessellation, the domain is divided into triangles/tetrahedrons with the given points as vertexes. Inside each triangle or tetrahedron, the displacement

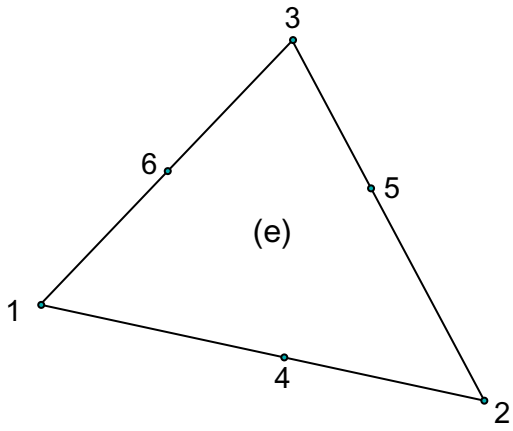

Figure 3.4: Numbering convention used in the interpolation scheme.

field can be interpolated using the displacement values on the vertexes. The displacement gradients, i.e., the strain, can then be calculated in each triangle and summed over the volume. This is essentially the interpolation scheme used in the standard displacement-based finite element formulation.

2D formulation:

A detailed 2D formulation of the above described procedure is shown below. The triangular tessellation can be performed by the Delaunay triangulation algorithm. The vertexes and three mid-points on the edges of a triangle will be numbered in the way shown in Figure 3.4.

The displacement field inside a triangle is assumed to have the following forms:

$$\begin{cases} u(x,y) = N_i(x,y)\, u_i \\ v(x,y) = N_i(x,y)\, v_i \end{cases} \tag{3.5}$$

in which, $i = 1, \cdots, 6$; u_i and v_i are the displacement of point i in x and y direction.

The form of $N_i(x,y)$ is assumed to be a complete second order polynomial in terms of x and

y with six undetermined coefficients (a_{i1} to a_{i6}).

$$N_i(x,y) = a_{i1} + a_{i2}x + a_{i3}y + a_{i4}x^2 + a_{i5}xy + a_{i6}y^2 \tag{3.6}$$

To ensure continuity of the displacement field along the common boundary of two neighboring triangle, it is required that:

$$N_i(x_j, y_j) = \delta_{ij} \tag{3.7}$$

This is equivalent to:

$$\begin{bmatrix} 1 & x_1 & y_1 & x_1^2 & x_1y_1 & y_1^2 \\ 1 & x_2 & y_2 & x_2^2 & x_2y_2 & y_2^2 \\ 1 & x_3 & y_3 & x_3^2 & x_3y_3 & y_3^2 \\ 1 & x_4 & y_4 & x_4^2 & x_4y_4 & y_4^2 \\ 1 & x_5 & y_5 & x_5^2 & x_5y_5 & y_5^2 \\ 1 & x_6 & y_6 & x_6^2 & x_6y_6 & y_6^2 \end{bmatrix} \cdot \begin{Bmatrix} a_{j1} \\ a_{j2} \\ a_{j3} \\ a_{j4} \\ a_{j5} \\ a_{j6} \end{Bmatrix} = \begin{Bmatrix} 0 \\ \vdots \\ 1_j \\ \vdots \\ 0 \\ 0 \end{Bmatrix} \tag{3.8}$$

The unknown coefficients of the interpolation function $N_i(x,y)$ can be obtained by solving Equation 3.8.

In the continuum theory, the infinitesimal strain is defined as the combinations of displacement gradients as shown below:

$$\epsilon_x = \frac{\partial u}{\partial x} = u_i \frac{\partial N_i(x,y)}{\partial x} \tag{3.9}$$

$$\epsilon_y = \frac{\partial v}{\partial y} = v_i \frac{\partial N_i(x,y)}{\partial y} \tag{3.10}$$

$$\gamma_{x,y} = \frac{\partial u}{\partial y} + \frac{\partial v}{\partial x} = u_i \frac{\partial N_i(x,y)}{\partial y} + v_i \frac{\partial N_i(x,y)}{\partial x} \tag{3.11}$$

in the vector form, Equation 3.9 to 3.11 can be expressed as:

$$\{\epsilon\}^e = [B]^e \cdot \{u\}^e \tag{3.12}$$

in which, $\{\epsilon\}^e = [\epsilon_x, \epsilon_y, \gamma_{xy}]^T$ and $\{u\}^e = [u_1, u_2, u_3, v_1, v_2, v_3, u_4, u_5, u_6, v_4, v_5, v_6]^T$. The expanded form of above equation is shown in Equation 3.13.

$$\left\{ \begin{array}{c} \epsilon_x(x,y) \\ \epsilon_y(x,y) \\ \gamma_{xy}(x,y) \end{array} \right\} = \left[\begin{array}{cccccccccccc} N_{1,x} & N_{2,x} & N_{3,x} & 0 & 0 & 0 & N_{4,x} & N_{5,x} & N_{6,x} & 0 & 0 & 0 \\ 0 & 0 & 0 & N_{1,y} & N_{2,y} & N_{3,y} & 0 & 0 & 0 & N_{4,y} & N_{5,y} & N_{6,y} \\ N_{1,y} & N_{2,y} & N_{3,y} & N_{1,x} & N_{2,x} & N_{3,x} & N_{4,y} & N_{5,y} & N_{6,y} & N_{4,x} & N_{5,x} & N_{6,x} \end{array} \right] \cdot \left\{ \begin{array}{c} u_1 \\ u_2 \\ u_3 \\ v_1 \\ v_2 \\ v_3 \\ u_4 \\ u_5 \\ u_6 \\ v_4 \\ v_5 \\ v_6 \end{array} \right\} \tag{3.13}$$

In above equation, $N_{j,x}$ and $N_{j,y}$ are derivatives of the shape function N_i with respect to x and y.

$$\begin{aligned} N_{j,x} &= \frac{N_j(x,y)}{\partial x} = a_{j2} + 2a_{j4}x + a_{j5}y \\ N_{j,y} &= \frac{N_j(x,y)}{\partial y} = a_{j3} + a_{j5}x + 2a_{j6}y \end{aligned} \qquad j = 1, \cdots, 6 \tag{3.14}$$

Next, the interpolated strain (lhs of Equation 3.12) is integrated to obtain the average value. The integration is performed over each triangular region numerically.

$$\langle \epsilon_{ij} \rangle = \frac{1}{A_{tot}} \sum_e \int_{S_e} \epsilon_{ij}(x,y)\, dxdy \tag{3.15}$$

Gauss quadrature is used inside a triangular region. Because the strain is linear functions of x and y; only one integration point at the center of the triangle is needed.

$$\{\langle \epsilon \rangle\} = \frac{1}{A_{tot}} \cdot \sum_e \left[B(x_c, y_c)\right]_e \cdot \{u\}_e \cdot A_e \cdot W_c \tag{3.16}$$

In the above equation, W_c is the weight of the Gauss quadrature; it is equal to 1 in this case. (x_c, y_c) are the coordinates of the center point of the triangle. The Matlab implementation of the above algorithm is attached in appendix B.

Numerical verification:

The above procedure to estimate the average strain is based on an intuitive analogy. The validity and effectiveness needs to be tested before the algorithm can be used. In this section, a number of numerical examples are used to verify the algorithm. The general procedure is as follows: (1) a non-uniformly fluctuating displacement field is defined by some analytical expressions on a closed 2D region; (2) a fixed number of coordinate pairs are chosen randomly inside the region, the exact displacements at these random locations

are calculated using the proposed analytical expressions; (3) the average strain is evaluated using the displacement values at these random locations through Delaunay triangulation and displacement interpolation as described in the previous section; (4) step 2-3 are repeated a number of times to assess the average and the variance of the estimation; (5) exact average strain is evaluated using the analytical expression and the exact value is compared with the estimated value.

In the first example, Equation 3.17 is used to describe the displacement in the x-direction on a 2D region $[0.1, 1.1) \times [0.1, 1.1)$. The displacement filed is plotted in Figure 3.5. The average strain can be calculated analytically as shown in Equation 3.18.

$$u(x,y) = 0.1x + 0.04\sin(7x)\cos(11y) + 0.02\sin(23x)\sin(37y) + 0.007\sin(77x+71)\cos(101y-3) \tag{3.17}$$

$$\frac{1}{A}\int \epsilon_x dA = \int_{0.1}^{1.1}\int_{0.1}^{1.1} \frac{\partial u(x,y)}{\partial x} dxdy = 0.0982653 \tag{3.18}$$

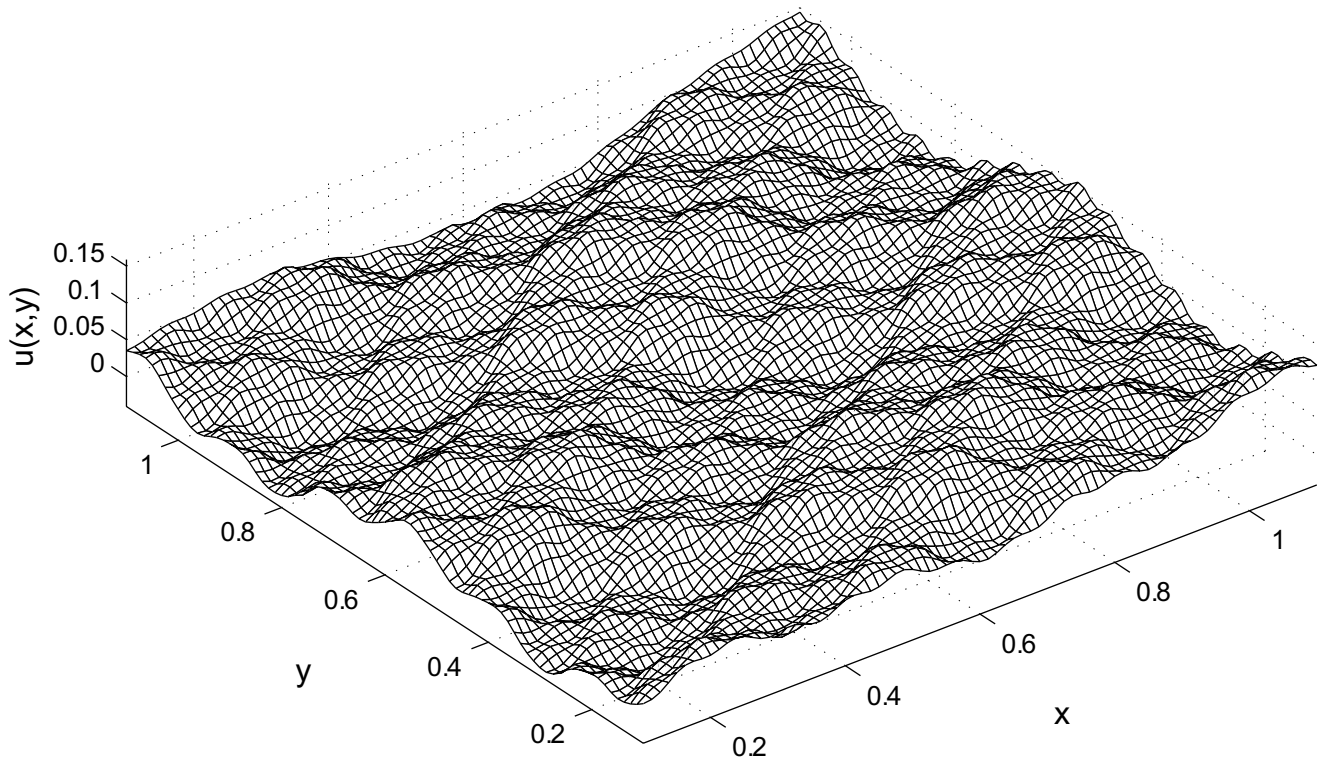

Figure 3.5: Non-uniform displacement field defined by equation 3.17

Next,the proposed algorithm is employed to estimate the average strain using the displacement values at a fixed number of arbitrary chosen sampling points. This procedure is repeated 25 times for every fixed number of sampling points. The average and variance of the estimation are plotted in Figure 3.6 against the number of sampling points. The result shows that the average of the estimations is within $\pm 5\%$ of the exact value if more than 10 random sampling points are used. The variance decreases with increasing number of sampling points but the magnitude of the variance generally exceeds $\pm 5\%$ range of the exact value.

Another numerical example is used to test the algorithm's capability to recover average shear strain. A non-uniform displacement field is described by Equations 3.19. The fluctuating u_x field and u_y field are plotted in Figures 3.7 and 3.8.

$$\begin{cases} u(x,y) = 0.1y + 0.04\sin(7x)\cos(11y) + 0.02\sin(23x)\sin(37y) + \\ \qquad\qquad 0.007\sin(77x+71)\cos(101y-3) \\ v(x,y) = 0.1x + 0.04\sin(6x)\cos(13y) + 0.02\sin(21x)\sin(31y) + \\ \qquad\qquad 0.007\sin(79x+71)\cos(103y-3) \end{cases} \tag{3.19}$$

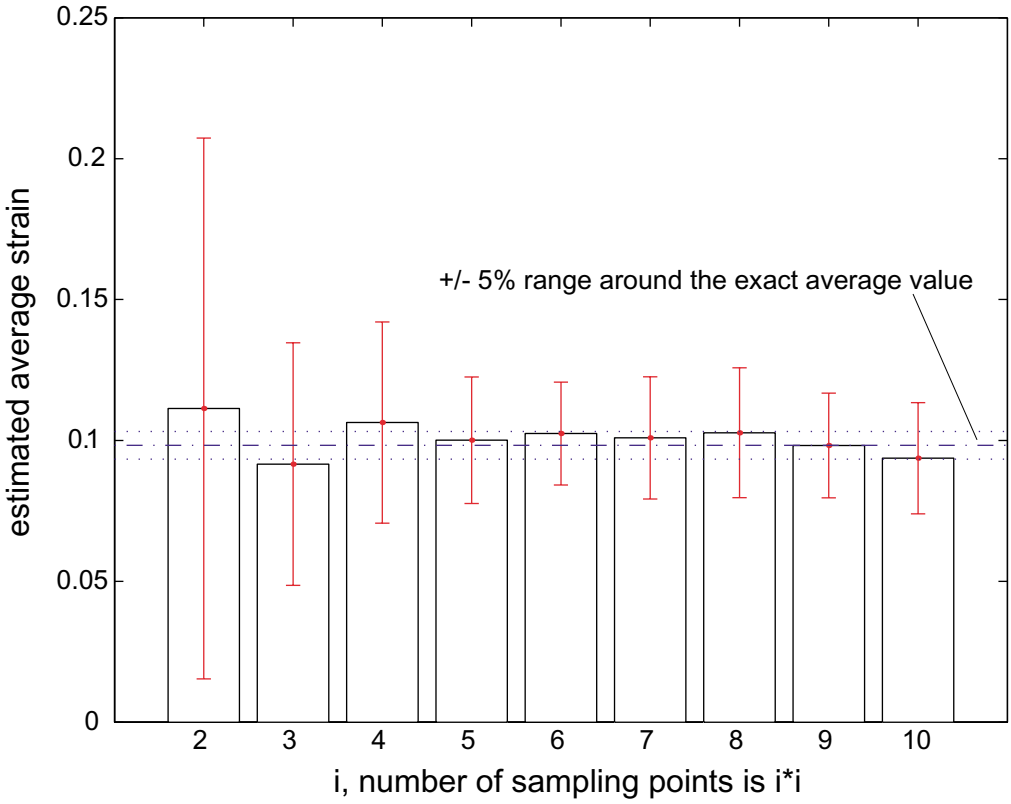

Figure 3.6: Estimated average strain: ϵ_x.

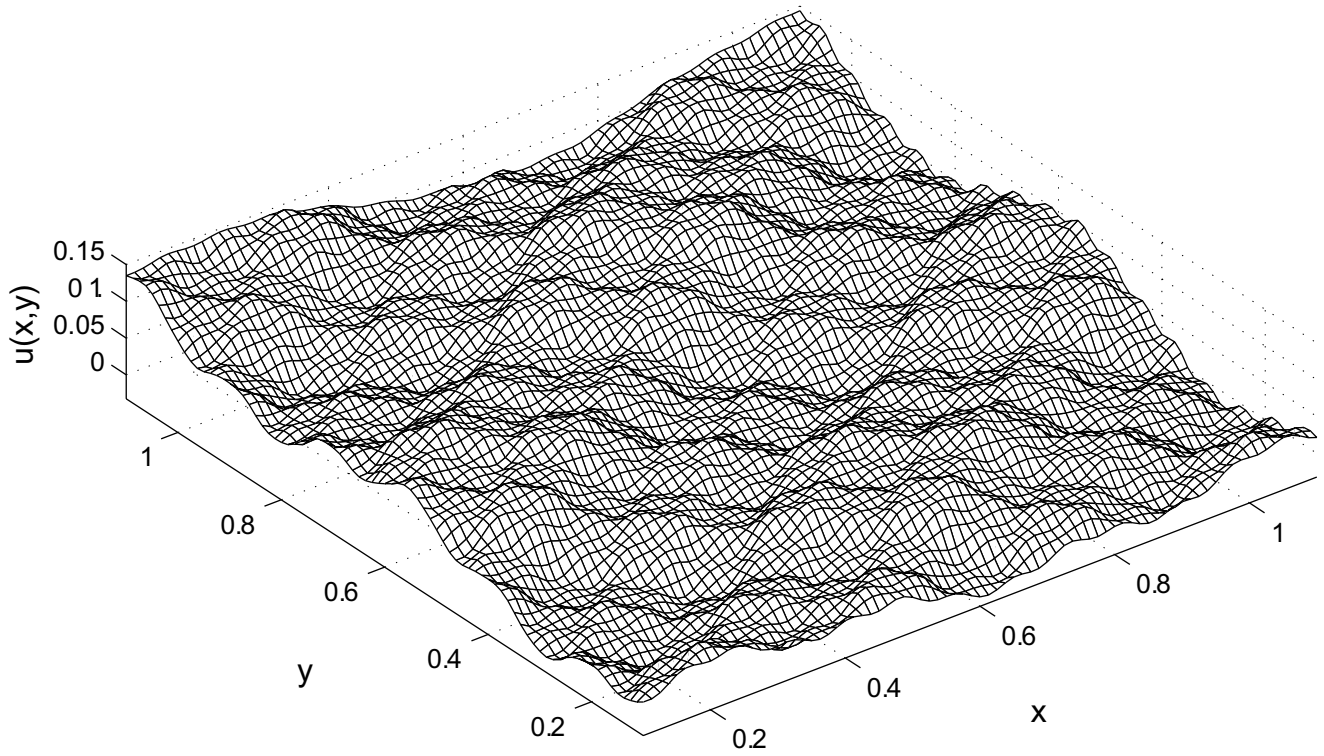

Figure 3.7: Non-uniform displacement field $u\,(x, y)$ defined in equation 3.19

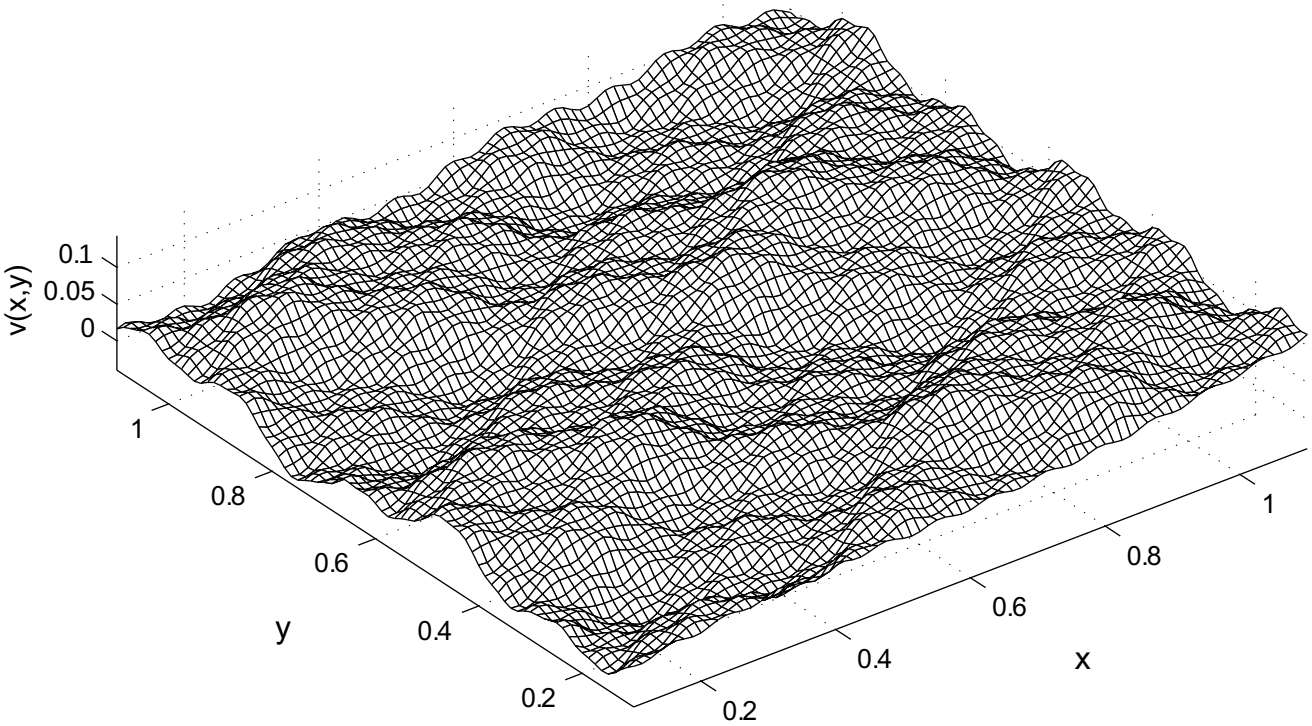

Figure 3.8: Non-uniform displacement field $v\,(x, y)$ defined in equation 3.19

The exact value of average shear strain can be evaluated analytically using the displacement field described by the above expressions:

$$\frac{1}{A}\int_A \gamma_{xy} dA = \int_{0.1}^{1.1}\int_{0.1}^{1.1}\left[\frac{\partial u\,(x,y)}{\partial y} + \frac{\partial v\,(x,y)}{\partial x}\right] dxdy = 0.200627 \tag{3.20}$$

Next, the proposed algorithm is used to estimate this average shear strain. The results are plotted in Figure 3.9 . Again, the average of the estimation is fairly close to the exact average value by sampling only less than 100 points. With increasing number of sampling points, the variation decreases and zooms in on the exact values.

In the above two verification examples, arbitrary points are thrown in at random locations and the displacement values are evaluated *exactly* using the analytical expressions at the chosen locations. To test the robustness of the algorithm, in the following two examples, a random noise[1] is added to the exact displacement value at each chosen location; the magnitude of the noise, $|err|$, is about 10% of the maximum displacement.

Following the same procedure, the estimation of average tensile strain and average shear strain are calculated and plotted in Figure 3.10 and 3.11. The result shows that the estimations are not adversely affected except for the case when only 4 sampling points are used. This indicates that the algorithm will be able to tolerate a certain level of error in the displacement solution if the error is "uniformly" distributed.

These examples have shown that reasonably good estimation of the average strain can be obtained by taking the average of a number of estimations on less than 100 sampling points. The results also suggest that, repetitive application of the algorithm for a number of times over random sets of sampling points that are distributed (not-clustered) through the region is necessary to get a good estimation.

[1] A uniformly distributed random number over the interval $\left(-\frac{err}{2}, \frac{err}{2}\right)$.

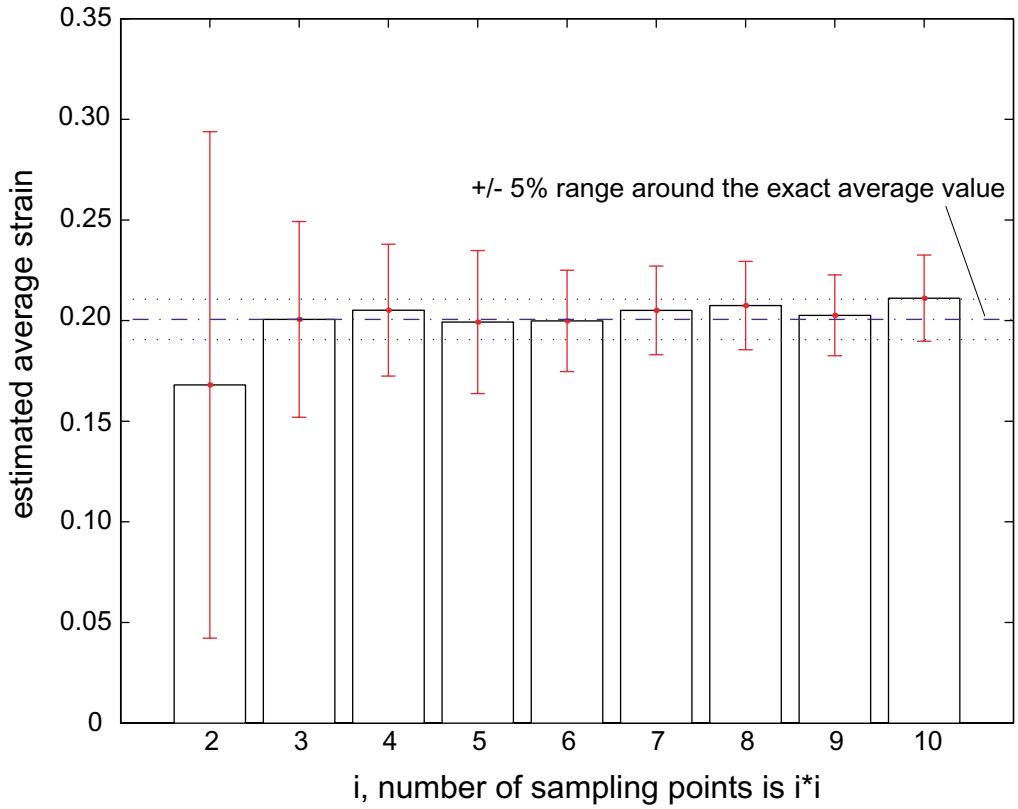

Figure 3.9: Estimated average shear strain: γ_{xy}.

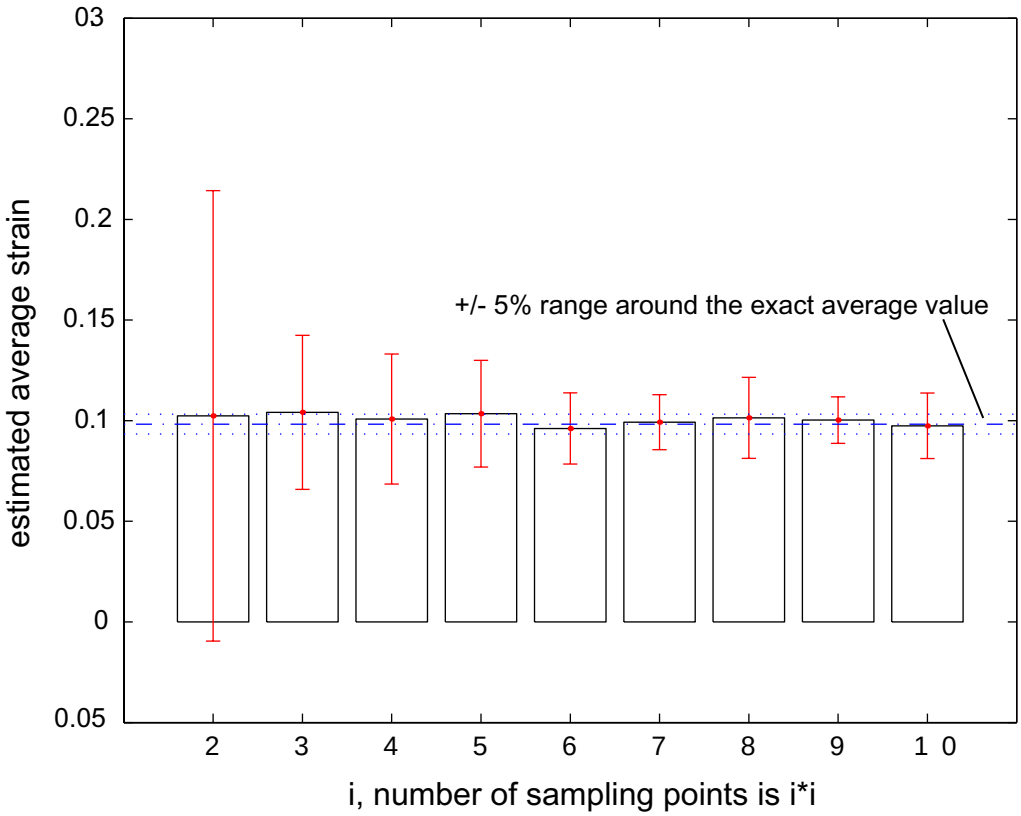

Figure 3.10: Effect of random errors on the estimated average strain: ϵ_x.

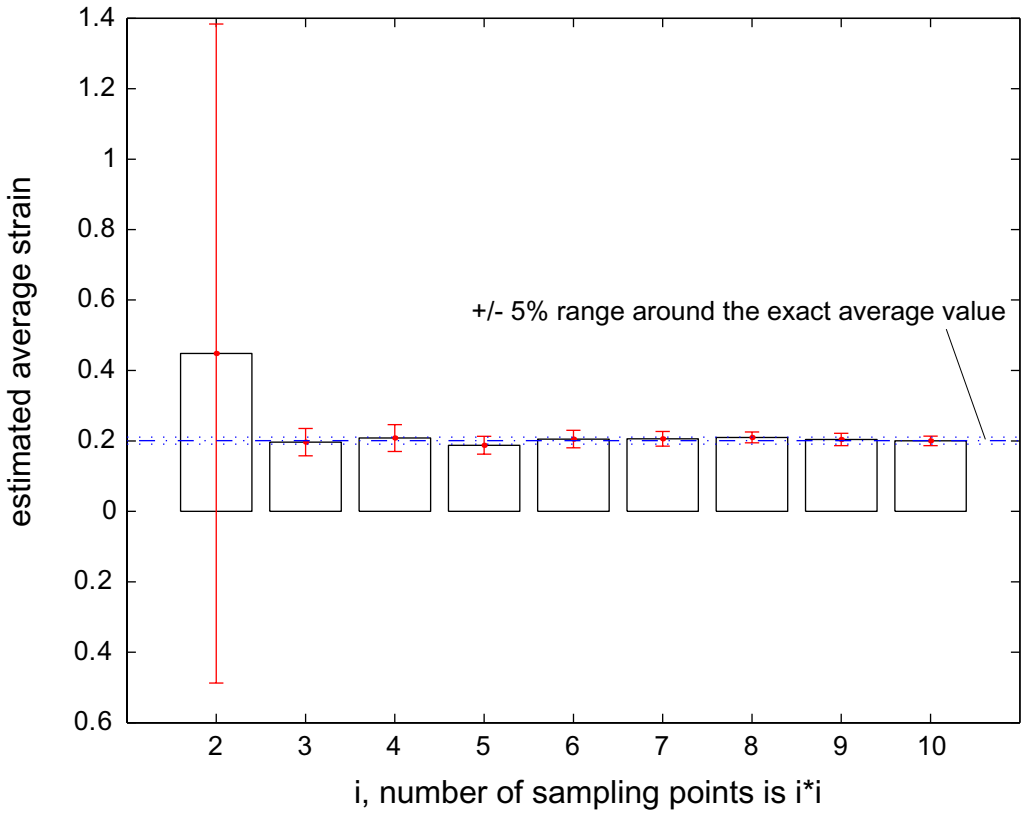

Figure 3.11: Effect of random errors on the estimated shear strain: γ_{xy}.

The displacement field in a heterogeneous material can be decomposed into two parts: (1) a randomly fluctuating part representing the effects local morphological (geometry and material) irregularities and (2) a smooth part representing the long-range order of the displacement as a function of location. The process to obtain the average strain is equivalent to a smoothing process, which reveals the characteristics of the smooth part of the displacement field. The author has shown that it is possible to obtain a reasonably good estimation of the average strains of a irregular displacement field without knowing accurately the displacements at every microscopic material points. This is a great advantage in micromechanics modeling because the burden to model excessive morphological details at the microscopic level is relieved if the only purpose is to obtain average strains.

3.1.3 The Strain Energy Equivalence Principle

The strain energy equivalence principle states that *the strain energy calculated using the average stress and the average strain has to equal to the strain energy calculated using the micro-stress and the micro-strain over a RVE,* as expressed in the following equations:

$$U_{RVE}\left(\langle\sigma_{ij}\rangle, \langle\epsilon_{ij}\rangle\right) = U_{RVE}\left(\sigma_{ij}, \epsilon_{ij}\right) \tag{3.21}$$

It is a natural consequence of *the principle of the conservation of energy* and it is used here to establish connections between average quantity and microlevel quantity. Assume the constitutive relation of the effective medium is an elastic one described by Hooke's law:

$$\langle\sigma_{ij}\rangle = C_{ijkl}\langle\epsilon_{kl}\rangle. \tag{3.22}$$

The average stress $\langle\sigma_{ij}\rangle$ in equation 3.21 can be eliminated by substituting in the effective

properties.

$$U_{RVE}\left(\langle\epsilon_{ij}\rangle; C_{ijkl}\right) = U_{RVE}\left(\sigma_{ij}, \epsilon_{ij}\right) \tag{3.23}$$

After solving the BVP defined on a RVE, the rhs of the above equation can be evaluated. Using the scheme presented in the previous section, the average strain $\langle\epsilon_{ij}\rangle$ can also be estimated from the displacement solutions to the BVP. Now, Equation 3.23 has only C_{ijkl} as unknowns. By applying a set of different boundary conditions on the RVE, we can setup and solve a set of BVPs on the same RVE and estimate the average strain and strain energy for each case; by substituting the estimated average strain and strain energy into Equation 3.23, we can obtain a set of linear independent equations in terms of the components of C_{ijkl}; the number of independent equations can be selected to match the number of unknown components in the effective elastic tensor C_{ijkl}; the effective elastic tensor can thus be determined by solving this simultaneous set of linear equations.

By assuming plane stress condition and a 2D linear elastic anisotropic constitutive law, we have derived equations to solve for the 2D effective elastic properties. The details are presented in the following section.

2D plane stress formulation:

The general form of strain energy density for a linear elastic material is expressed as:

$$V = \frac{1}{2}\sigma_{ij}\epsilon_{ij} = \frac{1}{2}C_{ijkl}\epsilon_{ij}\epsilon_{kl} \tag{3.24}$$

In the case of 2D plane stress, assume the effective properties are generally anisotropic, so that the constitutive law expressed in average stress and average strain is the following:

$$\begin{Bmatrix} \langle\sigma_{11}\rangle \\ \langle\sigma_{22}\rangle \\ \langle\tau_{12}\rangle \end{Bmatrix} = \begin{bmatrix} C_{11} & C_{12} & C_{16} \\ C_{12} & C_{22} & C_{26} \\ C_{16} & C_{26} & C_{66} \end{bmatrix} \cdot \begin{Bmatrix} \langle\epsilon_{11}\rangle \\ \langle\epsilon_{22}\rangle \\ \langle\gamma_{12}\rangle \end{Bmatrix} \tag{3.25}$$

The strain energy in this case is simplified to:

$$U = \frac{1}{2}\langle\sigma_{11}\rangle\langle\epsilon_{11}\rangle + \frac{1}{2}\langle\sigma_{22}\rangle\langle\epsilon_{22}\rangle + \frac{1}{2}\langle\tau_{12}\rangle\langle\gamma_{12}\rangle \tag{3.26}$$

Substituting Equation 3.25 into Equation 3.26 to eliminate average stresses yields:

$$\begin{aligned} U = \frac{1}{2}C_{11}\langle\epsilon_{11}\rangle^2 + \frac{1}{2}C_{22}\langle\epsilon_{22}\rangle^2 + \frac{1}{2}C_{66}\langle\gamma_{12}\rangle^2 + C_{12}\langle\epsilon_{11}\rangle\langle\epsilon_{22}\rangle + \\ C_{16}\langle\epsilon_{11}\rangle\langle\gamma_{12}\rangle + C_{26}\langle\epsilon_{11}\rangle\langle\gamma_{12}\rangle \end{aligned} \tag{3.27}$$

By applying six independent[2] sets of boundary conditions on the RVE, such as those listed in Equation 3.29, six independent linear equations are obtained; they can be solved to obtain $\{C_{11}, C_{22}, C_{12}, C_{16}, C_{26}, C_{66}\}$.

$$u_\alpha = \epsilon_{\alpha\beta}x_\beta, \text{ on the boundary of the RVE} \tag{3.28}$$

in which,

$$[\epsilon_{\alpha\beta}] = \left\{ \begin{bmatrix} 1 & 0 \\ 0 & 0 \end{bmatrix}, \begin{bmatrix} 0 & 0 \\ 0 & 1 \end{bmatrix}, \begin{bmatrix} 0 & 1 \\ 1 & 0 \end{bmatrix}, \begin{bmatrix} 1 & 1 \\ 1 & 0 \end{bmatrix}, \begin{bmatrix} 0 & 1 \\ 1 & 1 \end{bmatrix}, \begin{bmatrix} 1 & 0 \\ 0 & 1 \end{bmatrix} \right\} \tag{3.29}$$

The compliance matrix can be calculated by inverting the stiffness matrix.

[2]Independent in the sense that the resulting equations expressed by Equation 3.27 are linear independent.

$$\begin{bmatrix} S_{11} & S_{12} & S_{16} \\ S_{12} & S_{22} & S_{26} \\ S_{16} & S_{26} & S_{66} \end{bmatrix} = \begin{bmatrix} C_{11} & C_{12} & C_{16} \\ C_{12} & C_{22} & C_{26} \\ C_{16} & C_{26} & C_{66} \end{bmatrix}^{-1} \tag{3.30}$$

The engineering constants are then calculated:

$$E_{11} = \frac{1}{S_{11}} \tag{3.31}$$

$$E_{22} = \frac{1}{S_{22}} \tag{3.32}$$

$$G_{12} = \frac{1}{S_{66}} \tag{3.33}$$

$$\nu_{12} = -\frac{S_{12}}{S_{11}} \tag{3.34}$$

$$\nu_{21} = -\frac{S_{21}}{S_{22}} \tag{3.35}$$

This approach can be straightforwardly extended to the 3D case, in which there are 21 unknown components. So 21 sets of boundary conditions need to applied to the 3D RVE.

In the next section, the methodology described is applied to a class of highly porous systems with a microstructure that resembles random fibrous network.

3.2 Random Fibrous Network

A random fibrous network with point bonds characterizes the microstructures of a wide variety of materials, which are crucial to our social welfare. Examples are papers, filters, thermal/acoustic insulators, LiMH battery substrates, hydrogen storage substrates etc. The microstructure of some naturally occurring materials, such as trabecular bone and biological tissues, also resembles a fibrous network. Mechanical stiffness and strength of these materials are usually essential properties for them to perform their other intended functions.

The structural stiffness and strength derive from the fibers and point bonds between the fibers. Two distinctive features of these materials are (1) high porosity and (2) stochastic microstructure. The research and development of above materials have been largely led by the material society. The design and manufacturing philosophy of these material has been primarily an empirical one, which depends on numerous try and error processes. Recently, the relationship between the fibrous network microstructure and macro material properties has interested researchers in mechanics circle. Any light shed on above problem could have great practical implication in the design of fibrous network materials with optimal cost performance.

The typical processing route for such materials is the following: tiny fibers are suspended and mixed with bonding agent in fluids and poured into a porous mold. As the fluid water is removed through the pores of the mold, the fiber intertwine to form a structure that hold its shape but contain large open space. When this structure is dried and consolidated, the fiber bonds together where they contact each other to give the material stiffness and strength, but most of the open space remains. The type of fibers commonly used include cellulosic (e.g., paper), ceramic (hot gas filters, insulators), carbon (hydrogen storage substrate), metal (e.g., Ni fiber in LiMH battery substrate).

Figure 2.33 shows the microstructure of a ceramic candle filter material. The fibers shown are alumina fiber (Saffil) with a diameter from 2 to 5 microns. The structure is formed by a sol-gel process, in which a chopped Saffil fiber slurry mixed with an alumina bonding agent is deposited on an substrate and dried. The green part is then fired at high temperature. The final product has a 70% porosity. Aslo shown on the picture is the random arrangement of the fibers. A number of processing parameters can be identified in the process, e.g. the length of the chopped fibers, the volume fraction of chopped fiber, the volume fraction of bonding agent. Usually the slurry flowing direction will exert an preferred orientation of the chopped fibers. The questions are how these parameters would affect the effective properties

of the final product. And these types of question are also relevant to other materials that resemble a fibrous network.

3.2.1 Literature Review

There have been some research efforts on cellular materials, which bear close similarity to the material described above, especially the open cell cellular material. Ashby and Gibson [21] have made significant contributions to the mechanics of cellular material. They argued that the effective properties of a low density cellular material is correlated to its relative density by following equation:

$$\frac{E}{E_s} = C\left(\frac{\rho}{\rho_s}\right)^n \tag{3.36}$$

In which, E is effective modulus, E_s is the modulus of the underlying solid; ρ is the nominal density, and ρ_s is the density of the underlying solids. n is generally believed to be in the range $(1, 3)$.

Cox [14] appears to be the first to publish a micromechanical model on fibrous network. He analyzed the effect of orientation of the fibers on the stiffness and strength of paper. He showed that these effects can be represented completely by the first three Fourier coefficients, as shown in Equation 3.37 in a planar case and the first fifteen spherical harmonics in the 3D case. In his analysis, he assumed (1) no bonding between the cross over point of fiber (2) fiber deforms in tension and compression only (2) uniform deformation throughout the volume. A number of researchers have focused on the the micromechanical modeling of compressional response of fibrous network, following the pioneering work of van Wyk [65]. He translated global compressive strain into the bending strain of individual fibers, while completely neglecting the extension, compression, and torsion of individual fibers. Lee and

Lee [37] take the anisotropic nature of fiber network into account by introducing a mean-free fiber length parameter. They succeeded in relating the initial compressional modulus and Poisson's ratio to the ODF and properties of fibers. Carnabya and Pan [6] introduced a slippage mechanism in addition to the bending of fiber segment. This enabled them to estimate the hysteresis in a compression-recovery cycle.

$$\pi f(\theta) = 1 + a_1 \cos(2\theta) + a_2 \cos(4\theta) + b_2 \sin(4\theta) \tag{3.37}$$

Kallmes and his coworkers [34, 35] later extended Coxs work by applying probability theory to fiber bonding points, and to the free fiber length between fiber bonding bonds. Nissan [43] studied the strength of fiber bonding point and its relation to macro level properties. These research works mentioned above have been targeted primarily on the performance of paper. Chen and Duckett [9], Pan and Carnaby [6] have studied general fibrous assemblies in a broader perspective.

Ostoja-Starzewski[45, 46, 44] studied the effective elastic properties of a planar Delaunay network. Uniform deformation was assumed in their calculation of the effective properties. They also calculated the upper and lower bound of the effective properties using the Voigt and Reuss approximation.

Some recent work on fibrous include those of Sastry *et al* [54, 55, 67, 68, 69, 70] and Garboczi *et al* [20, 51, 40]. Sastry studied fibrous battery substrates. To simulate the random microstructure of a battery substrate, stochastic fiber networks were generated by a computer code and then analyzed by using finite element method. Each fiber segment was modeled as a frame element with both axial and flexure rigidity. Artificial periodic boundary conditions have been used in their simulated network models. They found that fiber aspect ratio has a significant influence on the effective network moduli. Garboczi has used an image-based numerical procedure to study the effective properties of porous fibrous material. He has used

a code to translate the 2D or 3D image directly into a FE model by converting each pixel in the image into a solid element. And the material properties for each pixel are determined by the gray level.

3.2.2 The FIBNET Simulation Program

To reveal the relationship between their microstructure and their effective mechanical properties, the general micromechanics approach described in the above sections is applied to simulate a random fibrous network. A representative volume element (RVE) approach is adopted. A novel treatment of the boundary conditions on the RVE is developed in order to avoid some commonly used but oversimplifying assumptions, such as uniform displacement or uniform traction. The finite element procedure is used to solve the boundary value problem defined on the RVE. The average strain and the total strain energy inside the RVE are derived from the finite element solution. A novel method to estimate the average strain of the RVE is introduced. Finally, the macro-effective elastic properties of the RVE are obtained by using the strain energy equivalence principles. The micromechanical approach obviously has the advantage of relating the global material parameters to the microstructure: fiber orientation distribution, fiber properties, bonding properties, etc.

To deal with the complex micromechanics simulation of stochastic fibrous networks, a practical software tool called FIBNET (FIBrous NETwork) has been implemented. This computer code addresses model generation and the post-processing part of the simulation task. The solution of the BVP is done by commercial finite element solvers; currently, interfaces to ABAQUS and ANSYS have been implemented. Given a statistical description of a random fibrous network, such as fiber length distribution, fiber orientation distribution, fiber volume fraction, etc., the FIBNET code generates a graph (vertexes and edges) representation of the fibrous network that bears the same statistical characteristics. Combined with material

properties data and boundary conditions, the graph representation is translated into a finite element model, which is subsequently solved by the chosen solver. The solution of the BVP is parsed into the FIBNET program in the post-processing process; the average values of the field variables inside an arbitrary chosen observation window are then calculated and the effective elastic properties are derived from these average field variables. The FIBNET code has made it possible to perform various statistical and parametric studies such as the ensemble average of effective elastic properties, the effect of fiber orientation distribution on the effective elastic properties, etc.

One function of the FIBNET code is to generate "realistic" models of a two-dimensional fibrous network. The algorithm mimics the typical manufacturing process. Fibers with random length and orientation are assigned to random locations in a closed 2D region. The cross-over points of the fibers are identified and represented by vertexes in the graph and the fibers are represented as edges in the graph. A very efficient graph generation algorithm has been developed. This fast algorithm allows the FIBNET code to simulate fibrous networks containing as many as tens of thousands of fibers with a reasonable turn-around time on a regular PC platform. It was noticed that there exist fiber segments that have one free ends (branches). They can not be loaded mechanically because of the free end. To reduce the size of the model and to save computational time, they are eliminated from the graph representation. A computer generated random fibrous network is shown in Figure 3.13 and Figure 3.14 shows the network after non-load-bearing branches are trimmed off. After the random network is generated, a set of points on the boundary are identified and uniform boundary conditions are applied. Several sets of "independent" boundary conditions are applied to the RVE. Figure 3.15 to 3.16 show the deformed shape of a RVE under six different sets of boundary conditions. After the solution, the effective properties can be calculated on an arbitrary chosen observation window inside the RVE. To do this, all nodal points inside the RVE are identified and a random subset of these points are chosen to

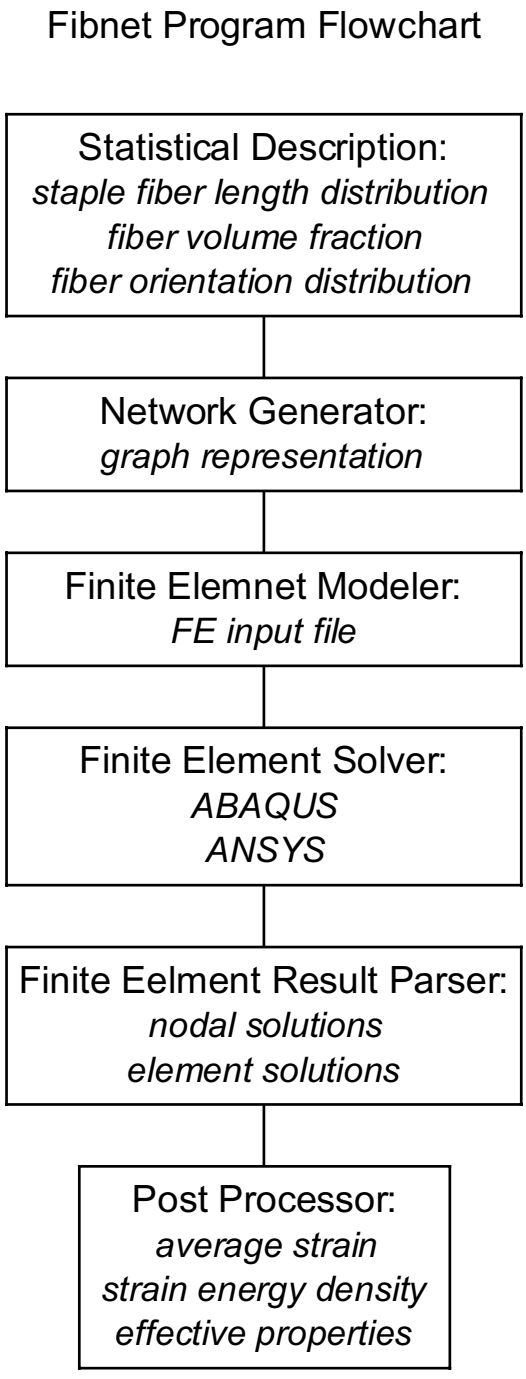

Figure 3.12: The structure of FIBNET program

calculate the average strain inside the window, this procedure is repeated a number of times and the average values are used as the estimation of the average strain. The strain energy inside the window is also calculated and finally the strain energy equivalence principle is used to solve for the unknown components of the elastic tensor.

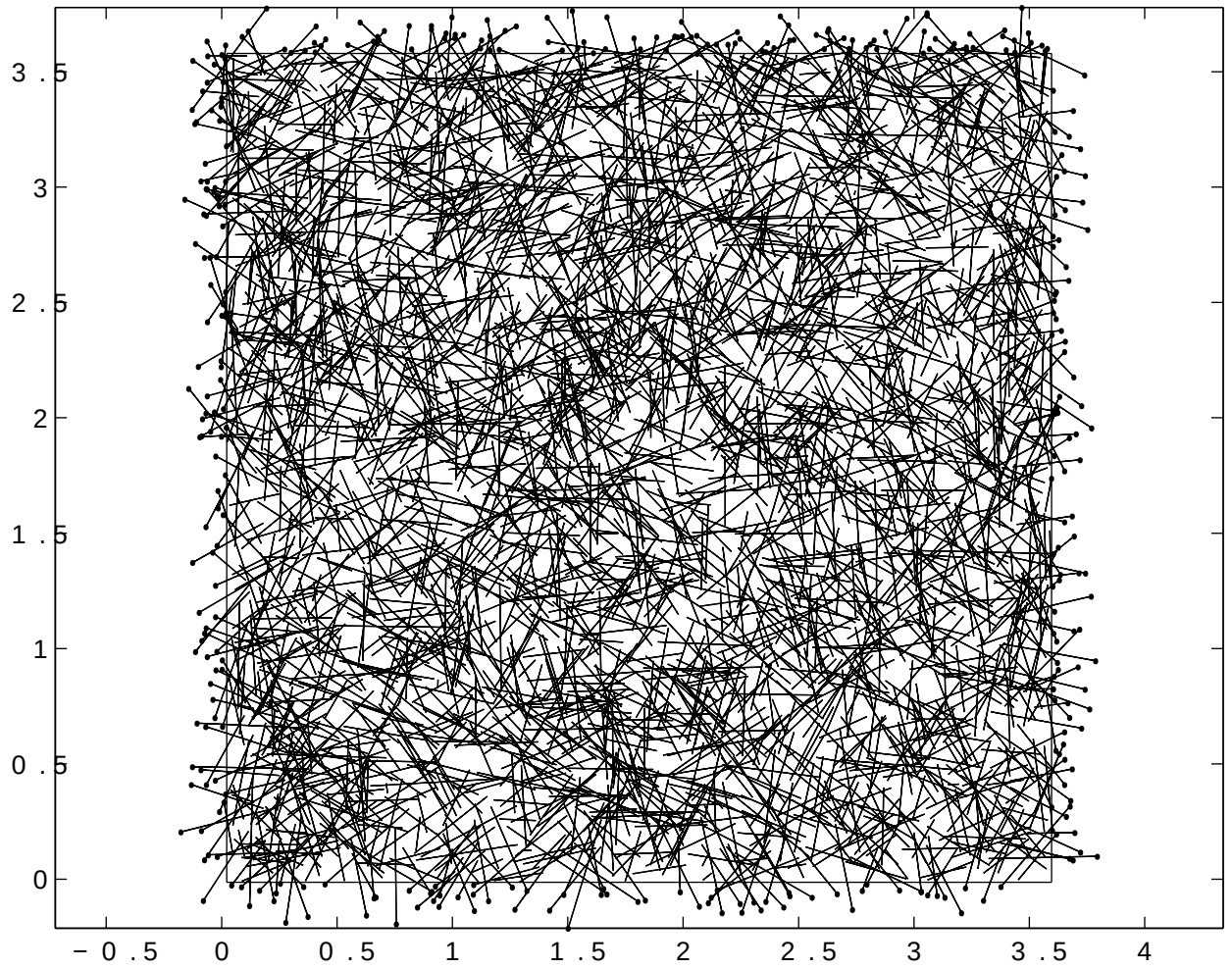

Figure 3.13: Random fibrous network generated by the FIBNET code. Dotted points are identified boundary points of the RVE.

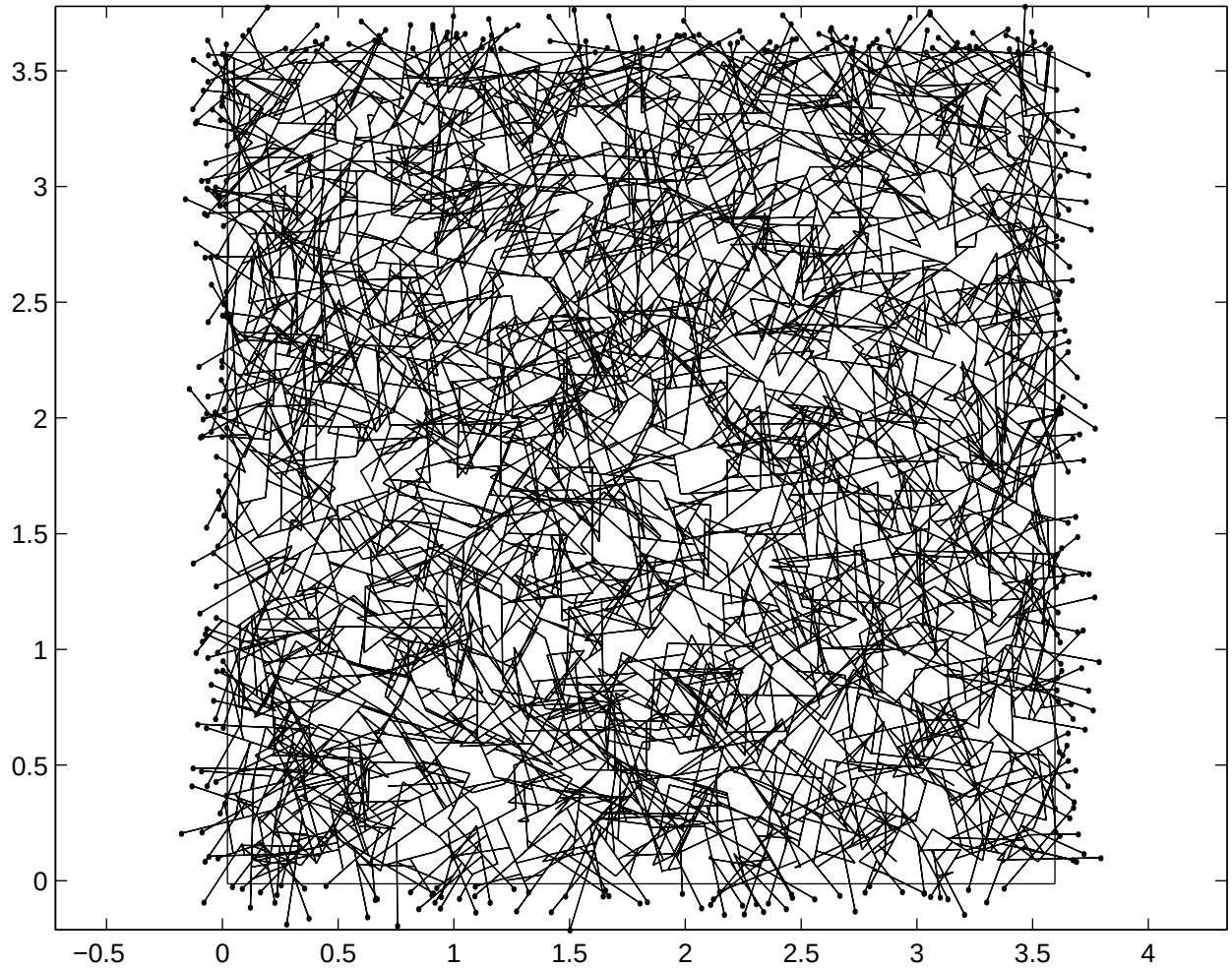

Figure 3.14: Random fibrous network after trimming. Non-load-bearing fiber segments are eliminated.

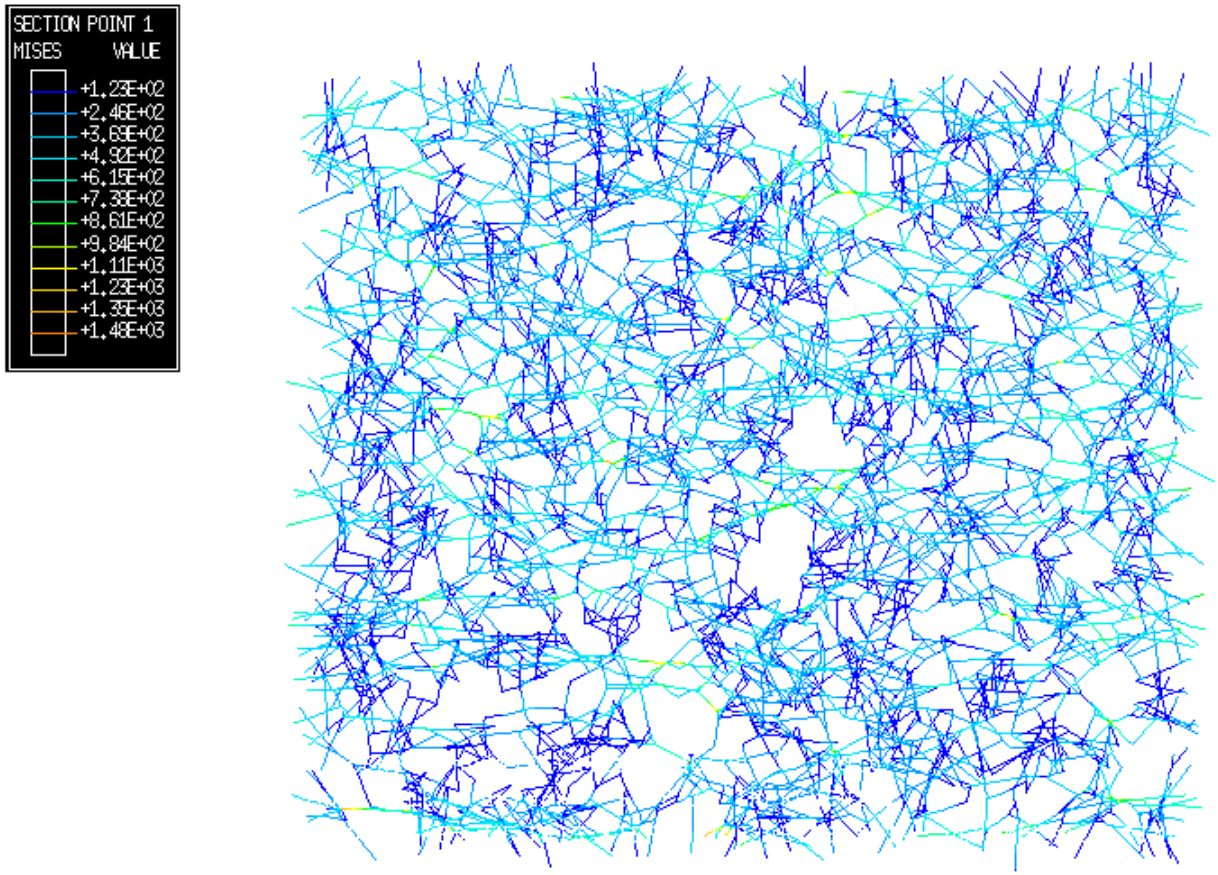

Figure 3.15: Deformed shape of a simulated random fibrous network: $\epsilon_x = 0.01$

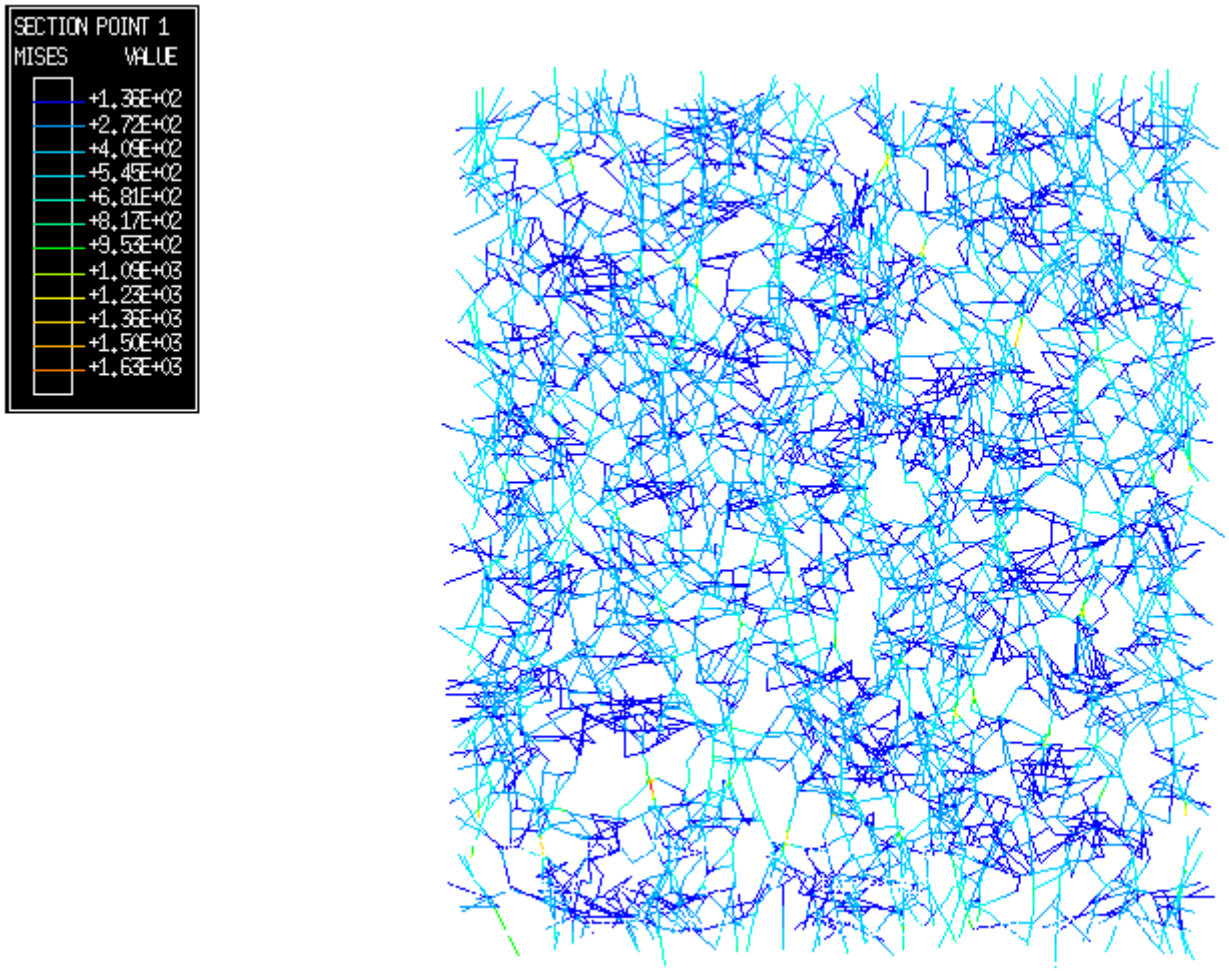

Figure 3.16: Deformed shape of a simulated random fibrous network: $\epsilon_y = 0.01$

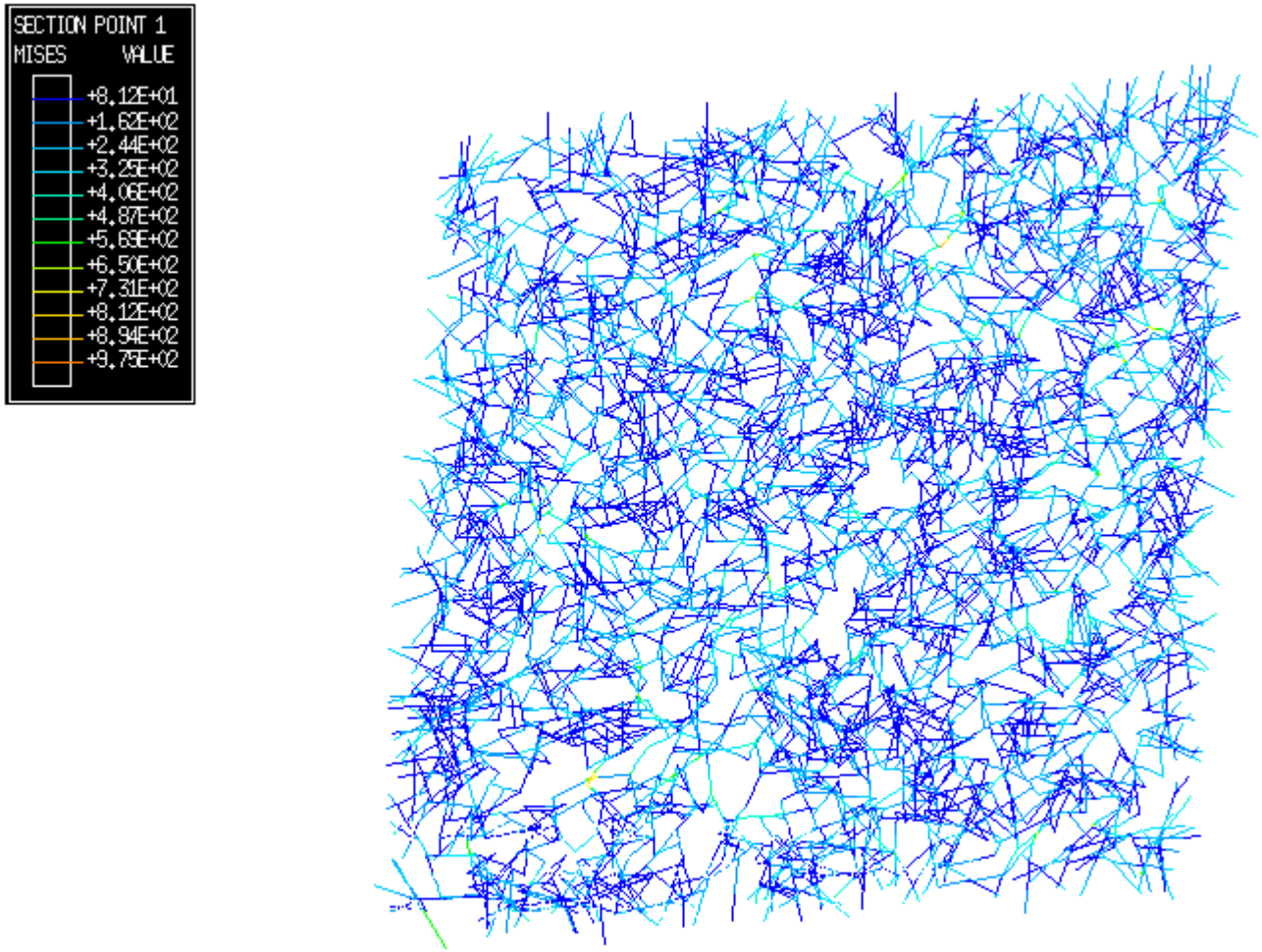

Figure 3.17: Deformed shape of a simulated random fibrous network: $\gamma_{xy} = 0.02$

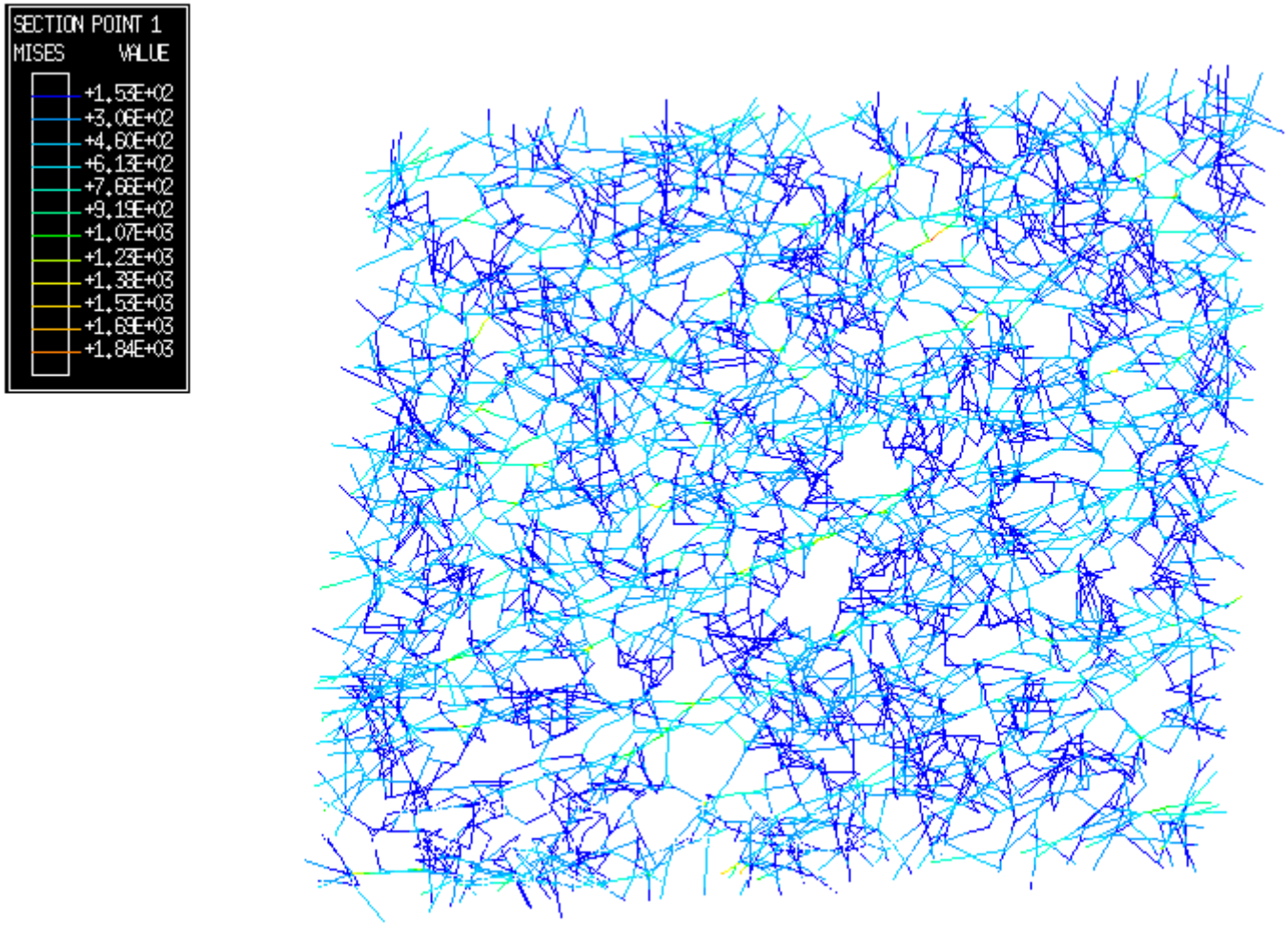

Figure 3.18: Deformed shape of a simulated random fibrous network: $\epsilon_x = 0.01, \gamma_{xy} = 0.02$

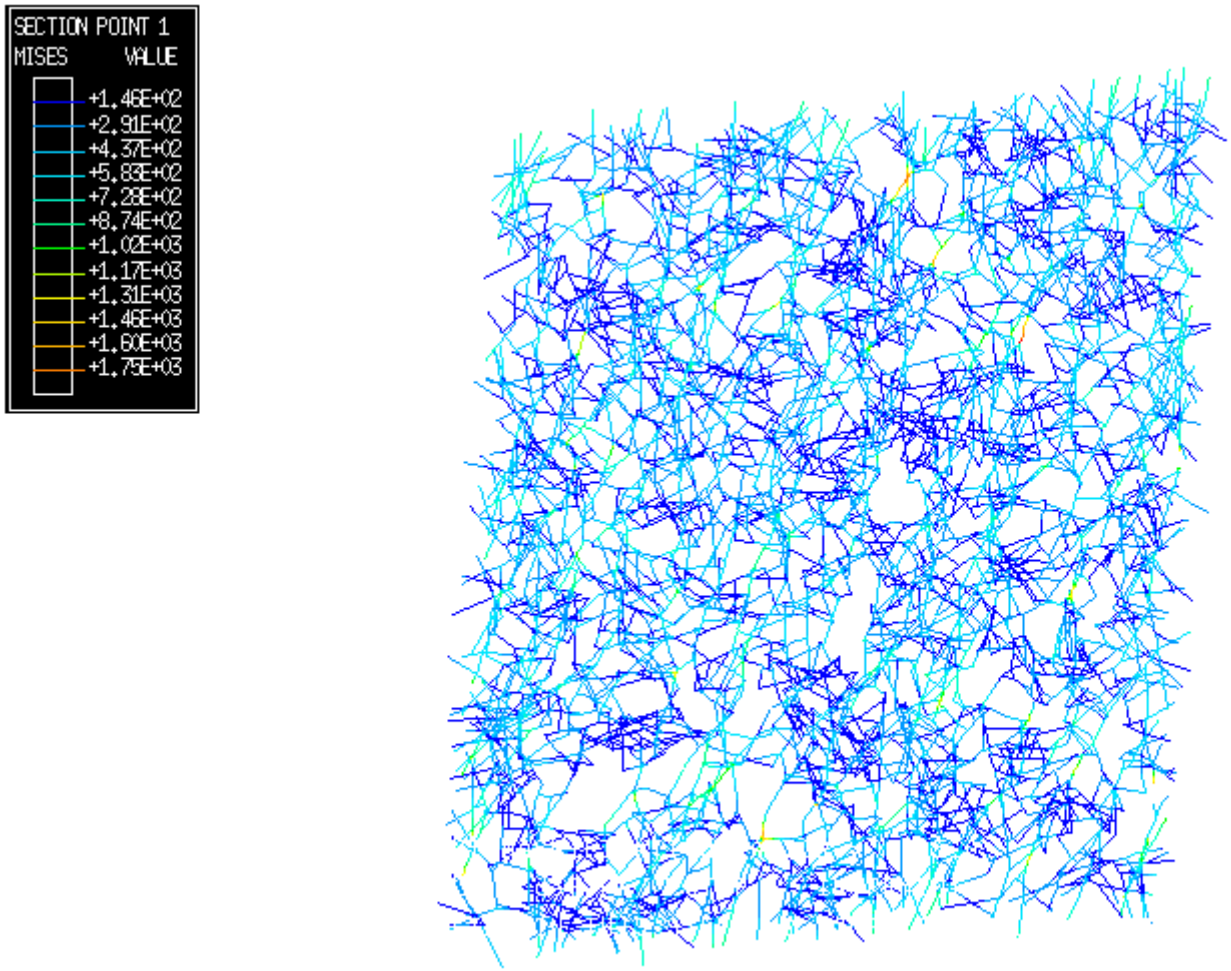

Figure 3.19: Deformed shape of a simulated random fibrous network: $\epsilon_y = 0.01, \gamma_{xy} = 0.02$

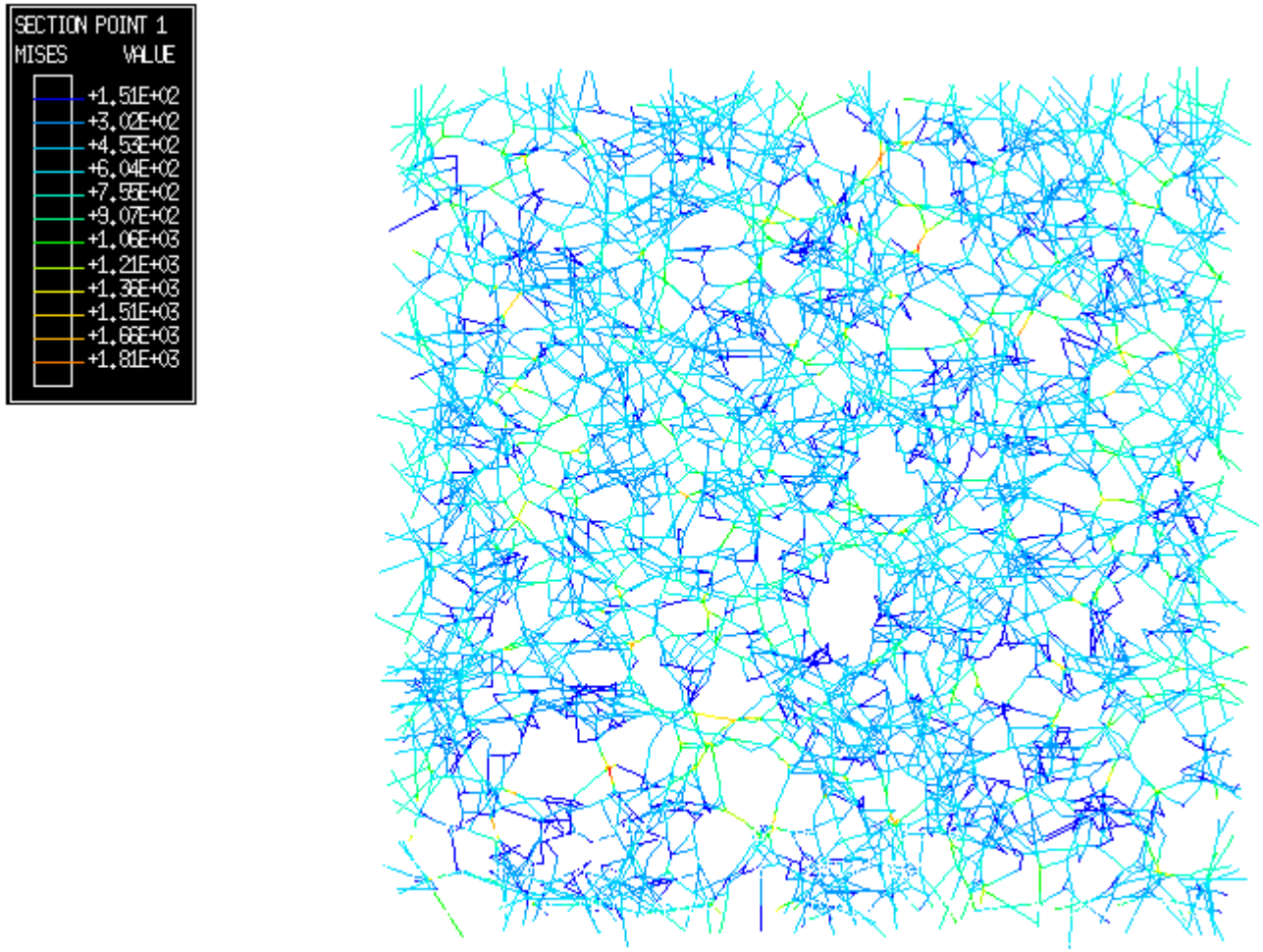

Figure 3.20: Deformed shape of a simulated random fibrous network: $\epsilon_x = 0.01, \epsilon_y = 0.01$

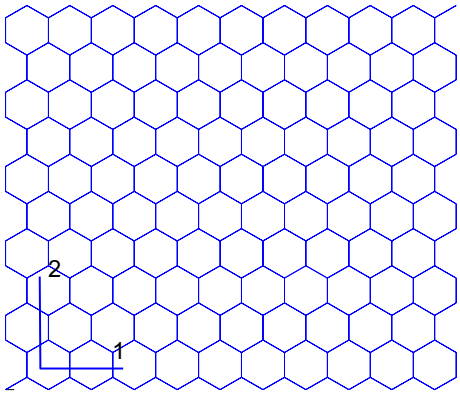

Figure 3.21: Cellular material with honeycomb microstructure.

3.2.3 Numerical Verification

There is no exact solution for random fibrous network. To verify the approach, we have chosen to apply the algorithm to a honeycomb material for which there is a closed-from estimation of effective elastic properties based on a mechanics of material analysis on a unit cell.

A cellular material with regular honeycomb microstructure is shown in Figure 3.21 . The microstructure of the honeycomb material is defined by four geometric parameters, i.e., h, l, t, and θ as illustrated in Figure 3.22. Ashby and Gibson [21] estimated the in-plane elastic moduli of the honeycomb material as functions of the above parameters and E_s, the modulus of the underlying solid material. Their closed form estimations are expressed in Equation 3.38 to 3.41.

$$\frac{E_1^*}{E_s} = \left(\frac{t}{l}\right)^3 \frac{\cos\theta}{(h/l + \sin\theta)\sin^2\theta} \tag{3.38}$$

$$\frac{E_2^*}{E_s} = \left(\frac{t}{l}\right)^3 \frac{(h/l + \sin\theta)}{\cos^3\theta} \tag{3.39}$$

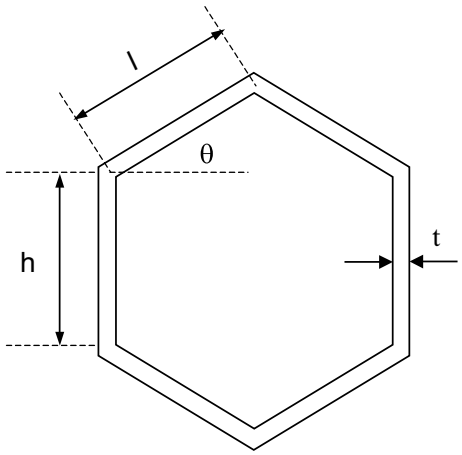

Figure 3.22: Unit cell of a honeycomb material.

$$\nu_{12}^{*} = \frac{\cos^2\theta}{(h/l + \sin\theta)\sin\theta} \tag{3.40}$$

$$\frac{G_{12}^{*}}{E_s} = \left(\frac{t}{l}\right)^3 \frac{(h/l + \sin\theta)}{(h/l)^2 (1 + 2h/l)\cos\theta} \tag{3.41}$$

These equations have been checked with experimental results with generally good agreement as shown in Figure 3.23 and 3.24. For regular honeycomb material ($h = l$), the equation predicts that $E_1 = E_2$ and $\nu_{12} = \nu_{21} = 1$. The Poisson's ratio predicted violates the physical limitation that requires that $1 - \nu_{12}\nu_{21} > 0$ [33]. This may be a result of simplified boundary conditions on the unit cell used in the analysis.

The author used the FIBNET code to predict a honeycomb structure defined by the parameters listed in Table 3.1. The Ashby & Gibson prediction and the FIBNET result calculated in three different observation windows are listed in Table 3.2. The FIBNET prediction shows that modulus in the 1-direction is slightly higher than the modulus in the 2-direction and at the same time ν_{12} is higher than ν_{21}. The product of two Poisson's ratios predicted is checked and found to be within the physical limitation. The FIBNET code predicted shear moduli

are higher than the analytical estimations; the experimental data shown in Figure 3.24 are also consistently higher than the analytical estimations. Experimental data of E_1 and E_2 have shown large variance; as a result, both of the prediction, analytical and FIBNET, fall into the range of scattered experimental data observed.

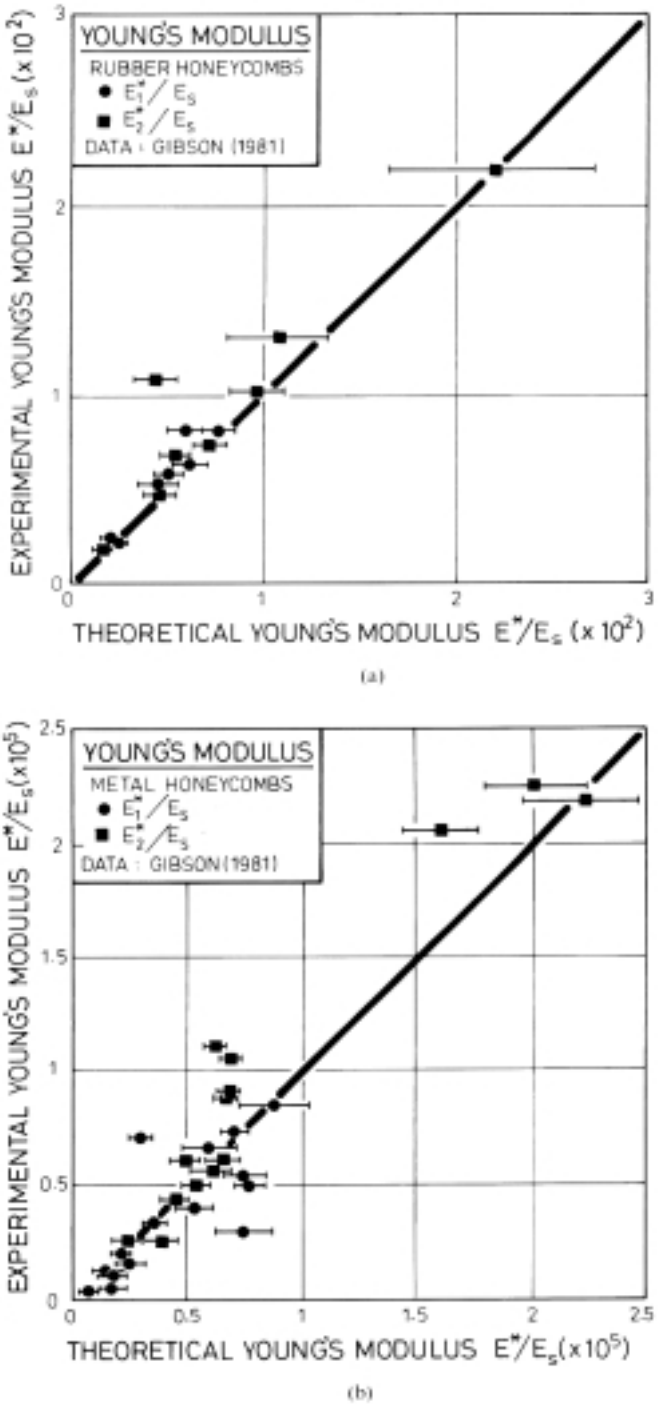

Figure 3.23: Young's moduli in X_1 and X_2 directions for: (a) elastomeric honeycombs; and (b) metal honeycombs [21]. Theoretical moduli refer to the moduli predicted by equation 3.38 and 3.39.

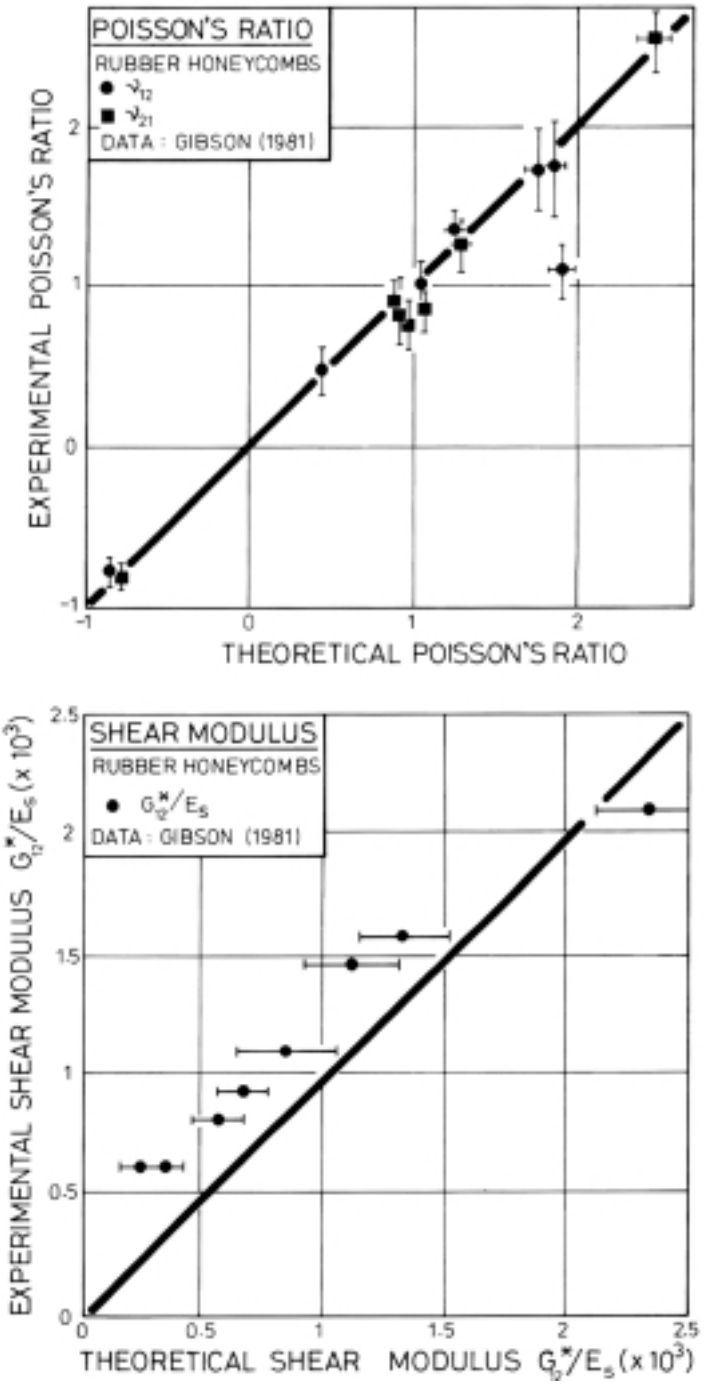

Figure 3.24: The in-plane Poisson's ratio and shear moduli for elastomeric honeycombs [21]. Theoretical values refer to the values predicted by equation 3.40 and 3.41. The measured shear moduli are systematically a little higher than those predicted by the simple closed-form solutions.

Table 3.1: Geometric parameters of honeycomb materials.

h	l	t	θ	E_s
0.3	0.3	0.03	30°	$7.0e4$

Table 3.2: Predicted effective elastic properties of a honeycomb material.

	E_1	E_2	G_{12}	ν_{12}	ν_{21}	$\nu_{12} \cdot \nu_{21}$
Ashby&Gibson	0.161	0.161	0.0403	1.0	1.0	1.0
FIBNET #1	0.2466	0.2259	0.0398	1.0443	0.9565	0.99887
FIBNET #2	0.2448	0.2287	0.0547	1.0341	0.9659	0.99883
FIBNET #3	0.2382	0.2208	0.0506	1.0381	0.9622	0.99885

Chapter 4

Meso-/Macro-mechanics of Reinforced Porous Ceramic Composites

In fibrous composites, meso-scale refers to the intermediate geometric scale between the micro-level (fiber) and macro-level (coupon); for example, fiber tow is a typical mesoscopic entity. Many mechanics models are built upon the abstraction at the meso-scale, particularly models of textile composites. In the next section, a brief review of the modeling of textile composites is given.

4.1 Literature Review

In the past two decades, many researchers have developed models to predict mechanical properties of textile composites. Ishikawa and Chou [30, 31, 32] developed several techniques, e.g., the "mosaic" model and the "crimp" (fiber undulation) model, for modeling the effective stiffness of textile composites. In the "mosaic" model, a woven composite is regarded as an assemblage of pieces of asymmetric cross-ply laminates. The composite elastic constant is

then obtained by parallel and series models assuming iso-strain and iso-stress conditions. In the "crimp" (fiber undulation) model, the fiber undulation at tow cross-over point is taken into account. The undulation region is approximated by infinitesimal slices of the thread-wise strip. These two analytical models are applicable to 2D woven composites. The "mosaic" model is suited for fabrics with large n_g[1] values and the "crimp" model is suited for fabrics with low n_g values.

Shankar and Marrey [53] proposed a selective averaging method (SAM) for predicting the effective stiffness of textile composite beam and plate. The SAM method is based on unit cell analysis. The unit cell is divided into slices (meso-scale) and the slices are subdivided into elements (micro-scale). The elastic constants of the homogenized medium are obtained by averaging elastic constants of elements selectively for both iso-stress and iso-strain conditions. The predicted elastic constants by Shankar and Marrey matched well with finite element results.

Finite element analysis (FEA) has long been used to analyze the behavior of woven composites, especially those with identifiable unit cells. (See works of Ichihashi *et al* [29], Glaessgen *et al* [22], Whitcomb [71, 72], Woo and Whitcomb [74], Chapman and Whitcomb [8], Fujita *et al* [19], Dasgupta and Bhandarkar [15].) FEA predicted elastic constants have generally good agreements with experimental values. Whitcomb tried to simulate the failure behavior of woven composite by FEA. He found the results to be sensitive to the order of integration quadrature, mesh refinement, and material degradation model. Cox *et al* [13, 75] developed a finite element model, known as the "binary model", for simulating 3D woven textile composite with 3D interlock reinforcements in the elastic regime. In the binary model axial properties of tows are represented by two-noded line elements, while the transverse stiffness, shear stiffness, and Poisson's effect of the composite are represented by solid elements—the "effective medium". This effective medium is assumed to be homogeneous.

[1]For plain weave, $n_g = 2$; for eight-harness satin weave, $n_g = 8$.

Above reviewed works have targeted woven fibrous composites with polymer matrix. The reviewed models can be roughly classified into two types: analytical models and numerical models. The analytical model usually requires assumptions such as iso-stress, iso-strain, or a mixture of iso-stress and iso-strain (e.g., SAM). The numerical model generally relies on the finite element analysis. For the purpose of predicting effective elastic moduli, these methodologies can be applied to ceramic composites as well.

4.2 Fiber Reinforced Porous Ceramic Composites

Porous ceramic materials are significantly weaker than the corresponding materials in the dense-forms. Reinforcements are sometimes needed in these materials to increase their load-bearing capabilities. Typical reinforcements are continuous ceramic fibers or fiber tows. There exist many processing techniques in manufacturing fiber reinforced ceramic composites, such as filament winding, braiding, weaving, etc., followed by a chemical vapor infiltration or a sol-gel infiltration before firing. Two types of fibers are commonly used as reinforcements: (i) alumina-based fibers such as Nextel-610 and Nextel-720 (ii) SiC-based fibers such as Nicalon and Hi-Nicalon. These fibers have elastic modulus in the range of 200 to 400 GPa and nominal strength in the range of 2 to 3 GPa. Both of these properties are several order of magnitudes higher then the corresponding values of typical porous ceramic materials.

Reinforcing fibers have been incorporated into dense ceramic matrix to form dense continuous fiber reinforced ceramic composites (CFCC), in which reinforcing fibers and dense matrix have comparable stiffness and strength. For the dense systems, the primary purpose of "reinforcing" fibers is to increase energy dissipation in their failure processes. That is achieved by the frictional loss in a so-called "fiber pullout" process and weak bonding between the fiber and the matrix is a pre-requisite to induce fiber pullout. For a porous system, the introduc-

tion of high stiffness and high strength reinforcing fibers significantly boosts all mechanical properties of the porous matrix material, including stiffness, strength, and toughness. In the porous composite system, the bonding strength between fiber and reinforcements is usually weak; it is no stronger than the strength of the weak porous matrix. In their failure process, fiber-matrix debonding is almost ensured and is followed by tow bridging across the failed matrix materials, and later fibers plowing through and pulling out of the crushing matrix. More energy is dissipated in these processes and improved toughness can be achieved.

In designing fiber reinforced porous material systems, questions, such as how to arrange the reinforcements to achieve the maximum reinforcing effect on stiffness and strength, need to be answered. One central problem is how the mechanical properties of the composites material system is related to properties and geometric arrangement of reinforcing fiber tows. The subjects of interest in this case are the fiber tow and the matrix, the analysis can be simplified by assuming that the fiber tows are unidirectional composites and the matrix is a homogeneous orthotropic material. The smallest length in this abstraction is the diameter of fiber tows, which is typically sub-millimeter, hence the modeling is classified meso/macro-mechanics. This problem has been addressed in following sections. As an concrete example, the MTI ceramic composite candle filter material is analyzed. A picture of the MTI candle filter material at the mesoscopic scale is shown in Figure 4.1 (compared with a picture in the microscopic scale shown in Figure 4.2). At the meso-scale, the author identified the fiber tow and chopped fiber matrix as two distinct components. Two analysis schemes were developed for the MTI composite material system the model predicted results were compared with experimental data reported in Chapter 2.

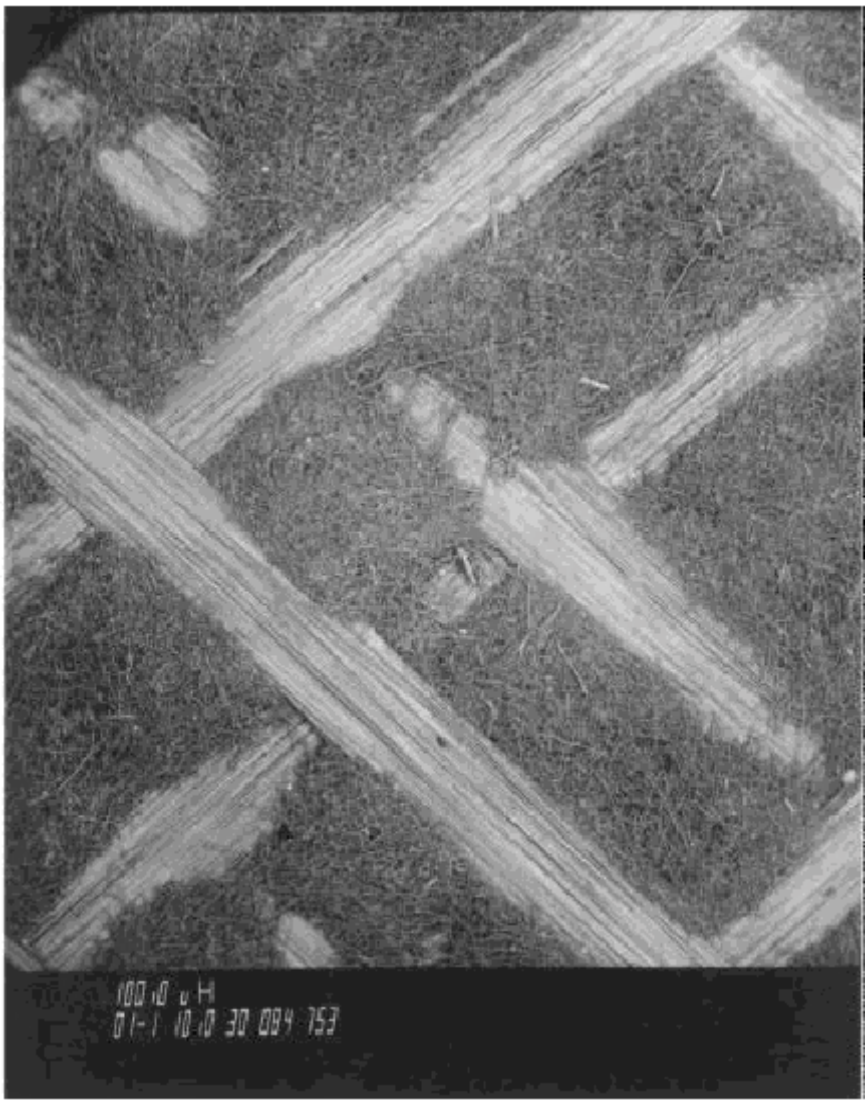

Figure 4.1: Micro-graph of the MTI filament-wound candle filter tube. Light strips are Nextel-610 fiber tows; dark areas are the chopped Saffil fiber matrix. (Photo courtesy of MTI Lynchburg research center, composite section, Lynchburg, VA)

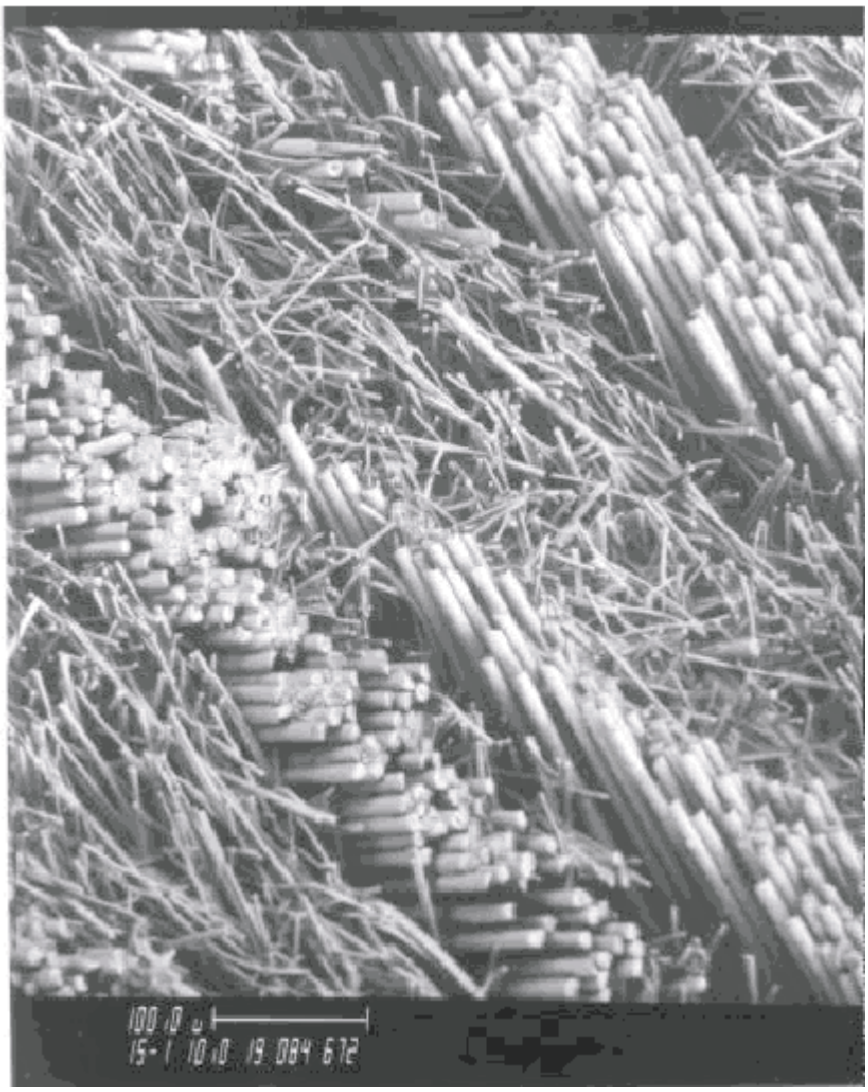

Figure 4.2: SEM picture of a crossi-section of a MTI composite candle filter. Nextel-610 fiber bundle and randomly oriented Saffil chopped fibers are clearly shown in the picture. (Photo courtesy of MTI Lynchburg research center, composite section, Lynchburg, VA)

4.3 Analytical Scheme — Energy Method

The author has developed a meso-level analytical scheme to predict the tensile and torsional stiffness of the MTI candle filter tube. The method is based on the well-known principle of stationary potential energy and is thus called the "energy method." The method is built upon the the kinematic assumptions shown in Figure 4.3. The MTI candle filter is a filament wound tube. If we cut the tube open along one of its generating lines and unwrap it into a flat surface, the matrix material and fiber tow can then represented by a parallelogram and its diagonals as shown in Figure 4.3. The deformed shape is shown in dashed lines. This idealized deformation can be characterized by a few parameters (generalized coordinates), for example, γ, Δh, and Δw. The elongation of fiber tow and shearing/stretching of the matrix can all be expressed as functions of these generalized coordinates.

Upon deformation, strain energy is stored in the filter material system. The total potential energy of the filter tube can be expressed in terms of these generalized coordinates. According to the theorem of stationary potential energy, at equilibrium, the total potential energy has a local minimum value [36], which implies that the derivatives of total potential energy with respect to the chosen generalized coordinates must vanish at the equilibrium point. A system of algebraic equations can be generated. By solving these equations, closed-form predictive equations can be derived. Using this approach, the author obtained the closed-form equations that relate tube global tensile and torsional stiffness and Poisson's ratio to the constituent properties and several processing variables, such as fiber tow winding angle, fiber tow spacing, etc. The details of the derivation are presented in following two sections.

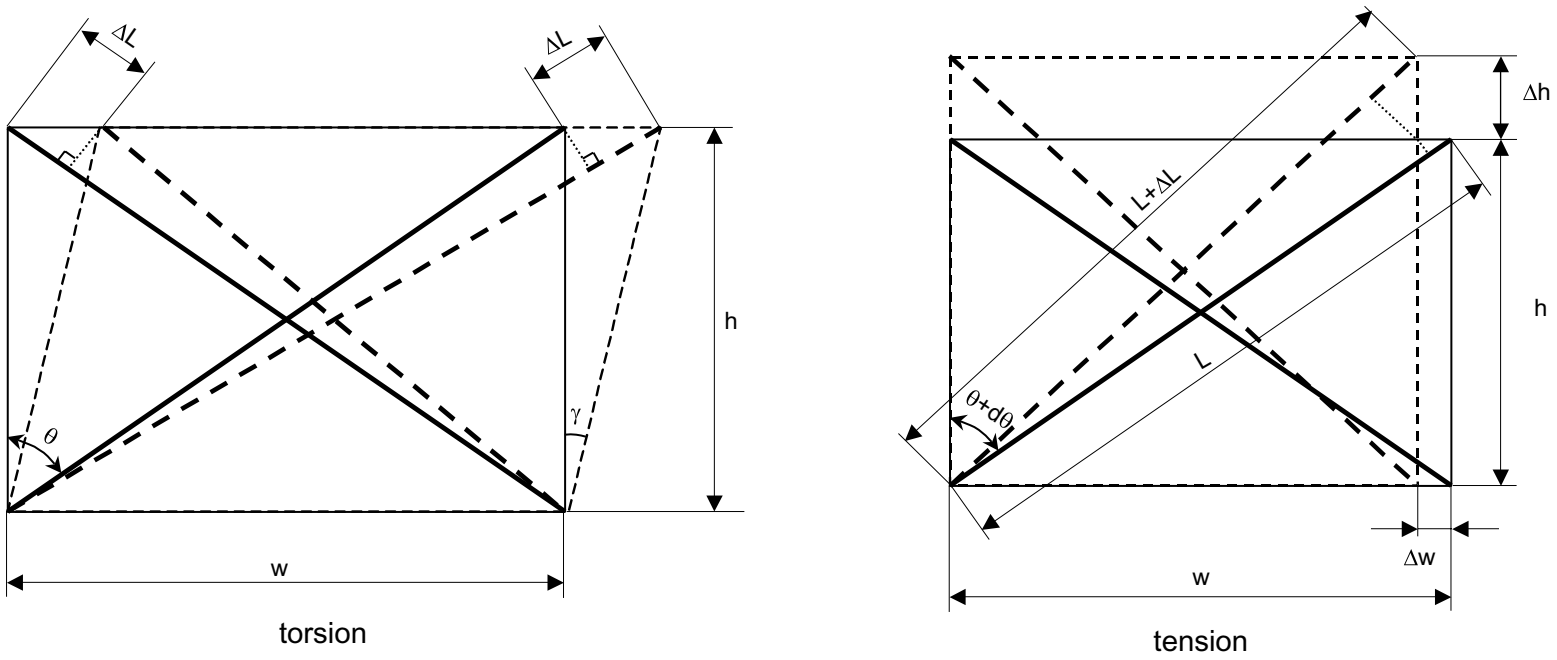

Figure 4.3: Kinematics assumptions used in the energy method

4.3.1 Tube Tension

Tube tensile stiffness and global Poisson's ratio can be estimated by using the energy method. Assume a thin walled filter tube segment with height h and winding angle θ is put in tension by an axial force P. It causes the tube to extend axially by a small length e, and to contract radially. Assume the global Poisson's ratio is $\widetilde{\nu}$. Assume the length of a fiber tow is L, and the Young's modulus and cross section area of a fiber tow are E_t and A_t respectively. The deformation (configuration) of the tube under loading can be determined approximately by e and $\widetilde{\nu}$. Strain energy is stored in both fiber tow (U_t) and chopped fiber matrix (U_m). The work done by the external force is denoted by $-\Omega$. Thus, the total potential energy of the system (V) is:

$$V = U_t(e, \widetilde{\nu}) + U_m(e, \widetilde{\nu}) + \Omega(e) \tag{4.1}$$

According to the principle of stationary potential energy (see [36] Chapter 1), at an equilibrium point in the configuration space, the total potential energy corresponds is a local minimum. So, at equilibrium:

$$\frac{\partial V}{\partial e} = \frac{\partial U_t(e, \widetilde{\nu})}{\partial e} + \frac{\partial U_m(e, \widetilde{\nu})}{\partial e} + \frac{d\Omega(e)}{de} = 0 \tag{4.2}$$

$$\frac{\partial V}{\partial \widetilde{\nu}} = \frac{\partial U_t(e, \widetilde{\nu})}{\partial \widetilde{\nu}} + \frac{\partial U_m(e, \widetilde{\nu})}{\partial \widetilde{\nu}} = 0 \tag{4.3}$$

The elongation of a fiber tow ΔL can be expressed in terms of tube elongation e, fiber tow winding angle θ, and global Poisson's ratio $\widetilde{\nu}$.

$$\Delta L = e\cos\theta - \widetilde{\nu} e \tan\theta \sin\theta \tag{4.4}$$

Assume that the total number of tows in this tube segment is n_t. The total strain energy

stored in fiber tows can then be expressed as:

$$U_t = \frac{n_t E_t A_t e^2}{2L} \left(\cos\theta - \widetilde{\nu} \tan\theta \sin\theta\right)^2 \tag{4.5}$$

Assume the chopped matrix is in a state of plane stress and it has a axial strain $\epsilon_x = \frac{e}{h}$ and a hoop strain $\epsilon_y = -\widetilde{\nu}\epsilon_x$. Then the strain energy stored in the chopped fiber matrix can be expressed as([62]):

$$\begin{aligned} U_m &= \frac{B_m E_m}{2\left(1-\nu_m^2\right)} \left(\epsilon_x^2 + \epsilon_y^2 + 2\nu_m \epsilon_x \epsilon_y\right) && (4.6) \\ &= \frac{B_m E_m e^2}{2h^2\left(1-\nu_m^2\right)} \left(1 + \widetilde{\nu}^2 - 2\nu_m \widetilde{\nu}\right) && (4.7) \end{aligned}$$

in which, B_m is the total volume of chopped fiber matrix, E_m and ν_m are Young's modulus and Poisson's ratio of chopped fiber matrix respectively. Substituting the work done by the external force $-\Omega = Pe$ and U_t and U_m into the total potential energy expression yields,

$$V = \frac{n_t E_t A_t e^2}{2L} \left(\cos\theta - \widetilde{\nu} \tan\theta \sin\theta\right)^2 + \frac{B_m E_m e^2}{2\left(1-\nu_m^2\right) h^2} \left(1 + \widetilde{\nu}^2 - 2\nu_m \widetilde{\nu}\right) - Pe \tag{4.8}$$

in which, $B_m = f_m A h$, $n_t A_t = \frac{f_t A h}{L}$, f_t and f_m are volume fractions of continuous fiber tow and chopped fiber matrix respectively. A is the cross section area of tube segment. Take the derivative of V with respect to e and $\widetilde{\nu}$, consider that $\widetilde{E} = \frac{PL}{Ae}$, and solve for $\widetilde{\nu}$ and $\widetilde{E}$, following results can be obtained.

$$\begin{aligned} \widetilde{\nu} &= \frac{f_t E_t \left(1-\nu_m^2\right) \sin^2\theta \cos^2\theta + f_m E_m \nu_m}{f_t E_t \left(1-\nu_m^2\right) \sin^4\theta + f_m E_m} && (4.9) \\ \widetilde{E} &= f_t E_t \cos^2\theta \left(\cos\theta - \widetilde{\nu} \tan\theta \sin\theta\right)^2 + f_m E_m \frac{1 + \widetilde{\nu} - 2\widetilde{\nu}\nu_m}{1-\nu_m^2} && (4.10) \end{aligned}$$

Define parameters C_t and C_m as following:

$$C_t = f_t \cos^2\theta \left(\cos\theta - \widetilde{\nu}\tan\theta\sin\theta\right)^2 \tag{4.11}$$

$$C_m = \frac{1+\widetilde{\nu}-2\widetilde{\nu}\nu_m}{1-\nu_m^2} f_m \tag{4.12}$$

then,

$$\widetilde{E} = C_t E_t + C_m E_m \tag{4.13}$$

For the case $f_t = 0$ or $E_t = 0$, we have $\widetilde{\nu} = \nu_m$ and $\widetilde{E} = E_m$ from Equation 4.10. For the case $\theta = 45^\circ$ and $E_t >> E_m$, we get $\widetilde{\nu} \doteq \cot\theta = 1.0$ and $C_t = 0$; thus

$$\widetilde{E} = C_m E_m = \frac{2f_m}{1+\nu_m} E_m \tag{4.14}$$

when $f_m \doteq 1.0$ and $\nu_m \doteq 0.5$ (rubber), it gives $\widetilde{E} = \frac{4}{3}E_m$, which is a widely known result for cord reinforced rubber composites [2].

For the MTI filter tube, $f_t \doteq 8\%$, $f_m \doteq 92\%$, $45^\circ < \theta < 50^\circ$, $E_t \doteq 372\ GPa$ (54.0 $Mpsi$). The exact value of ν_m and E_m are not known, $\widetilde{E}$ and $\widetilde{\nu}$ are plotted as functions of E_m and ν_m instead. For $\theta = 45^\circ$, the results are shown in Figure 4.4 and 4.6. For $\theta = 50^\circ$, the results are shown in Figure 4.5 and 4.7. According to the experimental results, $\widetilde{E}$ is in the range 3.5–4.0 GPa. In the following plots, we can see that E_m should be in the range of 2–3 GPa. And $\widetilde{\nu}$ should be around 0.7–1.0 according to Figure 4.6 and 4.7.

To find out which is the dominant part on the right side of Equation 4.13, $\frac{C_t E_t}{C_m E_m}$ is plotted as a function of E_m and ν_m. It was found that, in the reasonable range of E_m and ν_m, the contribution from continuous fiber tow to tube global tensile stiffness is negligible compared to that of the chopped fiber matrix. For the present configuration of materials in the tube, this result indicates that in the tube tension test, the tensile stiffness observed is predominantly

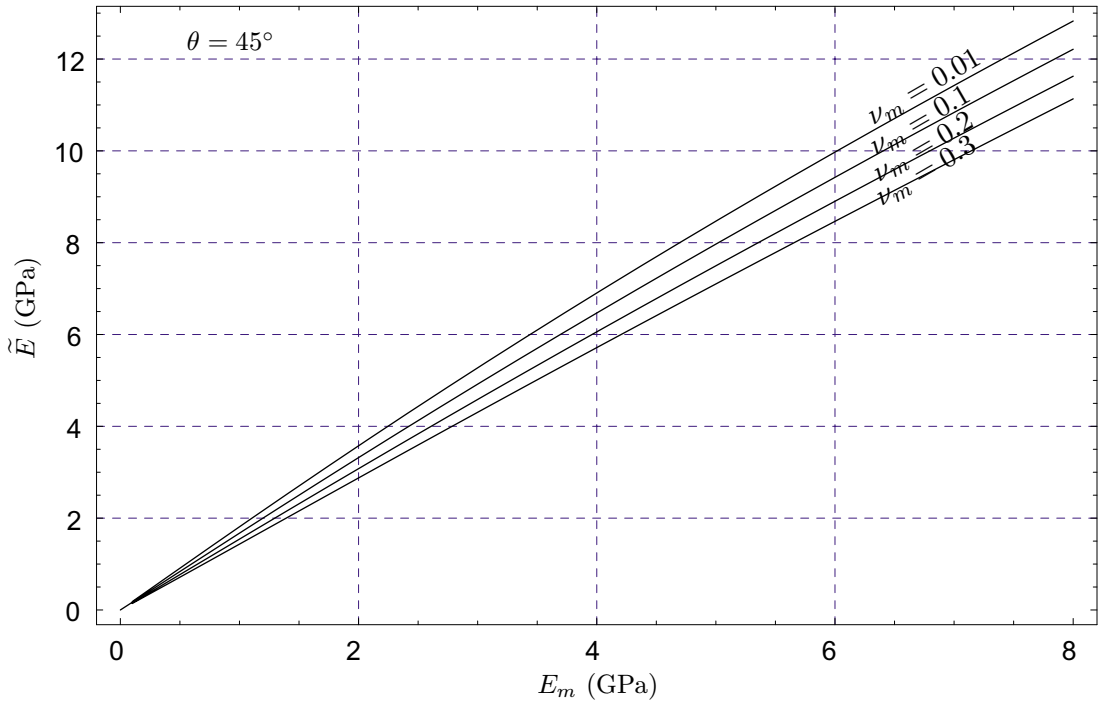

Figure 4.4: Plot of $\widetilde{E}$ as a function of E_m and ν_m.

the tensile stiffness of the chopped fiber matrix.

4.3.2 Tube Torsion

The global torsional stiffness of the filter tube can be estimated by using a simple energy method. If assume that the strain energy (internal energy) of filter tube is primarily stored in continuous fiber tows if it is loaded in torsion, then the torsional stiffness can be expressed in terms of fiber tow stiffness k_t, fiber winding angle θ, fiber tow count n_t[2], and the cross-section area of filter tube A:

[2]equals to the number of fiber tows that are cut off in a tube cross-section perpendicular to tube axis

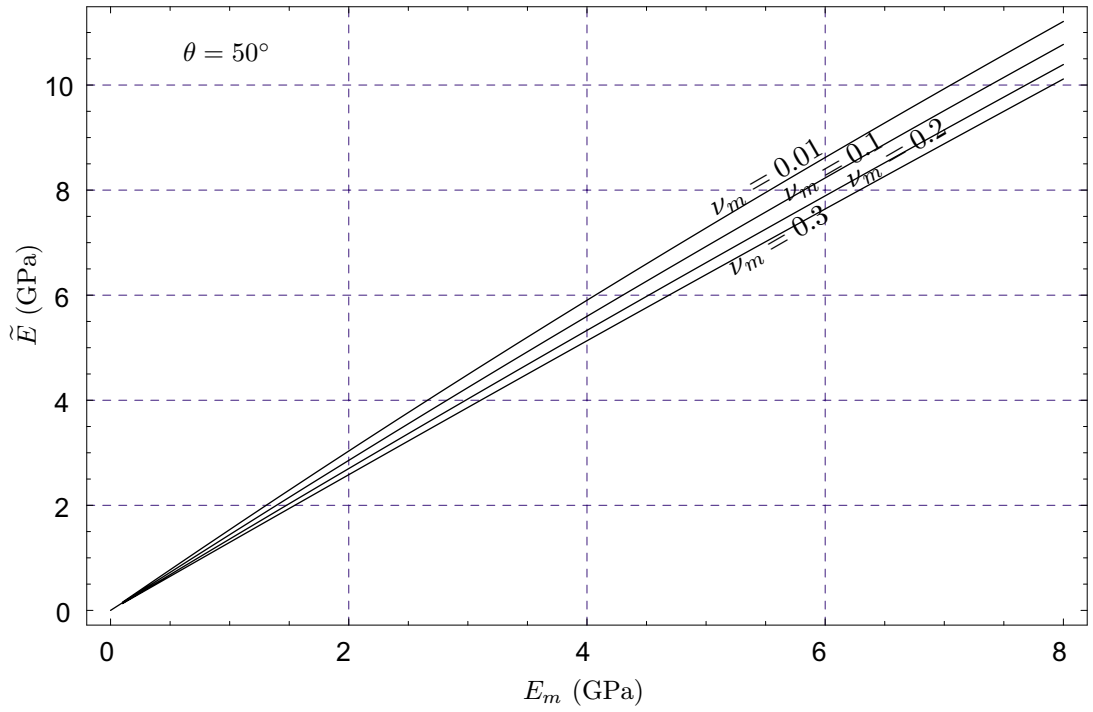

Figure 4.5: Plot of $\widetilde{E}$ as a function of E_m and ν_m.

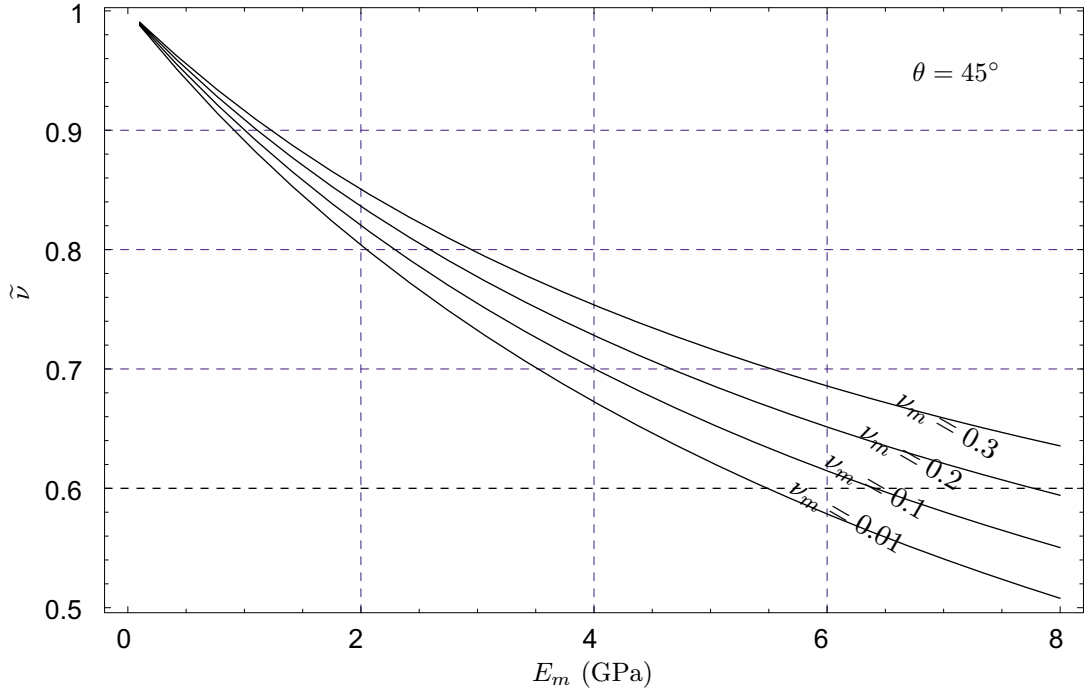

Figure 4.6: Plot of $\widetilde{\nu}$ as a function of E_m and ν_m.

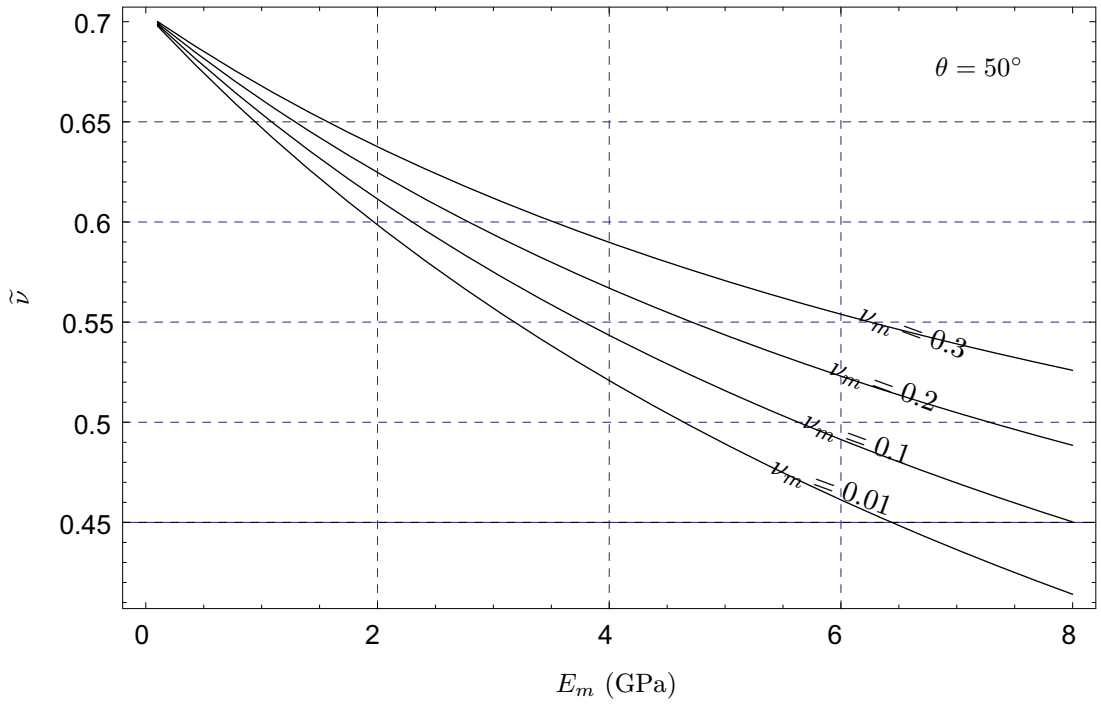

Figure 4.7: Plot of $\widetilde{\nu}$ as a function of E_m and ν_m.

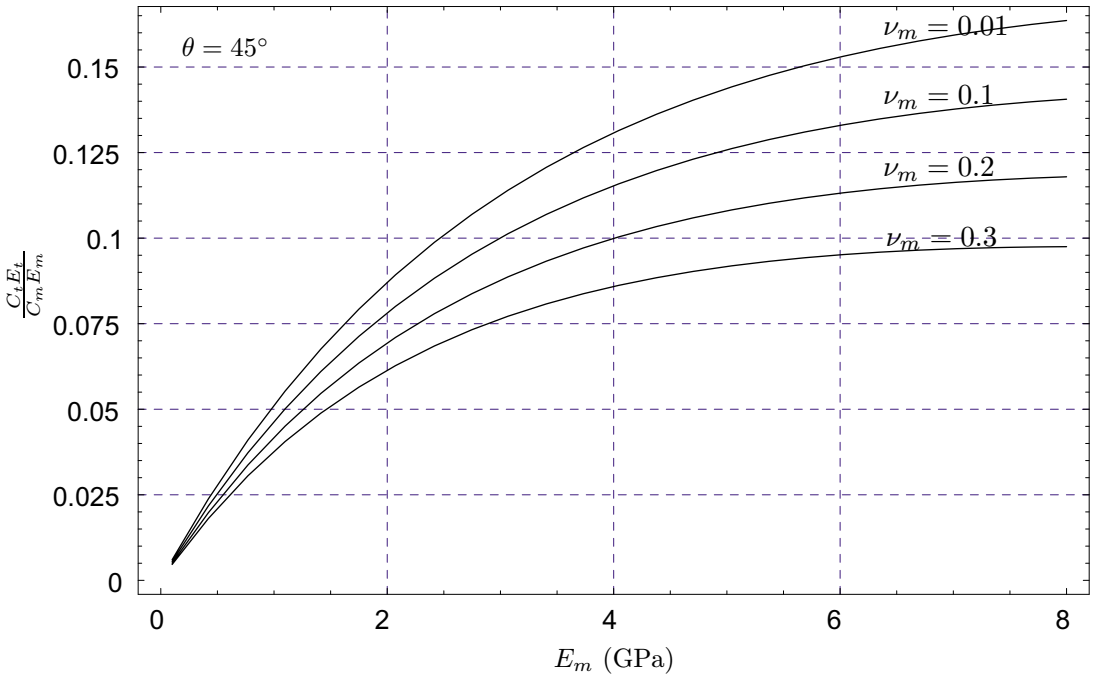

Figure 4.8: Plot of $\frac{C_t E_t}{C_m E_m}$ as a function of E_m and ν_m.

$$\widetilde{G} \doteq n_t \frac{k_t}{A} \sin^2\theta \cos\theta \tag{4.15}$$

$$= f_t E_t \sin^2\theta \cos^2\theta \tag{4.16}$$

in which,

$$k_t = E_t A_t$$

E_t is the Young's modulus of fiber tow and A_t is cross-section area of fiber tow.

For the MTI filter tubes that have been tested, $n_t \doteq 1024$, $E_t \doteq 54\ mpsi$, $f_t \doteq 0.08$. The predicted and experimental result is shown in Table 4.1

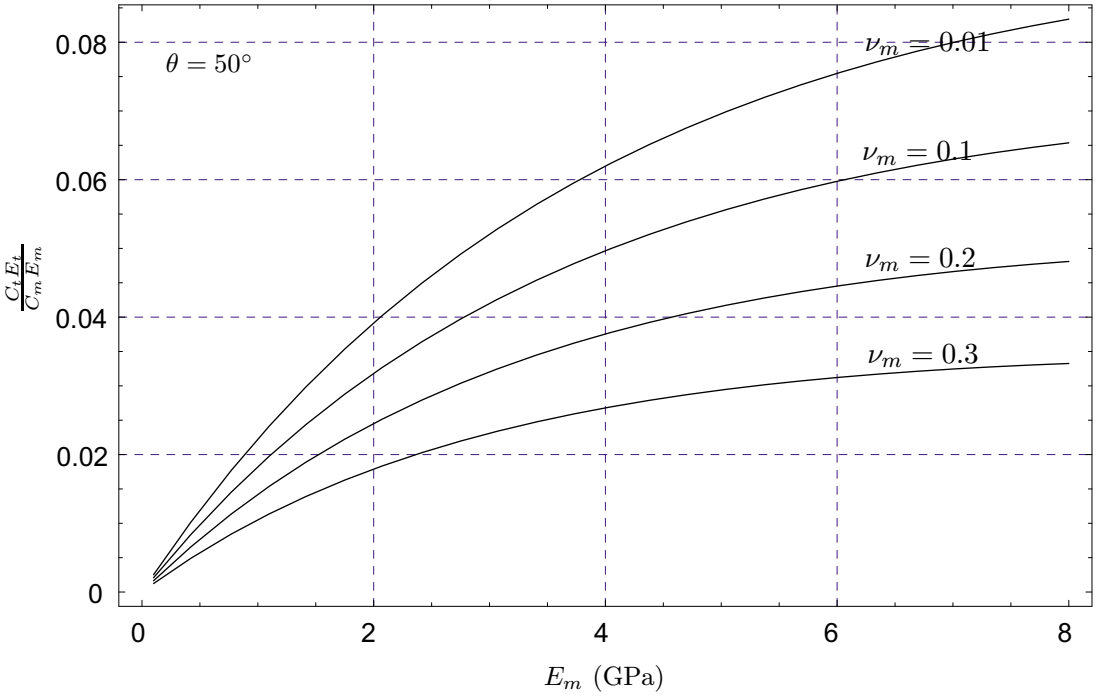

Figure 4.9: Plot of $\frac{C_t E_t}{C_m E_m}$ as a function of E_m and ν_m.

Table 4.1: Predicted and measured torsional stiffness of MTI candle filter tubes.

Model	Expr. Avg	Expr. Std.
7.24 GPa	7.63 GPa	0.36 GPa

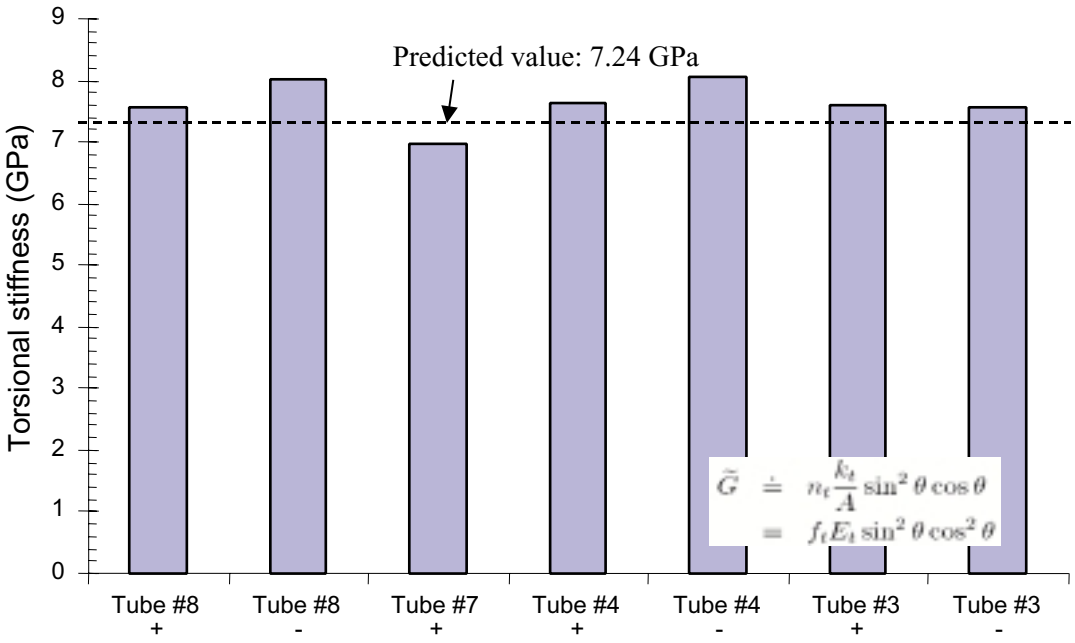

Figure 4.10: Comparison of predicted and observed torsional stiffness

4.4 Numerical Method — Ligature Model

The analytical scheme described in the previous section is limited to regular shaped components under simple loading conditions. To model the mechanical response of components with complex geometry and under realistic loading conditions, numerical methods such as finite element procedures are required.

Inspired by the "binary model" of Cox *et al* [13, 75], the author constructed a so-called "ligature" model. The ligature model is a finite element scheme to model fiber reinforced composites and it is suited to deal with composites with following characteristics: (1) the one-dimensional reinforcing elements have large spacings and occupy a small volume fraction (2) there is large difference between the stiffness of the reinforcements and the matrix. Because of the large spacing of the reinforcing fibers, they can be modeled discretely without resulting in an huge model. Compared to smearing the fiber stiffness into the matrix, it is more

direct and natural to model the reinforcements and matrix with different material properties especially when their stiffness differs by several orders of magnitude.

The ligature elements can be represented by truss, frame, or rebar elements, which are implemented in most FEM software packages. The effect of the soft matrix is represented by solid elements, which is comparable to the effective media in the "binary model". The orientation and spacial distribution of the ligature elements are set in accordance with the actual path of the reinforcing fiber tows.

The solid element and ligature element need to couple together, and there are two ways to implement the coupling: (1) by sharing the common nodes (2) by integrating the stiffness contribution of ligature element directly into the solid element stiffness matrix (rebar). Using the first method, truss elements can be superimposed onto solid elements and frame elements can be superimposed onto shell elements by shearing a set of common nodes. Because the ligature element needs to follow the actual direction of reinforcing fibers, the mesh for the solid/shell elements needs to be specially designed to accommodate the superimposed ligature element. In the second method, the stiffness contribution of reinforcing element is directly incorporated into the element stiffness matrix of the underlying solid element and node-sharing is not necessary. This scheme is usually implemented as "rebar" features in FEM software packages. Equation 4.17 shows the adjusted Gauss integration volume to incorporate the rebar stiffness in Abaqus [26]:

$$\Delta V = \frac{A_r}{A_s} \left(\frac{\partial x}{\partial r} \cdot \frac{\partial x}{\partial r} \right)^{\frac{1}{2}} t_0 W_N \tag{4.17}$$

in which, t_0 is the original thickness for plane elements and A_r is the rebar cross-sectional area, S_r is the spacing of rebar, W_N is the Gauss weight of the integration point, r is the coordinate attached to the axis of the rebar and $x = x(g_i)$ is the position vector in the underlying solid element. The strain in the rebar is calculated by projecting the deformation

of the underlying solid element onto the arbitrary direction defined by a rebar element. In Abaqus, the logarithmic strain in the rebar is calculated by the following equation:

$$\epsilon = \frac{1}{2} \ln \left(\frac{dl^2}{dl_0^2} \right) \tag{4.18}$$

where, dl and dl_0 measure the length along the rebar in the current and initial configuration. The rebar approach is equivalent to the smeared approach except that the rebar force is explicitly resolved at the end of analysis. The node-sharing approach will cause artificial stress concentrations at nodes that are shared and the rebar approach does not has such a problem. In summary, the ligature model has following features:

- FEM based modeling technique.
- Use truss/frame/rebar to model reinforcements explicitly.
- Use 2D/3D continuum element to model matrix material.
- Reveal global stiffness as a function of meso-level geometry and material details.
- Reveal force resultant in fiber tows.
- Reveal average stress level in the matrix

4.4.1 Verification and Comparison

In this section, two ligature model examples of the MTI candle filter material are presented and compared with other analysis methods. The elastic properties of the fiber tow are determined by the rule of mixtures, assuming the fiber tow to be a unidirectional composite. Properties of the chopped fiber matrix are estimated from experimental data.

Table 4.2: Predicted and measured tensile stiffness of MTI candle fiber tubes.

	E (GPa)	ν
Experiment	3.57	0.4–1.2
Model	3.82	.97

ligature model: block

To test and validate the ligature model, the author constructed a model of a flat panel. This model consists of 576 solid elements of type C3D8[3] and 640 truss element of type T3D2[4]. The block was anchored at the bottom with symmetric boundary conditions, while loads was applied on top in the form of specified displacements. To calculate global stiffness, the resultant nodal force was summed up on the top surface and used to calculate global stress. The displacements of two lateral sides were used to calculate the global Poisson's ratio. The model was constructed and solved with ABAQUS version 5.7 and calculated results and experimental values are shown in Table 4.2.

ligature model: one-inch ring under tension & torsion

Another example is a model of an 1-in long tube segment. In this case, the fiber tows (ligatures) follow a curved path in accordance with the fiber winding angle. Using the same material properties and element types as in the Block model, the ring model can predict tube tension/torsion stiffness. The predicted results are compared with those predicted by the energy method.

Figure 4.11 and 4.12 show the comparison of tube tensile stiffness predicted by both the

[3]linear 8-node 3-D solid element in ABAQUS solid element library

[4]2-node linear link element

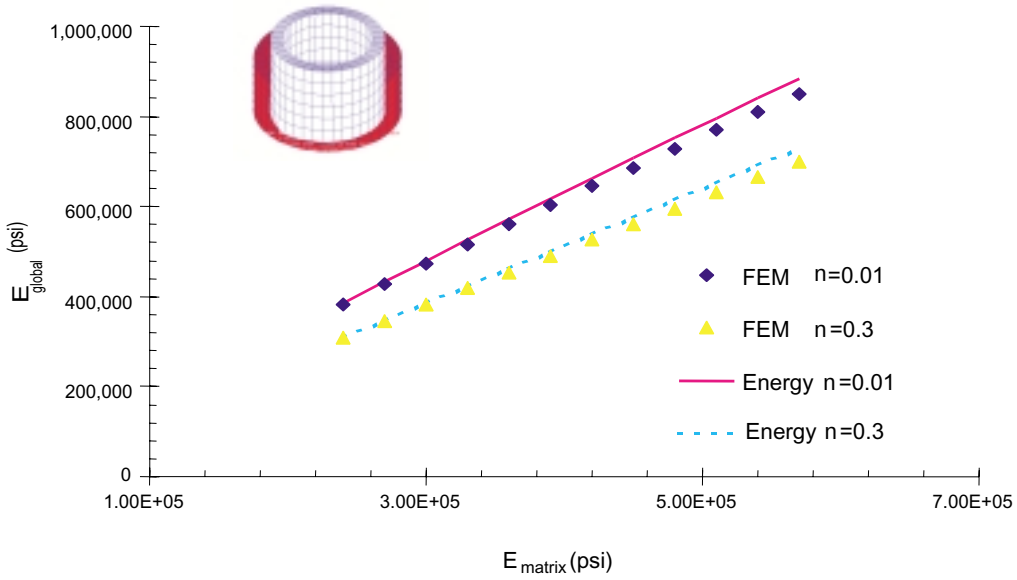

Figure 4.11: Comparison of stiffness predicted by the energy method and the ligature model: E_g v.s. E_m

ligature model and the energy method. The stiffness of chopped fiber matrix and winding angle of the fiber tow are varied and predictions from two methods are shown to be fairly close. Figure 4.13 shows the tube torsional stiffness predicted by the two method at a number of winding angles. The ligature model gave a higher prediction than the energy method, but both predictions lie within the range of experimental data observed.

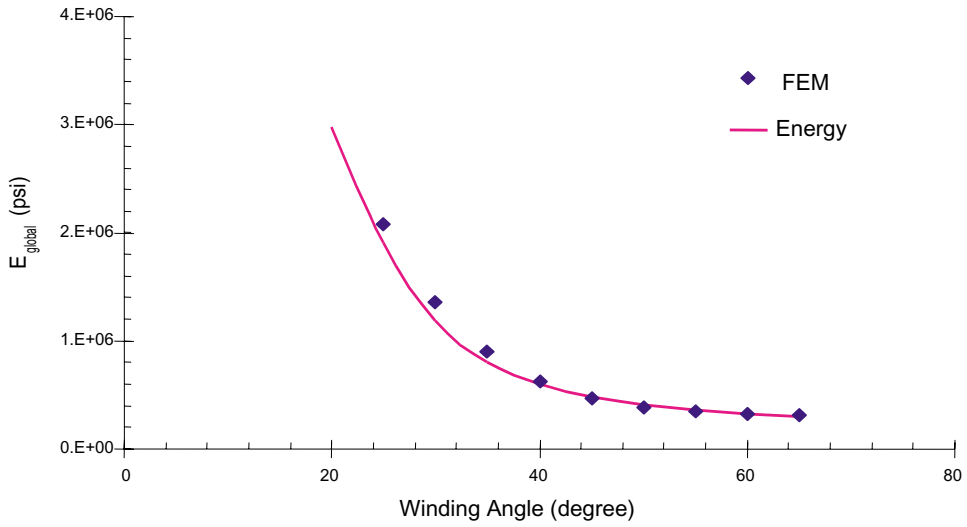

Figure 4.12: Comparison of stiffness predicted by the energy method and the ligature model: E_g v.s. winding angle

4.4.2 Stress Analysis Case Study

tube flange under compression

In a barrier filter system, filters are typically arranged in several modules. In each module, an array of candle filters are clamped onto a tube sheet by collars and bolts. Figure 4.14 shows an assembly of a filter tube flange with a collar and the tube sheet. To minimize stress concentration, the curved surface of the metal collar matches that of flange. Bolts exert a clamping force on the collar to seal the contact surface. The magnitude of the clamping force needs to be large enough to maintain a good seal without damaging the filter flange. Due to high clamping force, stresses in the flange region are higher than those in the rest part of candle filter tube. A ligature model of tube flange was built to analyze the stress distribution in the tube flange under such loading conditions and to demonstrate the flexibility of the ligature model in dealing with complex geometry.

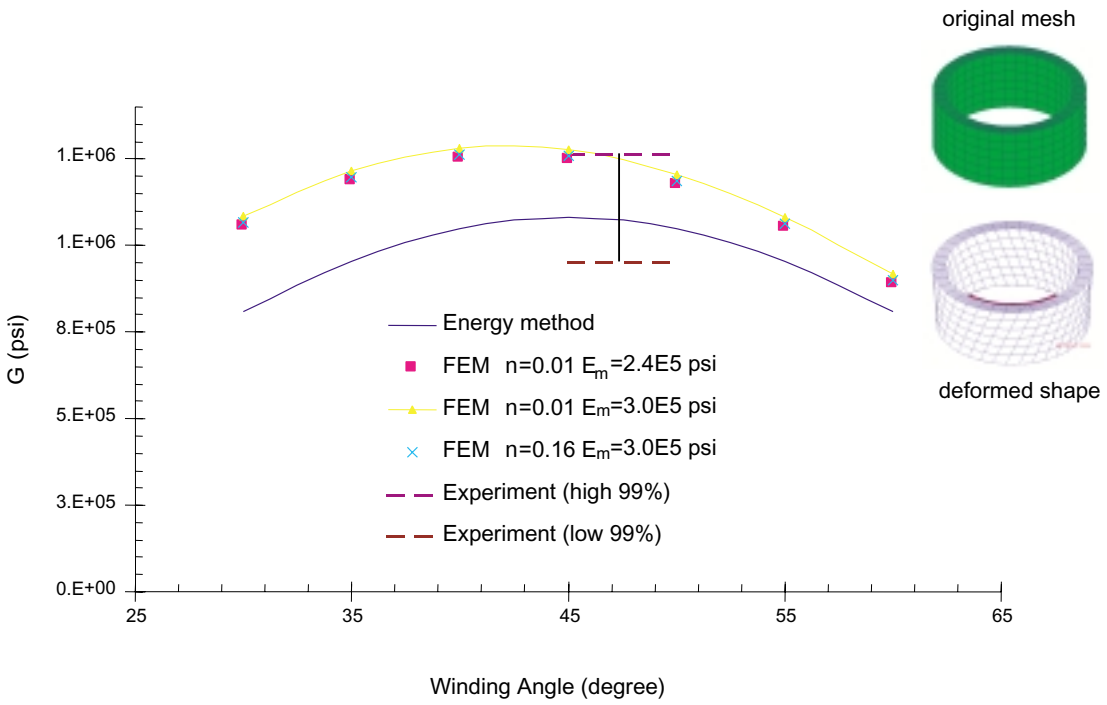

Figure 4.13: Comparison of stiffness predicted by the energy method and the ligature model: G v.s. winding angle

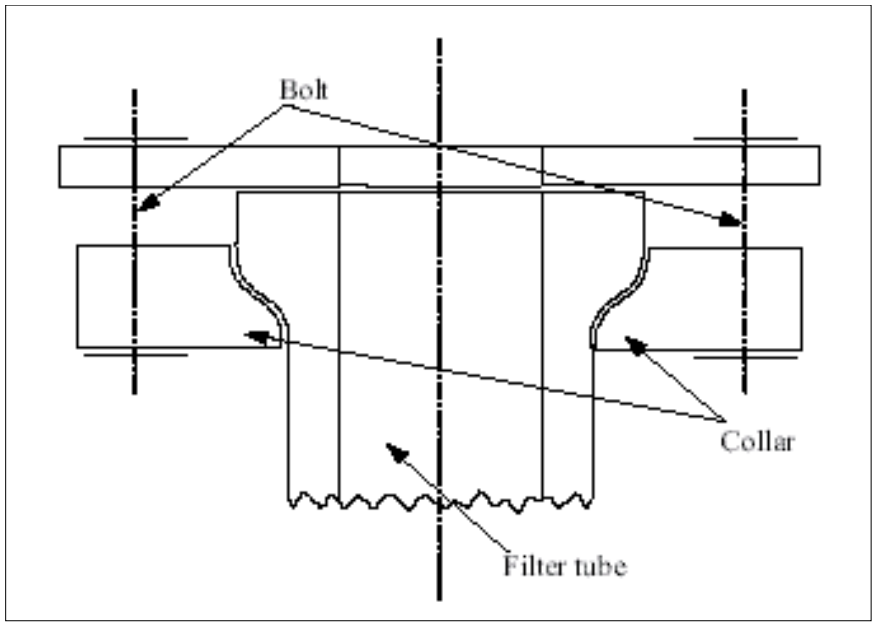

Figure 4.14: Schematic of the candle filter flange assembly.

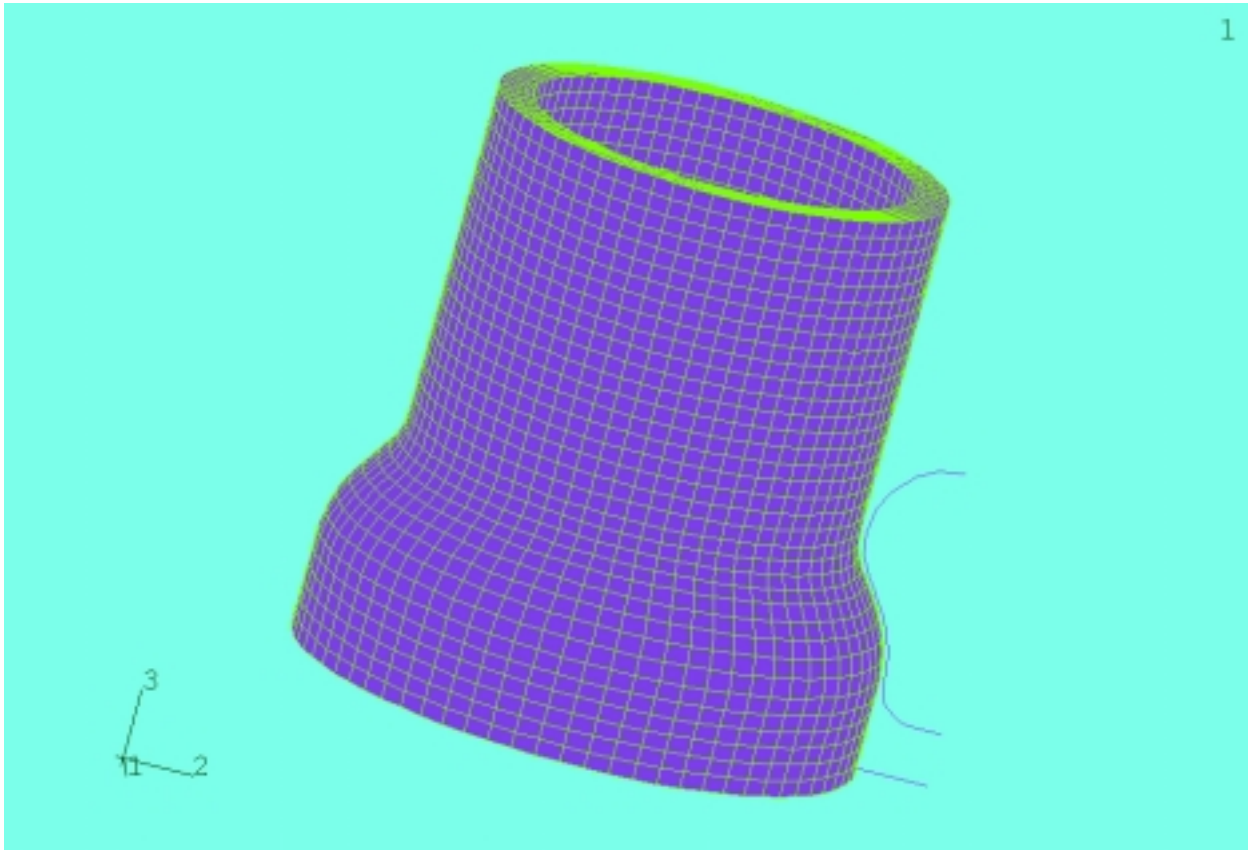

Figure 4.15: Finite element model of a candle filter flange.

The mesh for the flange model is shown in Figure 4.15. The fiber tow in the flange region follows geodesic path on the curved surface. It is necessary to model the exact direction of fiber tows in order to get an accurate representation of the reinforcements. A C++ code was implemented to calculate the geodesic direction of the fiber tows in the flange region and is attached in Appendix C. Twenty-noded iso-parametric block elements were used to model the chopped fiber matrix and 3D rebar elements that follow the path of fiber tows were used to simulate the fiber tow. Contact is a primary feature of this assembly, as shown in Figure 4.14. Due to the complicated interaction on the contact surfaces, contact elements were used to capture the interactions between those mating surfaces. Otherwise, it would be difficult to specify the boundary conditions on those surfaces. Two contact pairs were identified: one lies between the tube sheet and bottom surface of the filter tube, the other between the collar and the shoulder of the tube flange. The tube sheet and stainless steel collar were assumed to be rigid. Load was applied through the specification of the bolt force. The model was solved by ABAQUS with a general non-linear analysis procedure.

The deformed shape is shown in Figure 4.16 and the contour plot of the out-of-plane shear stress (σ_{23}) is shown in Figure 4.17. High shear stresses region were found near the shoulder of the flange as well as on the bottom surface that contacts the tube sheet. Compression tests were performed to assess the compression force that flange can sustain in this arrangement. And two failure regions were observed in the test: one was circular crack on the bottom surface of the flange (see Figure 4.18) and the other was the torn surface layer near the shoulder of the flange (see Figure 4.19). The stress results qualitatively agree with failure modes observed in the actual flange compression test.

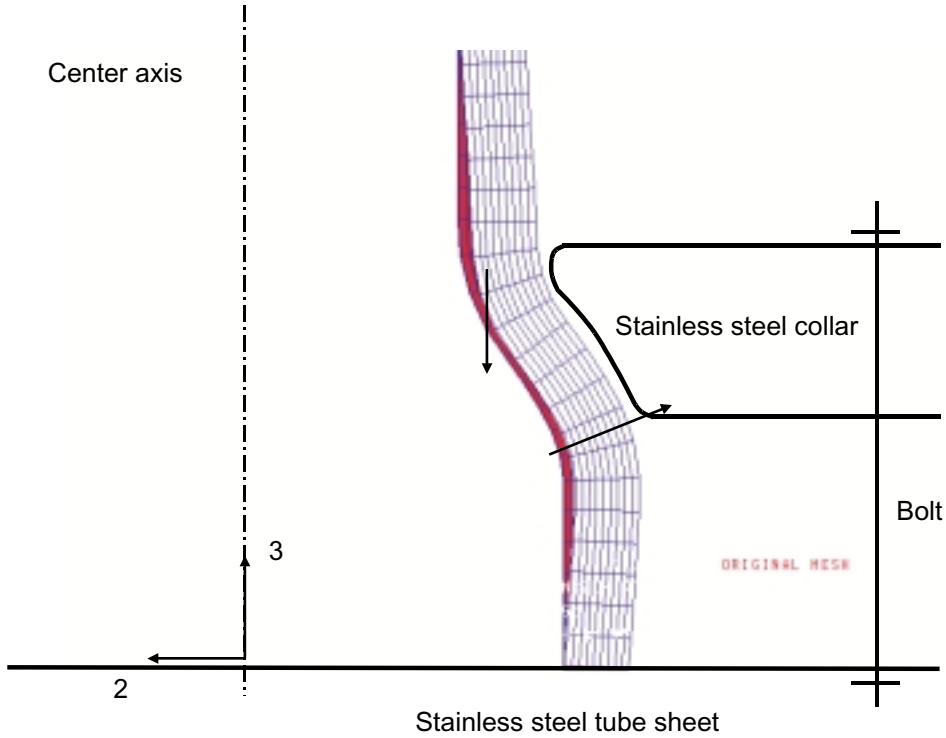

Figure 4.16: Simulated deformation of a flange under compression.

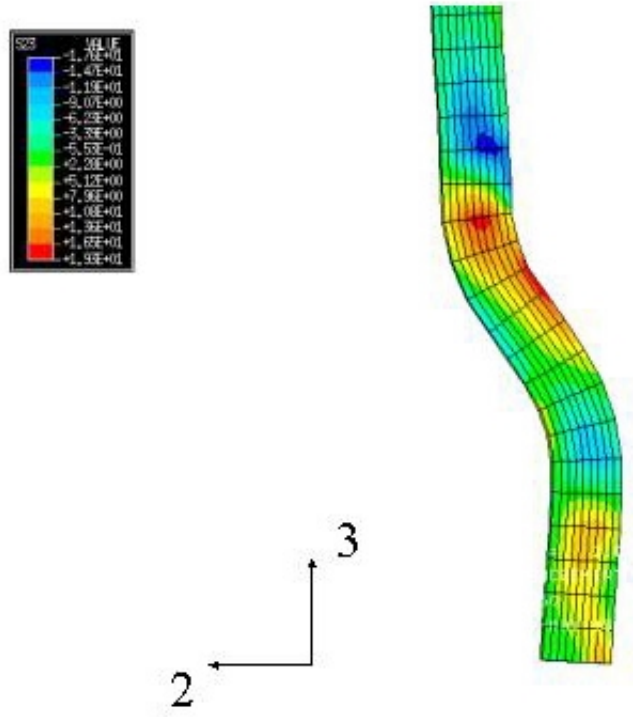

Figure 4.17: Contour plot of shear stress (σ_{23}) in the tube flange.

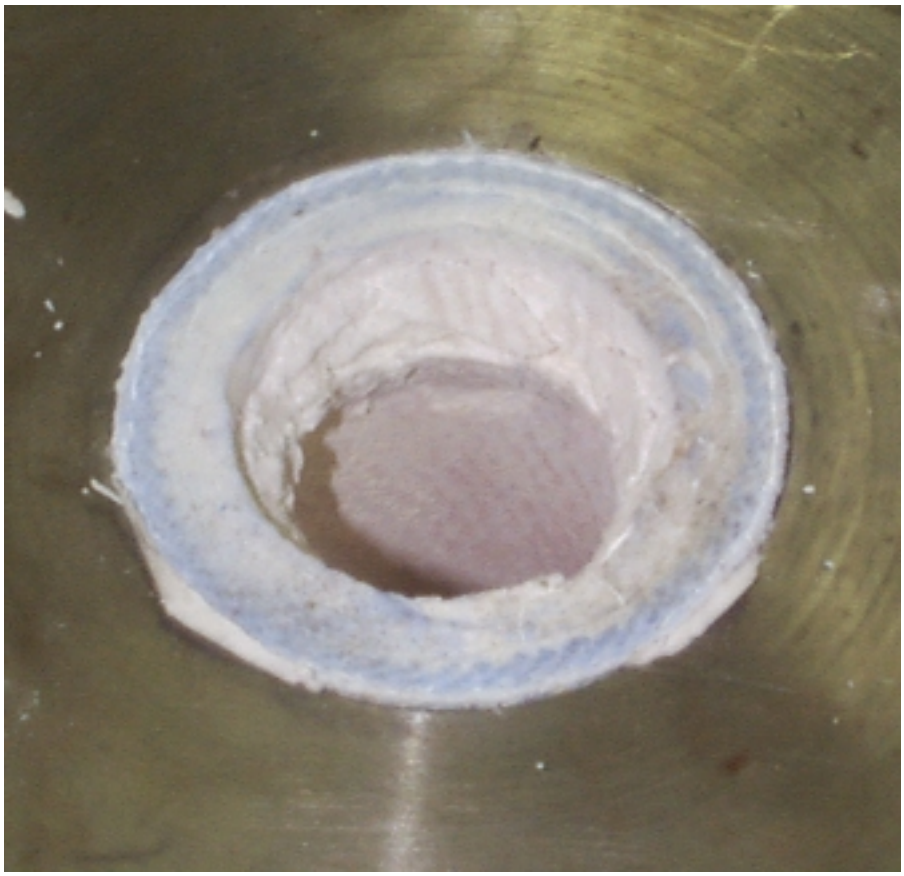

Figure 4.18: Failure mode of flange in a compression test: *circular cracks*

Figure 4.19: Failure mode of flange in a compression test: *torn surface layer*

Chapter 5

Strength and Durability

In the first part of this chapter, the failure behavior of the MTI ceramic composite candle filter material is discussed; in the second part, the degradation mechanisms of the MTI ceramic composite candle filter material are summarized and a durability modeling approach for this material is presented with a numerical example.

5.1 Failure Behavior of MTI Candle Filter Material

The failure of material is a topic of great engineering interest and there have been enormous efforts in understanding the physics of material failure process over a long period of time. For composite materials, the failure behavior usually has the following characteristics: (1) multiple failure modes (2) multiple failure stages. The knowledge about the onset of failure is usually summarized in empirical forms called failure criteria, for example the Mises or Tresca criterion for metals and the Tsai-Hill or Tsai-Wu criterion for laminated composites. It represents the onset of catastrophic failure for brittle materials or the onset of yielding for ductile materials. For non-brittle material, after the initial failure, the material still holds

together and further loading is needed to completely sever the material into several parts. In the following paragraphs, the onset of failure and post-failure behavior of the MTI ceramic composite candle filter material are discussed.

For the MTI ceramic composite candle filter material, the strength is defined as the stress level at which the first "damage event" occurs. The "damage event" typically manifests itself as the a sudden load drop in displacement controlled quasi-static tests. The strength data obtained are summarized in Figure 5.1. The stress shown is the global level stress calculated by the classical laminate theory and expressed in local material coordinates, i.e., the coordinates defined by the direction of fiber tows. Attempts have been made to fit these data to commonly used failure criteria for fiber reinforced composites, such as the Tsai-Hill and the Tsai-Wu criterion. However, the experimental data do not seem to remotely fit into any of the empirical forms.

There are a number of possible reasons to explain this discrepancy. Firstly, the stress analysis is based on the assumption that the stiffness of chopped fiber matrix is uniform across the thickness. However, the SEM investigation on the MTI candle filter material (section 2.3) has confirmed that there exists a gradient in the distribution of the bonding agent, this may result in a varying local stiffness of matrix across the thickness, which will invalidate our analysis based on the classical laminate theory. Secondly, there may be a potential size-effect involved. The C-ring test failure stress reported by Westinghouse[1] is about one order of magnitude higher than our tensile test failure stress on the 7-in tube. And the burst test failure stress on 1 to 3 inch long specimens is higher than the 7-in tube test result but smaller than the C-ring test result. The effective volume[2] in these test happens to be roughly inversely proportional to the strength data they indicated. This is an indication of the size dependence of strength commonly seen in dense ceramic materials. Thirdly,

[1]Personal communication with Dr. Rich Wagner.

[2]Stress weighted integration of specimen total volume.

the failure mode does not support the hierarchical structure of a laminated tube, in which the interfaces between laminae are the natural weak planes. Having observed the failure process of a number of tested specimens, the author noticed that the MTI filament-wound composite filter tends to fail at an intrinsic weak-plane, which is spiral a band characterized by a close-packing of fiber tows as shown in Figure 5.2. Such close-packed band is a result of the special winding process used in manufacturing the tube. Cracks tend to initiate and propagate along this plane in the early stage of failure followed by fiber tow bridging and shear failures of fiber tows in the post-failure regime. It would be more natural to express the resultant failure driving force on these weak plane.

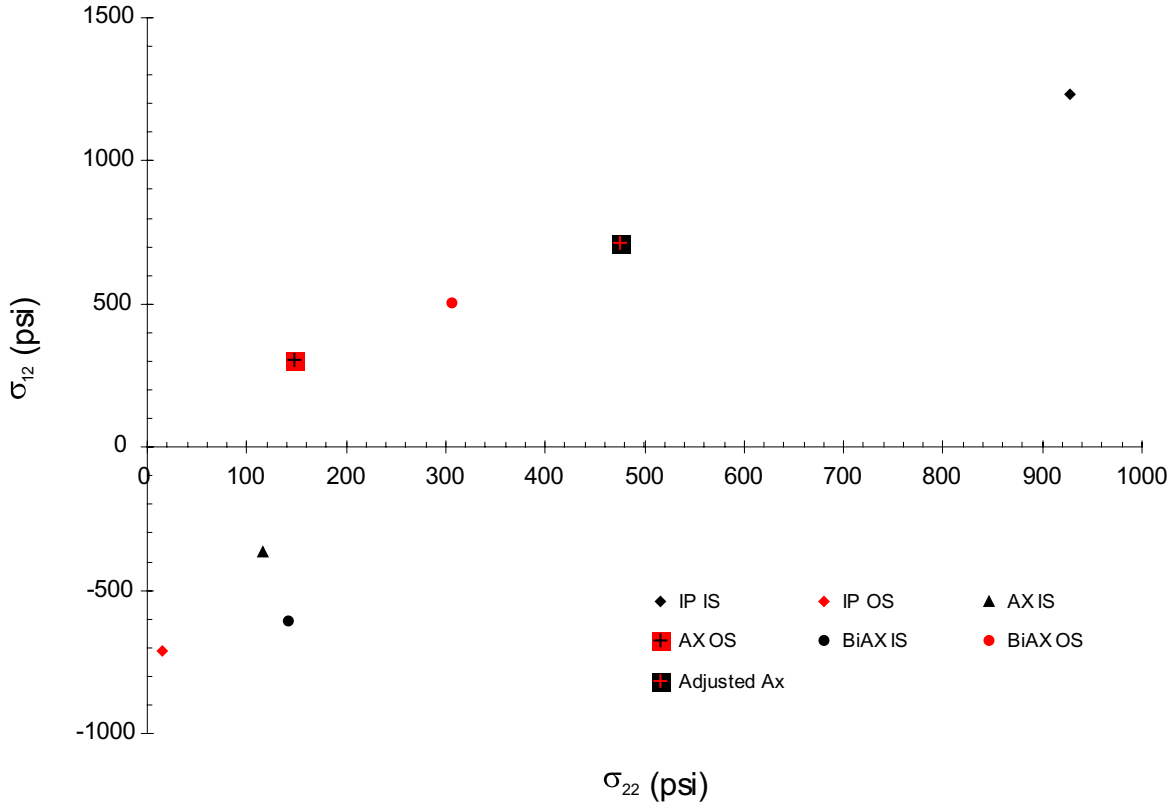

Figure 5.1: Failure stress expressed in local material coordinates. Direction 1 is fiber tow direction and direction 2 is the transverse direction to the fiber tow. IP—internal pressure test data, AX—axial test data, BiAX—bi-axial test data, IS—inner surface, OS—outer surface.

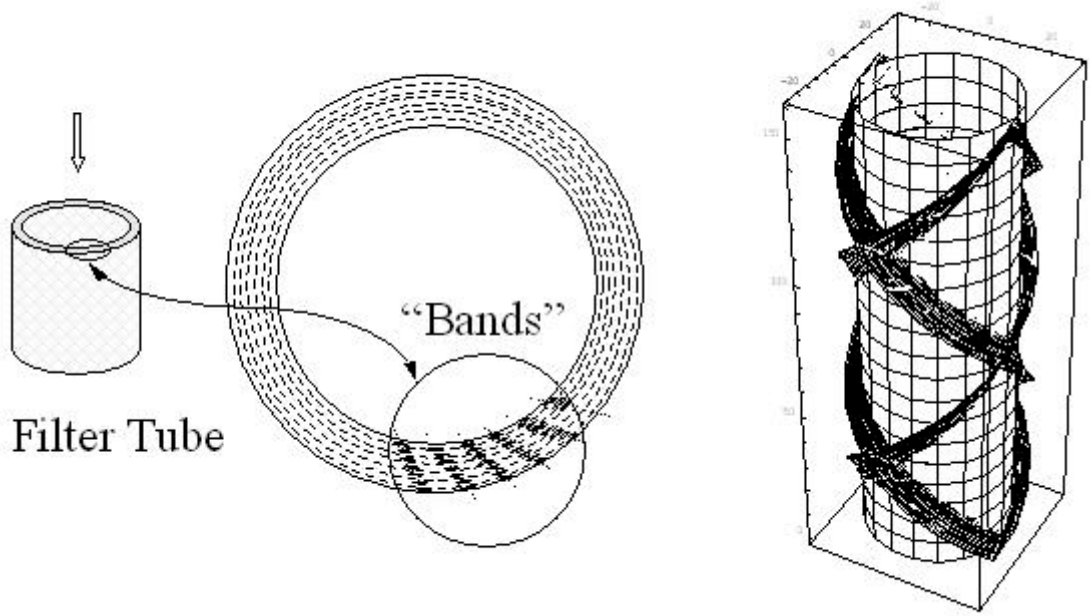

Figure 5.2: Schematics of the close-packed bands of fiber tows in the MTI candle filter material. The sub-figure to the right is a 3D rendering of the weak-plane using a mathematical description.

After initial failure, the MTI candle filter material shows a pseudo-ductile behavior when continuously loaded. When stresses in the matrix reach some critical value, it starts to crack; the matrix fails or debonds from the fiber tow before it can transfer a load to the fiber tow large enough to break it; localized crack emerges and starts growing in a brittle manor; however, the long fiber tows bridge across the crack and stabilize it before the complete fracture occurs. The reinforcing fiber tows in the MTI ceramic composite candle filter material play an important role in rendering such a non-catastrophic failure mode. The fact that the Nextel-610 fiber tow has much higher strength and stiffness than the porous matrix and the weak interface between the fiber tow and the matrix ensures the energy dissipation mechanisms observed such as fiber tow bridging, scissoring, and plowing in the matrix. To maintain such a favorable failure mode, the reinforcing fiber needs to keeps its high strength values. However, with external loading, reinforcing fiber tows take on a higher load than the matrix, and this higher mechanical load combined with high temperature exposure and other environmental conditions may cause the strength of fiber tows to degrade at a faster rate than the matrix material. The change of material state, especially that of the fiber tow, needs to be considered in a durability model to assess the long-term behavior of the MTI candle filter material.

5.2 Durability and Life Prediction

One single big problem in the design and commercialization of advanced ceramic composite candle filters is the lack of a durability evaluation tool. The range and complexity of the degradation mechanisms and the uncertainty of load and environment history make the durability evaluation task extremely challenging. In the following sections, a review of major material degradation mechanisms related to the hot gas candle filter material made of oxide/oxide composites is given; then the strength degradation of reinforcing fibers is discussed;

and finally a frame work of a life prediction methodology based on the MRLife philosophy is presented with a numerical example.

5.2.1 Degradation Mechanisms

Hot gas candle filters operate in an extremely aggressive environment. The sources of material degradation can be roughly classified into four categories. Listed below are the four sources and the potential degradation processes driven by the corresponding sources.

1. High temperature exposure $\Longrightarrow$ Grain coarsening.
2. Mechanical loading $\Longrightarrow$ Stress rupture, creep rupture, and slow crack growth (SCG).
3. Thermal shock $\Longrightarrow$ Fiber and bond breaking.
4. Corrosive chemical environment $\Longrightarrow$ Loss of fiber and bonding materials, corrosion assisted crack growth.

In following text, detailed discussions on the above degradation sources are presented.

effects of high temperature exposure

The operating temperature of candle filters in a PFBC environment is typically between 700 °C to 900 °C. Thermal exposure in this temperature range (without any mechanical load) will gradually cause a morphology change in alumina fibers, which results in a loss of fiber strength.

Many researchers [77, 78, 76] have investigated the effect of high temperature exposure on the strength of alumina fibers. The strength of Nextel-610 fiber was found to degrade with high temperature exposure. It is shown that the Nextel-610 fiber undergoes a grain coarsening

process at elevated temperature, which causes significant strength degradation. Xu, Chawla, and Li [76] also investigated the effect of thermal exposure on Nextel-610 fibers. They tested tensile strength of Nextel-610 fiber after 2-hour exposure in air at 900 °C, 1100 °C, and 1300 °C. Significant drop in fiber mean strength was found. They reported the mean strength drop from 1.651 GPa to 1.281 GPa after 900 °C thermal exposure for 2 hours in air. Significant grain growth was found following thermal exposure.

effects of mechanical loading

Filter tube needs to sustain its own weight and the weight of dust cake. Static side loads can be induced by excessive ash filling and bridging. Cyclic loading may result from transverse vibration of the candle filter and the periodic back-pulse cleaning cycle. At the micro-scale, mechanical loads result in stresses in alumina fibers, which may cause stress/creep rupture.

Wilson *et al* [73] characterized creep and creep rupture behavior of Nextel610 fiber at high temperature. He found the temperature and stress dependence of steady state creep in air is described by equation 5.1. (The unit of strain rate is $1/sec$, the unit of stress is ksi). The creep rupture mechanism was suggested to be the accumulation of cavities over either the entire fiber or at a local heterogeneity.

$$\dot{\epsilon} = 2.944 \times 10^{15} \sigma^3 \exp\left(\frac{-660KJ}{RT}\right) \tag{5.1}$$

Yun *et al* [66] studied stress-rupture behavior of Nextel-610 fiber. He found the time exponents for stress-rupture decrease for 13 at 900 °C to below 3 near 1050 °C, which suggests a transition from slow crack growth (SCG) to creep rupture as the controlling fracture mechanism.

effects of thermal shock

Thermal shock may be caused by start-up or shutdown of PFBC system. To remove ashes deposited on the outer surface of filter tube, a compressed air stream is applied in reverse direction to hot gas stream. This back-pulse cleaning cycle is used rather frequently and causes repeated thermal shock on the filter tube. Sometimes unburned coal particles attach to the outer surface of the filter; they may be ignited by hot gas stream and start to burn. This localized heating is another source of thermal shock.

We have tested a number of MTI filter tubes which have been subjected to simulated back-pulsing cleaning cycles ranging from $1,000$ to $1,000,000$. The results show that the tensile strength has degraded noticeably, while the tensile stiffness remain unchanged. Singh *et al* [57] performed oil-quenched tests on MTI composite candle filter. They found negligible strength loss when temperature difference is below $900\,^{\circ}\mathrm{C}$.

corrosion effects

PFBC hot gas environments can be roughly classified into two types: oxidizing environment and reducing environment. Oxidizing environments are characterized by high contents of oxygen. Reducing environments are characterized by high contents of carbon monoxide and hydrogen. Depending on the type of coal, hot gas stream contains various amount alkali metals and other corrosive agents. Alumina (aluminum oxide) based composite candle filters have much better corrosion resistance than SiC based candle filters. Spear *et al* [58, 56] conducted research on the corrosion of ceramic candle filters. Their thermal dynamic based simulation showed that the removal of aluminum from alumina/mullite by hydroxide gaseous species is almost three orders of magnitude less severe than the removal of silicon by its hydroxides. Alvin [3] reported that oxide-based material would react with gas-phase alkali forming stable solid complexes.

combined effects

Little is known about the combined effect of thermal exposure, mechanical load, and corrosion environment on the mechanical properties of composite candle filter material. Real field tests are required to investigate material degradation behavior under combined sources.

Westinghouse has conducted several test campaigns to evaluate the viability of advanced CFCC candle filters by placing them in real PFBC demonstration plants. MTI oxide/oxide composite filters were field tested at the Forster Wheeler PFBC demonstration facility at Kahula, Finland. The MTI filter tubes were installed in the filtration module and ran up to 581 hours. After field exposure, the filter tubes were subsequently examined for material degradation. Alvin [3] reported the moderate material degradation of MTI candle filters after the Kahula field test. An approximately 10% C-ring compressive strength loss was reported for MTI candle filter.

Singh [57] evaluated the in-situ strength of Nextel-610 fiber in a 3M ceramic composite candle filter by using the fracture mirror technique. He found that after 1100 hours of exposure in Tidd demonstration plant, the mean Nextel fiber strength decreases about 50% and the Weibull modulus increased slightly. This decrease in strength should be a combined effect of grain growth and SCG. The decreasing of mean strength is in accordance with the observations of Xu *et al* [76] and Yun *et al* [77, 78]. But the increase of Weibull modulus is unexplained.

fiber strength degradation kinetics

Acquiring fiber stiffness/strength degradation data is key in evaluating the long term behavior. Alumina fibers are very stable in an oxidizing environment. At high temperature the fine polycrystalline alumina fiber undergoes a grain coarsening process, which causes the degradation of strength. Yun *et al* [77, 78] has published data on the strength degradation

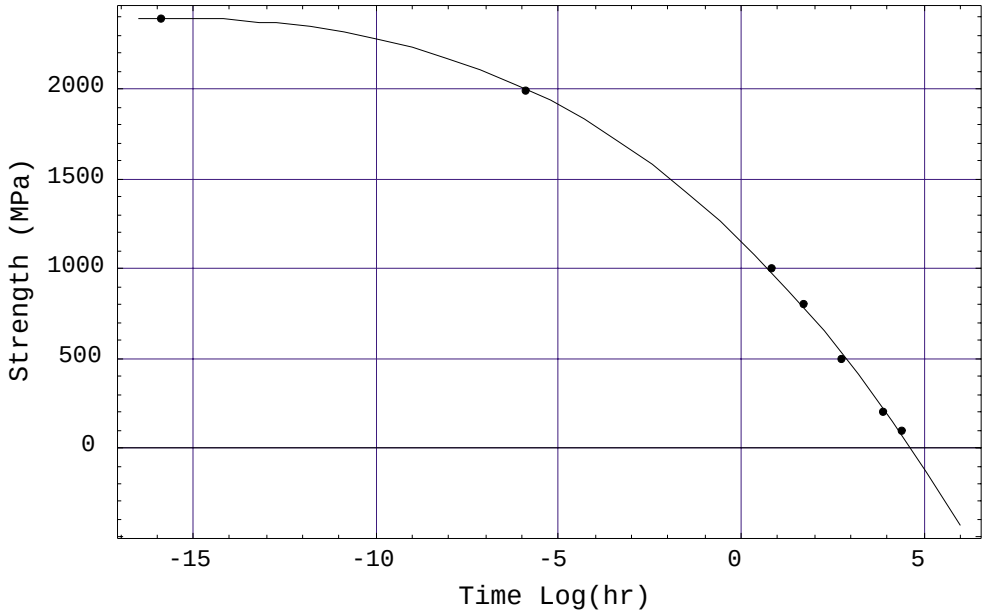

Figure 5.3: Strength degradation kinetics of Nextel-610 fiber at 871 °C in air.

of single filament Nextel-610 under thermal exposure, which is shown in Figure 5.3.

5.2.2 Damage Accumulation Concept

Life prediction of composite material systems under fatigue and other loading conditions has been the subject of many investigations. S-N curves generated by coupon tests under controlled laboratory environment are required as the basis for prediction. In the case of the creep rupture or the stress rupture problem, S-t_f curves are required as input to the life prediction model. The effects of complex load history are treated by assuming some damage accumulation laws, among which the Palmgren-Miners rule is the most widely known.

The damage accumulation concept is the central idea of life prediction. The external load history causes some irreversible change of the state of material and most of the time this

change causes a strength or residual life degradation. This change of material state is coined "damage". People have tried to relate this "damage" to some measurable physical quantities such as stiffness reduction or residual strength. Poursartip *et al* [47] assumed that stiffness reduction is related to the "damage" in a linear fashion. Material fails when the "damage" reaches a critical value, which can be represented by a critical stiffness reduction. Broutman and Sahu [5] proposed a cumulative damage theory based on residual strength degradation. Failure is assumed to occur when the residual strength becomes equal to the applied stress. They predicted fatigue life of a glass fiber reinforced polymer composites under multi-stage loading conditions.

Reifsnider and his coworkers [49, 48, 50] proposed a critical element model to predict the residual strength and life of a composite material system by making the assumption that residual strength is a state variable. By using a thermal dynamics argument, he proposed the form of kinetic laws (Equation 5.5) for residual strength evolution as a function of applied load and time. By generating the concept of equivalent time, both the fatigue and creep rupture effects can be incorporated in this unified framework. Case [7] later applied this model to polymeric and ceramic composite material systems. The predicted result compares reasonably well to laboratory data.

5.2.3 Coupled Damage and Finite Element Analysis

The delayed failure of filter tubes is determined by three factors at that time: the external load, the material state, and the stress state. All of the three factors are complex functions of time. They are also coupled to each other in a nonlinear fashion. For example, the creep rate of alumina fiber is proportional to the third power of axial stress in the fiber. The grain coarsening rate of alumina fiber depends on the temperature in an Arrhenius type of equation.

Before any meaningful long-term behavior predictions can be made, questions such as, what controls the failure behavior? what is the "critical element" in the material system? have to be answered. Accroding to the observed failure modes of the MTI composite filters, Nextel-610 fiber tows are the controlling elements that renders an overall graceful failure behavior of the composites. In the MTI composite materials sytem, fiber tow has a higher strength than the porous matrix and a weak bonding exists between the fiber tow and the porous matrix. These features correlate to the observed energy dissipation mechanisms that lead to improved material toughness in the failure process. However, micro-mechanics modeling showed that global stiffness contribution from fiber tows is minimal except for the case of torsion. Since the focus here is the failure behavior, we will concentrate our analysis on the stress state and material state in the fiber tows and we assume that Nextel-610 fiber tows are the "critical elements" in the sense that their failure define the final failure of the composite material system.

A finite element and damage mechanics coupled model for predicting the residual strength and service life was built. Two assumptions were made to simplify the model: (1) failure is defined when the first fiber tow breaking occurs (2) loads are carried by fiber tows only. In this model, fiber tows are modeled by 3D frame elements, which carry both axial and bend loads. The effect of matrix is put into a torsion member between the cross over point of two fiber tows. Constant load and temperature are assumed. Only stiffness and strength reduction of fiber tows are considered. Kinetic laws for stiffness and strength as a function of time are fitted into a third order polynomial form. A FEM code was developed to solve the boundary value problem. The system stiffness matrix is modified for every time step. Strength reduction on a pre-selected critical element is summed during the iteration process. The program is terminated after the first break of the fiber tow. A failure function is defined to be the ratio of maximum tensile stress over the tensile strength on the critical element. Damage accumulation is based on the model proposed by Reifsnider and Stinchcomb. The

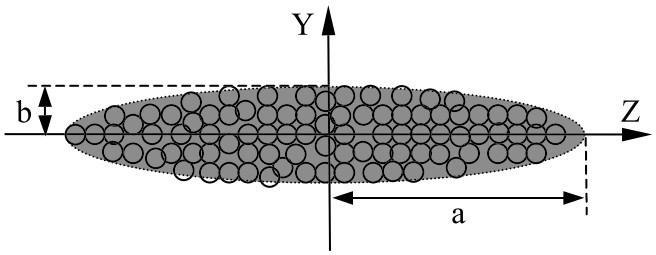

Figure 5.4: Idealized cross-section geometry of a fiber tow.

flow chart is shown in Figure 5.5. Figure 5.6 shows a predicted F_r (failure function) and F_a (applied load) as a function of time.

Conceivablely, the most severely loading condition for the slender filter tube is the side load exerted near its free end. This is may be the result of unsymmetrical gas flow patterns, ash bridgings, etc. High bending moment may result near the root of the clamped tube. Because of the close arrangement of filter tubes in the filter module, one failed tube may "hit" nearby tubes and so forth casuing a cascading failure of many tubes. At one time, in Wilsonville PFBC test facility, cascading bend failure broke hundreds of tubes[3]. Here, we model a small volume of material near the tensile side of a bend-loaded tube. The tensile load is assumed to be 77.4 N, which corresponds to a 9.675 MPa nominal stress as a result of a 100 $N \cdot m$ bending moment. This is a very high load when compared to the observed failure moment (from 100 to 150 $N \cdot m$) in the cantilever bend test.

Stress on a cross-section of a fiber tow was calculated by the following equation:

$$\sigma = \frac{M_z}{I_z} y + \frac{M_y}{I_y} z + \frac{N_x}{A} \tag{5.2}$$

In which,

[3]Personal communication with Dr Rich Wagner.

$$I_z = \frac{1}{4}\pi ab^3,\ I_y = \frac{1}{4}\pi a^3 b,\ A = \pi ab$$

If knowing the bending moment and the torque load on the fiber tow, the maximum tensile stress in the cross-section can be shown to be:

$$\sigma_{max} = \frac{4}{\pi}\left(\frac{M_z^2}{b^2\sqrt{a^2M_z^2 + b^2M_y^2}} + \frac{M_y^2}{a^2\sqrt{a^2M_z^2 + b^2M_y^2}} + \frac{N_x}{4ab}\right) \tag{5.3}$$

We assumed the load function and failure function to be:

$$F_a = \frac{\sigma_{max}}{X_t},\ F_r = \frac{S_r}{X_t} \tag{5.4}$$

In which, X_t is the ultimate tensile strength of the fiber. S_r is the residual tensile strength. And we assume failure occurs when $F_a = F_r$. The evolution of F_r is assumed to follow this equation proposed by Reifsnider and Stinchcomb [50].

$$F_r = 1 - \int_0^\tau \left(1 - F_a\left(\tau\right)\right) j\tau^{j-1} d\tau \tag{5.5}$$

In which, j is a material constant obtained by curve fitting experimental data and τ is the characteristic time defined as:

$$\tau = \begin{cases} \frac{t}{t_r}, & \text{creep rupture} \\ \frac{n}{N}, & \text{fatigue} \end{cases} \tag{5.6}$$

A numerical integration scheme of equation 5.5 established by Case [7] was adopted. In his method, for a small time step, the change of residual strength is approximated by:

$$\Delta F_r = -\left(1 - F_a\right)\left\{\left[\frac{n^0 + \Delta N}{N}\right]^j - \left(\frac{n^0}{N}\right)^j\right\} \tag{5.7}$$

$$\Delta F_r = -\left(1 - F_a\right)\left\{\left[\frac{t^0 + \Delta t}{t_r}\right]^j - \left(\frac{t^0}{t_r}\right)^j\right\} \tag{5.8}$$

In which, N is the fatigue life for present stress level, t_r is time to rupture at present temperature and stress level. t^0 and n^0 are pseudo-time and pseudo-cycle defined as:

$$t^0 = \left(\frac{1 - F_r}{1 - F_a}\right)^{\frac{1}{j}} t_r,\ n^0 = \left(\frac{1 - F_r}{1 - F_a}\right)^{\frac{1}{j}} N \tag{5.9}$$

Numerically, the value of F_r is obtained by integrated by following formula:

$$F_r = 1 + \sum_{\Delta t} \Delta F_r + \sum_{\Delta n} \Delta F_r \tag{5.10}$$

The dependence of N and t_r on stress level are obtained by curve fitting independent experimental data for fatigue and stress rupture tests. Because currently fatigue data is not available, some guessed value is used. Creep rupture data came from the experiment result of Yun [77, 78]. The creep rupture data is fitted into a third-order polynomial:

$$\frac{T}{1000}\left(\log\left(t_r\right) + 22\right) = A + B \cdot F_a + C \cdot F_a^2 + D \cdot F_a^3 \tag{5.11}$$

In which, T is absolute temperature in Kelvin, t_r is creep rupture time to failure in hours. A, B, C, and D are curve fitting constants.

The above damage evolution procedure is coupled to a finite element code that calculates and updates the resultant bending moment and axial tensile load in the fiber tow. The program terminate when $F_a = F_r$. At a load level of 77.4 N the time to failure was calculated to be 5700 hours. This is an extremely conservative estimation due to the simplifying assumptions.

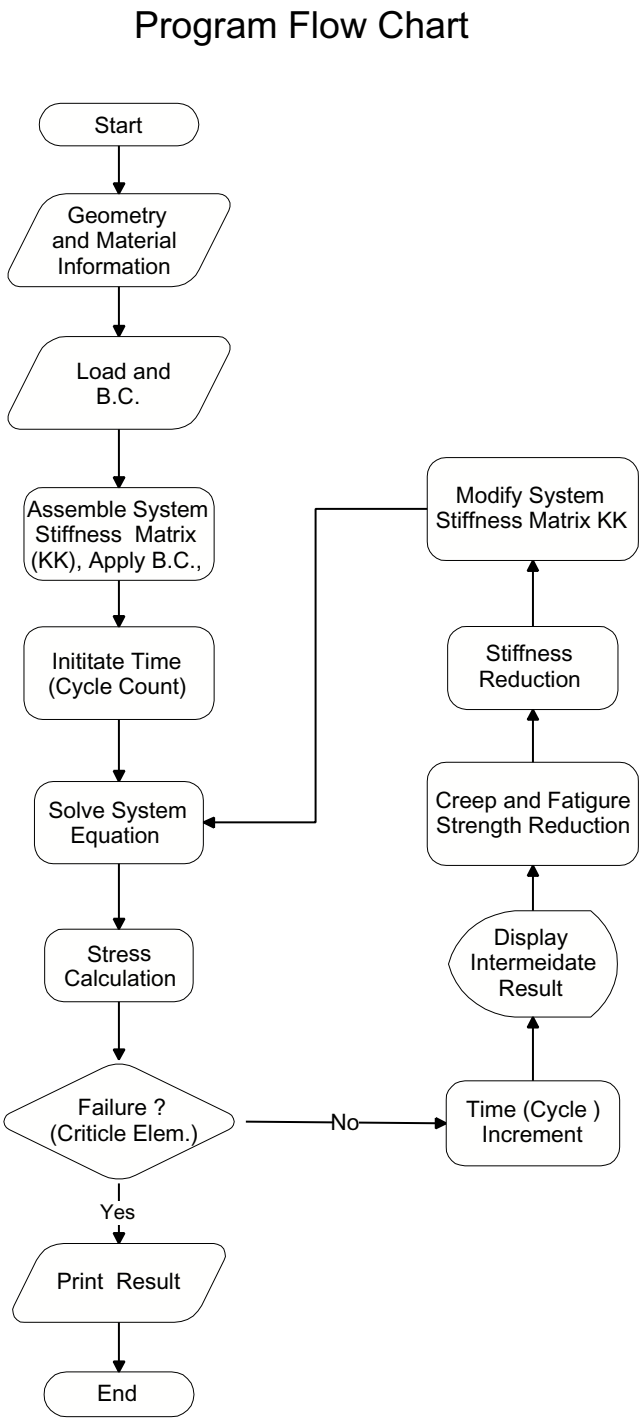

Figure 5.5: Program flow-chart of the life prediction code.

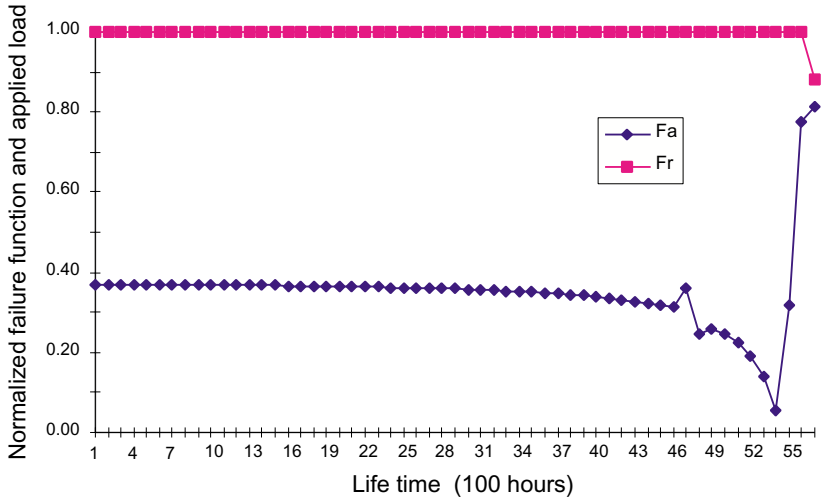

Figure 5.6: Predicted residual strength as a function of time.

Chapter 6

Summary and Conclusion

The author's dissertation research has been focused on the subject: *porous ceramics and fiber reinforced porous ceramic composites.* Both experimental and theoretical work have been conducted to characterize and to model the mechanical behavior and durability of this novel functional material. The results represent the current state-of-the-art understanding of the mechanical behavior of highly porous ceramic composite materials, especially the relationship between the microstructure and macro effective properties. In the following sections, a summary on the dissertation research, several major conclusions, and future work are presented.

6.1 Summary

The structure of the research work is schematically illustrated in Figure 6.1. Extensive experiments were performed on the MTI hot gas candle filter, a fiber reinforced porous ceramic composites. Quasi-static tests were conducted at both room temperature and elevated temperature to characterize the stiffness, failure modes, and the strength of this material.

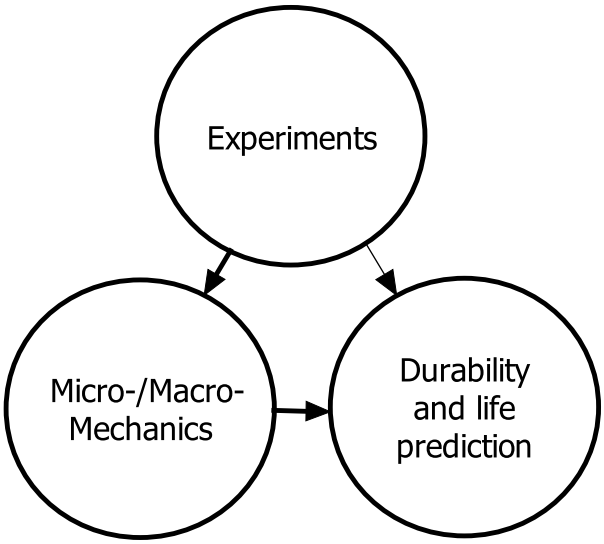

Figure 6.1: Structure of the dissertation research.

Theoretical work includes micro-mechanics modeling of highly-porous heterogeneous materials and meso-/macro-mechanics modeling of the continuous fiber reinforced porous ceramic matrix composites. The author has devised a novel computational micro-mechanics approach to simulate highly porous material with stochastic microstructures. This method is suitable to model random fibrous networks, which represents the microstructure of many porous functional materials including hot gas candle filter, paper, and trabecular bone. Meso-/macro-mechanics models were constructed to model fiber reinforced porous matrix systems. An analytical scheme—the energy method—was formulated based on the principle of stationary potential energy. Closed-form equations are obtained to predict the global effective stiffness as a function of fiber tow architecture in the MTI ceramic composite system. The predicted results compared favorably with the experimental data obtained on the MTI candle filter material system. In addition to the analytical method, a finite element modeling scheme was also identified to model the reinforced composites at the fiber tow level (meso-scale). Attempts have been made to understand the durability issues of ceramic composite hot gas candle filters. A hot gas candle filter is required to maintain its mechanical prop-

erties in an extremely aggressive working environment. Material degradation mechanisms related to an oxide/oxide composite filter material were reviewed and the framework of a life prediction method based on coupled damage mechanics and finite element simulation was demonstrated. Because of limited experimental supporting data, the method has not been calibrated and verified against experimental results.

6.2 Conclusions

MTI Hot Gas Candle Filter Material

From the room temperature tests, good measurements of filter tube stiffnesses were obtained. The tensile stiffness of the filter tube obtained was about 500 ksi and the torsional stiffness was about 1000 ksi. Analytical models for stiffness were established; they showed good correlations with experimental values. The test results showed that the porous ceramic composite filter material failed in a non-catastrophic fashion at room temperature. In tension, the failure was caused by tow-matrix debonding and shear along the "weak-plane" explained in the previous chapter. In compression, the failure was caused by surface layer buckling and delamination. For bending, surface layer buckling or out-of-plane shear failures were all possible depending on the load level. Different failure modes were observed in tube pull out tests and ring burst tests. In the burst tests, short specimens were used. The fiber tows were severed in the high stress region near the free edge. In tension tests, longer specimens were used; fiber tows in the gage section remained intact. In the burst test, fiber tows did not break but the matrix material was crushed; while in the tension test, fiber tows broke along a long spiral shear crack. The burst strength results did not reflect the "true" strength of the filter tube under real working conditions; instead it could be used as an indication of how well the fiber tows were bonded and/or how strong the chopped fiber matrix was, i.e., a

lower bound on usable strength. The test results of thermally-cycled specimen showed that the simulated back-pulsing cycles had no significant effect on the stiffness of filter tube but caused noticeable degradation of filter strength.

Micro-/Meso-Mechanics Modeling

Chapter 3 reported the development of a computational micro-mechanics approach that can be used to predict the effective elastic properties of highly porous materials with random microstructures. The approach was based on a novel method to estimate the average strain in the RVE of a highly porous material. This novel method was tested by a number of numerical examples; fairly accurate results were obtained and the algorithm was also shown to be robust, i.e., insensitive to random errors of input data. With the help of the strain energy equivalence principle, a micro-mechanics method was established to estimate the effective elastic properties of highly porous materials. The approach was implemented in a random network simulation code called FIBNET. The code was applied to a honeycomb material, and the predicted effective properties were compared with literature data with reasonably good agreements.

Chapter 4 reported the development of an energy method that is capable of predicting the tensile and torsional stiffness of a candle filter tube. Results compared reasonably well with experimental data. Since the representation of the constituents was explicit and analytical, the stresses and strains in the constituents could be extracted from the results of the calculations. A numerical variety of the energy method—the ligature model—was developed and this model is amenable to finite element constructions, so that it is easily applied to complex global shapes, and locally non-uniform stress states and material states. The model is computationally simple, and can, therefore, be applied in such a way that represents essentially all of the actual constituent details over comparatively large areas of analysis. Predictions

of stiffness of the MTI tow-wound filter materials showed agreement within ten percent of observed values.

Durability of Porous Ceramic Composites

Chapter 5 reported a durability modeling approach for ceramic composite candle filter material. This is a frame work of a general methodology and the real application requires a number of supporting data such as the stress rupture life of fiber tow, the corrosion rate of alumina fibers, the long-term failure mode, etc. The approach needs to be validated against real test results, especially when multiple failure mechanisms need to be incorporated in the life prediction.

6.3 Future Work

Future work on micromechanics modeling includes the investigation of the effect of relative density and fiber orientation distribution on the effective properties. In the two dimensional model, the fibers are assumed to lie in a 2D plane, but fibers actually stack on each other, loading the microstructure would result not only tension and bending, but also torsion deformation of small fibers. So a natural progression is to extend the 2D micro-mechanics model to 3D fibrous network. The micro-mechanics model was currently used to predict the effective stiffness. It is worth trying to extend the micromechanics model to simulate the failure process, which is of great engineering importance. Incorporation of micro-mechanics models into the life prediction effort is another future research direction. The degradation of material properties for material with complex microstructure is currently treated with phenomenological mothods. The material damage state is described by a scalar or tensorial variable. The actual "physics" meaning of this damage variable is blurred. The micro-

mechanics model would be an ideal tool to reveal the missing linkage between microstructure evolution and the abstract damage variable.

Bibliography

[1] Jacob Aboudi. *Mechanics of Composite Materials—A Unified Micromechanics Approach*. Elsevier, Amsterdam, 1991.

[2] T. Akasaka. Advances in structural mechanics of rubber composites. In *Proceedings of the Sixth Japan-U.S. Conference on Composites Materials*, pages 3–25. Air Force Office of Scientific Research, Technomic Publishing Co., June 1992.

[3] Mary Anne Alvin, Tomas E. Lippert, Edward S. Diaz, Eugene E. Smeltzer, and Gerald J. Bruck. Filter component assessment. Technical Report DE-AC21-94MC31147, DOE.

[4] Mary Anne Alvin, Tomas E. Lippert, Eugene E. Smeltzer, and Gerald J. Bruck. Advanced hot gas filter performance and characterization. Technical Report DE-AC21-94MC31147, DOE.

[5] L. J. Broutman and S. Sahu. A new damage theory to predict cumulative fatigue damage in fiberglass reinforced plastics. In *Composite Materials: Testing and Design*, ASTM STP 497, pages 170–188. 1972.

[6] G. A. Carnaby and Ning Pan. Theory of the compression hysteresis of fibrous assemblies. *Textile Res. J.*, 59:275–284, 1989.

[7] Scott W. Case. *Mechanics of Fiber Controlled Behavior in Polymeric Composites*. PhD thesis, Virginia Polytechnic Institute and State University, May 1996.

[8] C. Chapman and J. D. Whitcomb. Effect of assumed tow architecture on predicted moduli and stresses in plain weave composites. *Journal of Composite Materials*, 29(16):2134–2159, 1995.

[9] C. C. Chen and K. E. Duckett. The direction distribution on cross-contacts points in anisotropic fiber assemblies. *Textile Res J.*, 49:379, 1979.

[10] H. L. Chen and Alejandro C. Kiriakidis. Nondestructive dynamic characterization of ceramic candle filters. In *Symp. of High Temperature Particulate Cleanup for Advanced Coal-Based System*, pages 308–319, Palo Alto, California, March 1998. EPRI.

[11] H. L. Chen and Alejandro C. Kiriakidis. Stiffness evaluation and damage detection of ceramic candle filters. *Journal of Engineering Mechanics*, pages 308–319, March 2000.

[12] Richard M. Christensen. *Mechanics of Composite Materials*. Wiley, New York, 1979.

[13] B. N. Cox, W. C. Carter, and N. A. Fleck. A binary model of textile composites—I. formulation. *Acta metall. mater.*, 42(10):3462–3479, 1994.

[14] H. L. Cox. The elasticity and strength of paper and other fibrous materials. *British Journal of Applied Physics*, 3:72–79, 1952.

[15] A. Dasgupta and S. M. Bhandarkar. Effective thermomechanical behavior of plain weave fabric reinforced composites using homogenization theory. *Journal of Engineering Materials and Technology*, 116:99–105, 1994.

[16] Yu. I. Dimitrienko. Modeling of the mechanical properties of composite materials at high temperatures. part 1. Matrix and fibers. *Applied Composite Materials*, 4(4):219–237, 1997.

[17] Yu. I. Dimitrienko. Modeling of the mechanical properties of composite materials at high temperatures. part 2. Properties of unidirectional composites. *Applied Composite Materials*, 4(4):239–261, 1997.

[18] Yu. I. Dimitrienko. Modeling of the mechanical properties of composite materials at high temperature. part 3. Textile composites. *Applied Composite Materials*, 5(4):257–272, 1998.

[19] A. Fujita, A. Yokoyama, and H. Hamada. Simulation system for mechanical behaviors for textile composites. In *Computational Mechanics'95: Theory and Applications*, pages 2311–2316, Hawaii, July 1995. International Conference on Computational Engineering Science.

[20] E. J. Garboczi and J. G. Berryman. Elastic moduli of a material containing composite inclusions: Effective medium theory and finite element computations. *Mechanics of Materials*, 33:455–470, 2001.

[21] Lorna J. Gibson and Michael F. Ashby. *Cellular Solids: Structure and Properties.* Cambridge Solid State Science Series. Cambridge University Press, Cambridge, UK, 2nd edition, 1997.

[22] E. H. Glaessgen, O. H. Griffin, C. M. Pastore, and A. Birger. Modeling of textile composites. *ICCE*, (1):183–184, 1994.

[23] Zvi Hashin. The elastic moduli of heterogeneous materials. *Journal of Applied Mechanics*, 29:143–50, 1962.

[24] Zvi Hashin. Analysis of composite materials—a survey. *Journal of Applied Mechanics*, 50:481–505, 1983.

[25] Zvi Hashin and B. W. Rosen. The elastic moduli of fiber reinforced materials. *Journal of Applied Mechanics*, 31:223–32, 1964.

[26] Hibbitt Karlsson & Sorensen Inc. *ABAQUS Theory Manual*, 5.7 edition, 1997.

[27] S. J. Hollister, J. M. Brennan, and N. Kikuchi. A homogenization sampling procedure for calculating trabecular bone effective stiffness and tissue level stress. *J. Biomechanics*, 27(4):433–444, 1994.

[28] Michael W. Hyer. *Stress Analysis of Fiber-Reinforced Composite Materials*. WCB/McGraw-Hill, 1998.

[29] H. Ichihashi, H. Hamada, N. Ikuta, and Z. Maekawa. Finite element analysis of woven fabric composites considering interfacial properties. In *Annual Meeting of the Society of Interfacial Science in Composites*, volume 2, Japan, 1994.

[30] T. Ishikawa and T. W. Chou. Elastic behavior of woven hybrid composites. *Journal of Composite Materials*, 16:2–19, 1982.

[31] T. Ishikawa and T. W. Chou. Stiffness and strength behavior of woven fabric composites. *Journal of Material Science*, 17:3211–20, 1982.

[32] T. Ishikawa and T. W. Chou. In-plane thermal expansion and thermal bending coefficients of fabric composites. *Journal of Composite Materials*, 17:92–104, 1983.

[33] Robert M. Jones. *Mechanics of Composite Materials*. McGraw-Hill, New York, 1975.

[34] O. Kallmes and H. Corte. The structure of paper, I: The statistical geometry of an ideal two-dimensional fiber network. *Tappi*, 43:737, 1960.

[35] O. Kallmes, H. Corte, and G. Bernier. The structure of paper, V: The free fiber length of a multi planar sheet. *Tappi*, 46(108), 1963.

[36] Henry L. Langhaar. *Energy Methods in Applied Mechanics*. Robert E. Krieger Publishing Co., Inc., Krieger Drive, Malabar, Florida 32950, reprint from original edition 1962 edition, 1989.

[37] D. H. Lee and J. K. Lee. Initial compressional behavior of fibre assembly. In S. Kawabata, R. Postle, and M. Niwa, editors, *Objective Measurement: Applications to Product Design and Process Control*, pages 618–622. 1985.

[38] J. Lemaitre and J.-L. Chaboche. *Mechanics of Solid Materials*. Cambridge University Press, 1990.

[39] T. E. Lippert and R. A. Newby. High-temperature particulate control. In M. Alvarez Cuenca and E. J. Anthony, editors, *Pressurized Fluidized Bed Combustion*. Blackie Academic and Professional, 1995.

[40] S. Meille and E. J. Garboczi. Linear elastic properties of 2D and 3D models of porous materials made from elongated objects. *Modeling Simul. Mater. Sci. Eng.*, 9:371–379, 2001.

[41] A. Nakai and H. Hamada. Influence of braiding structure on torsional properties of braided composite tube. In *Computer Technology: Applications and Methodology*, volume 326 of *PVP, ASME*, pages 125–130. 1996.

[42] Sia Nemat-Nasser and M. Hori. *Micromechanics: Overall Properties of Heterogeneous Materials*.

[43] A. H. Nissan and Batten G. L., Jr. On the primacy of the hydrogen bond in paper mechanics. *Tappi*, 73:159, 1990.

[44] M. Ostoja-Starzewski and K. Alzebdehand I. Jasiuk. Linear elasticity of planar delaunnay networks III: Self-consistent approximations. *Acta Mechanica*, 110:57–72, 1995.

[45] M. Ostoja-Starzewski and C. Wang. Linear elasticity of planar delaunnay networks: Random field characterization of effective moduli. *Acta Mechanica*, 80(4):61–80, 1989.

[46] M. Ostoja-Starzewski and C. Wang. Linear elasticity of planar delaunnay networks, part II: Voigt and reuss bounds, and modification for centroids. *Acta Mechanica*, 84:47–61, 1990.

[47] A. Poursartip, M. F. Ashby, and P. W. R. Beaumont. Damage accumulation during fatigue of composites. *Scripta Metallurgica*, 16:601–606, 1982.

[48] Ken L. Reifsnider, Scott W. Case, and Y. Xu. A micro-kinetic approach to durability analysis: the critical element method. In *Keynote address, International Conference on Durability of Composite Material Systems*, July 1995.

[49] Ken L. Reifsnider, N. Iyengar, Scott W. Case, and Y. Xu. Kinetic methods for durability and damage tolerance design of composite components. In *Keynote Address, Conference on Composite Materials*, Tokyo, Japan, June 1995. Japan Society for Mechanical Engineers.

[50] Ken L. Reifsnider and W. W. Stinchcomb. A critical element model of the residual strength and life of fatigue-loaded composite coupons. In H. T. Hahn, editor, *Composite Materials: Fatigue and Fracture*, ASTM STP 907. Philadelphia.

[51] A. P. Roberts and E. J. Garboczi. Elastic moduli of model random three-dimensional closed-cell cellular solids. *Acta mater.*, 49:189–197, 2001.

[52] Sanchez-Palencia. *Non-Homogeneous Media and Vibration Theory.* Springer, Berlin, 1980.

[53] B. V. Sankar and R. V. Marrey. Analytical method for micromechanics of textile composites. *Composite Science and Technology*, 57:703–713, 1997.

[54] A. M. Sastry, X. Cheng, and C. W. Wang. Mechanics of stochastic fibrous networks. *Journal of Thermoplastic Composite Materials*, 11:288–296, 1998.

[55] A. M. Sastry, C. W. Wang, and L. Berhan. Deformation and failure in stochastic fibrous networks: Scale dimension and application. *Key Engineering Materials*, 200:229–250, 2001.

[56] D. L. Shelleman, K. E. Spear, C. E. Crossland, and R. E. Tressler. High temperature corrosion of advanced ceramic materials for hot gas filters and heat exchangers. Technical Report ORNL/Sub/94-SS111/03.

[57] J. P. Singh, S. Majumdar, M. Sutaria, and W. Bielke. Fracture behavior of advanced ceramic hot gas filters: Final report. Technical Report ORNL/Sub/94-SS107V/01, 1997.

[58] K. E. Spear, C. E. Crossland, D. L. Shelleman, and R. E. Tressler. High temperature corrosion of advanced ceramic materials for hot gas filters. Technical Report ORNl/Sub/94-SS111/02, 1994.

[59] D. Stinton, R. Judkins, B. Smith, and Ed Fischer. Ceramic filters. *CFCC News*, pages 12–13, Spring 1996.

[60] C.-T. Sun and R.-S. Vaidya. Prediction of composite properties from a representative volume element. *Composites Science and Technology*, 56:171–179, 1996.

[61] P. Tan, L. Tong, and G. P. Seven. A 3D modeling technique for predicting the linear elastic properties of open-packing woven fabric unit cell. In *Ninth International Conference on Composite Structure*, Paisley, Scotland.

[62] S. P. Timoshenko and J. N. Goodier. *Theory of Elasticity.* Classic Textbook Re-Issue. McGraw-Hill, Inc., 3rd edition, 1987.

[63] S. Torquato. Random heterogeneous media: Microstructure and improved bounds on effective properties. *Appl. Mech. Rev.*, 44(2), 1991.

[64] S. Torquato. Modeling of physical properties of composite materials. *International Journal of Solids and Structures*, 37:411–422, 2000.

[65] C. M. van Wyk. Note on compressibility of wool. *J. Textile Inst.*, 37:T285–T292, 1946.

[66] Richard A. Wagner. Ceramic composite hot gas filter development. In *Proceedings of the Advanced Coal-Based Power and Environmental Systems'98 Conference*, 1998.

[67] C. Wang, X. Cheng, A. M. Sastry, and S. B. Choi. Investigation of failure processes in porous battery substrates: Part I—experimental findings. *Journal of Engineering Materials and Technology*, 121:503–513, 1999.

[68] C. Wang, X. Cheng, A. M. Sastry, and S. B. Choi. Investigation of failure processes in porous battery substrates: Part II—simulation results and comparisons. *Journal of Engineering Materials and Technology*, 121:514–523, 1999.

[69] C. W. Wang, L. Berhan, and A. M. Sastry. Structure, mechanics and failure of stochastic fibrous network: Part I—microscale considerations. *ASME Journal of Engineering Materials and Technology*, 122:450–459, 2000.

[70] C. W. Wang and A. M. Sastry. Structure, mechanics and failure of stochastic fibrous networks: Part II—Network simulations and application. *ASME Journal of Engineering Materials and Technology*, 122:460–468, 2000.

[71] J. D. Whitcomb. Iterative global local finite element analysis. *Computers and Structures*, 40(4):1027–1032, 1991.

[72] J. D. Whitcomb and K. Woo. Application of interactive global local finite element analysis. Part I: Linear analysis. *Communications in Numerical Methods in Engineering*, 9:745–756, 1993.

[73] D. M. Wilson, D. C. Lueneburg, and S. L. Lieder. High temperature properties of Nextel 610 and alumina-based nano-composite fibers. *Ceramic Engineering and Science Proceedings*, 14(7–8):609–621, 1993.

[74] K. Woo and J. D. Whitcomb. Global local finite element analysis for textile composites. *Journal of Composite Materials*, 28(14):1305–1321, 1994.

[75] J. Xu, B. N. Cox, M. A. McGlockton, and W. C. Carter. A binary model of textile composites II: The elastic regime. *Acta metall. Mater.*, 43(9):3511–3524, 1995.

[76] Z. R. Xu, K. K. Chawla, and X. Li. Effect of high temperature exposure on the tensile strength of alumina fiber Nextel 610. *Materials Science and Engineering*, A171:249–256, 1993.

[77] H. M. Yun and J. A. DiCarlo. Time/temperature dependent tensile strength of SiC and Al_2O_3-based fibers. *Ceramic Transactions*, 74:17–25, 1996.

[78] H. M. Yun, J. C. Goldsby, and J. A. DiCarlo. Stress-rupture behavior of small diameter polycrystalline alumina fibers. *Ceramic Transactions*, 38:713–724.

Appendix A

Mechanisms and Sources of Filter Failure

Table A.1: Mechanisms and sources of filter element failure. [39]

Mechanism	Source
Short-term	
Mechanical shock	Filter vessel ash filling or bridging
	High loading dust excursion
Thermal shock	High gas temperature excursion
Chemical shock	Low permeability coating formation during off-design conditions
Long-term	
Thermal exposure	Continuous degradation such as flow of the binder phase
Temperature transients	PFBC start-ups and shut-downs
	Pulse cleaning cooling
Bulk gas reactions	Oxidation of non-oxide ceramics, gas phase moisture, volatilization
Gas phase trace contaminants	Alkali vapour (and others), reacting with amorphous phase and weakening material strength
Fly ash interactions	Adherence along amorphous glass phase, and subsequent pore plugging, reaction of fines with ceramic

Appendix B

Matlab Code to Calculate Average Strain

```
function [Epsilon, area_tot] = avgstrain2(A, varargin)

%AVGSTRAIN2  calculate average strain of a region in 2-D cartesian space
%
%  [Epsilon] = avgstrain2(A) calculates average strain of a region
%  in 2-D cartesian space based on the displacements of a number of
%  key points in that domain by means of trianglar tessalation and
%  second-order displacement interpolation.
%
%  'Epsilon' is a an array containing three calculated average engineering
%  strain values, i.e., E_x, E_y and Gamma_xy; if more than one disp cases
%  are specified in A, results will be arranged like:
%
%                  case1,    case2,    ...
%      Epsilon = [ E_x,      E_x,      ... ]
%                [ E_y,      E_y,      ... ]
%                [ Gamma_xy, Gamma_xy, ... ]
%
```

```
%  'A' is an array that specify the coordinates and displacements of
%  an arbitary number of points:
%
%                   coords,   case1,    case2
%            A = [ x1, y1,   ux, uy,   ux, uy,   ... ]
%                [ x2, y2,   ux, uy,   ux, uy,   ... ]
%                  ...       ...       ...       ...
%                [ xn, yn,   ux, uy,   ux, uy,   ... ]
%

%  Written by: Xinyu Huang

nargs = length(varargin) + 1;

if nargs == 2
    mesh_flag = varargin{1};
end

%  Input consistency test

[n_pts, n_cols] = size(A);
if  n_pts < 3
    error('Input array must have at lease 3 rows');
elseif mod(n_cols, 2) ~= 0
    error('Inconsistent data, uneven number of columns in the input array');
elseif n_cols < 4
    error('Input array must have at least 4 columns');
end

n_cases = n_cols/2 - 1;

%  Initialize the output variable
Epsilon = zeros(3, n_cases);

%  Generate triangular mesh
```

```
Tri = delaunay(A(:,1), A(:,2));
[n_elem, n_cols] = size(Tri);

%  Plot mesh
if mesh_flag == 'nomesh'
    % do not plot mesh
else
    triplot(Tri,A);
end

%  Interpolation and integration
area_tot = 0;
for iii = 1 : n_elem

    elemind = Tri(iii,:); x123 = A( elemind, 1 ); y123 = A( elemind, 2 );
    area = 0.5 * det([x123, y123, ones(3,1)]);

    if area < 0     % re-shuffle node ordering
        elemind = elemind([1,3,2]);
        x123 = x123([1,3,2]);
        y123 = y123([1,3,2]);
        area = -area;
    elseif area == 0    % degenerated case, skip this element
        continue;
    end

    % Calculate matrix B
    x456 = 0.5*(x123 + x123([2,3,1]));
    y456 = 0.5*(y123 + y123([2,3,1]));
    px = [x123', x456']; py = [y123', y456'];
    geom = [ones(1,6); px; py; px.^2; px.*py; py.^2];

    if cond(geom) > 10e12
        % mark this triangle
        continue;   % skip it
```

```
end
xc = sum(x123)/3; yc = sum(y123)/3;   % center coordinates

%  solve for the coefficients of the shape functions
%  N_i(x, y) = a(i,1) + a(i,2) * x + a(i,3) * y +
%              a(i,4) x^2 + a(i,5) x y + a(i,6) y^2
aij = eye(6)/geom;

% derivatives of the shape functions evaluated at (xc, yc)
N123x = [ aij(1,2) + 2*aij(1,4)*xc + aij(1,5)*yc;
          aij(2,2) + 2*aij(2,4)*xc + aij(2,5)*yc;
          aij(3,2) + 2*aij(3,4)*xc + aij(3,5)*yc ]';
N456x = [ aij(4,2) + 2*aij(4,4)*xc + aij(4,5)*yc;
          aij(5,2) + 2*aij(5,4)*xc + aij(5,5)*yc;
          aij(6,2) + 2*aij(6,4)*xc + aij(6,5)*yc ]';
N123y = [ aij(1,3) + 2*aij(1,6)*yc + aij(1,5)*xc;
          aij(2,3) + 2*aij(2,6)*yc + aij(2,5)*xc;
          aij(3,3) + 2*aij(3,6)*yc + aij(3,5)*xc ]';
N456y = [ aij(4,3) + 2*aij(4,6)*yc + aij(4,5)*xc;
          aij(5,3) + 2*aij(5,6)*yc + aij(5,5)*xc;
          aij(6,3) + 2*aij(6,6)*yc + aij(6,5)*xc ]';
Nzero = zeros(1,3);

% compose 3 by 12 matrix B
B = [ N123x, Nzero, N456x, Nzero;
      Nzero, N123y, Nzero, N456y;
      N123y, N123x, N456y, N456x ];

%  Integration
area_tot = area_tot + area;

for ic = 1 : n_cases
    du123 = A(elemind, 2*ic+1); du456 = 0.5 * (du123 + du123([2,3,1]));
    dv123 = A(elemind, 2*ic+2); dv456 = 0.5 * (dv123 + dv123([2,3,1]));
    du = [du123; dv123; du456; dv456];
```

```
        Epsilon(:, ic) = Epsilon(:, ic) + area * B * du;
    end
end

Epsilon = Epsilon/area_tot;

%EOF
```

Appendix C

C++ Code to Calculate the Geodesic Fiber Path

The fiber tow on the flange of the MTI candle filter material follow a geodesic path on the curved surface. It is important to figure out the right orientation for each fiber tow in order to build an accurate representation of the reinforcements. Using a conformal mapping scheme, the following code calculate the orientation of fiber tow inside the flange given a number geometric control paramter of the shape of tube flange. The reults is incorporated into the "ligature" model presented in chapter 4. A plot of the calculation result in shown in Figure C.1.

```
//////////////////////////////////////////////////////////////////////
//
// Code to calculate the geodesic fiber path near the flange of the
// candle filter tube
//
// written by: Xinyu Huang
// date:    July 1999
//
```

```
// usage:  modify following variables for different flange geometry:
//
//    double inner_dia = 50.0;
//    double outter_dia = 60.0;
//
//    int num_bands = 56;
//    int num_layers = 19;
//    int num_stacks = 90;
//
// then, recompile and run the code, ouput will be send to the stdout,
// it needs to be redirected because of the large amount of output data
//
////////////////////////////////////////////////////////////////////////////
#include <math.h>
#include <iostream.h>

void map_to_flange(int, double*, double*, double*);

void main(){

  const double pi = 3.1415926535898;

  const double inner_dia = 50.0;
  const double outter_dia = 60.0;
  const int num_bands = 56;
  const int num_layers = 19;
  const int num_stacks = 90;

  int i, j, k, count, length;
  int i_stack, i_layer;
  double ir, or, dr, dtheta, dz;
  double rs, thetas, zs;

  length = num_bands * num_layers * num_stacks;
```

```
double * x = new double[length + 1];
double * y = new double[length + 1];
double * z = new double[length + 1];
int * nn = new int[length + 1];

ir = inner_dia/2;
or = outter_dia/2;
dr = (or - ir)/num_layers;
dz = 2.9288;

dtheta = 2.0*pi/num_bands;

count = 0;
zs = 0;
for(i=0; i<num_stacks; i++)
{
  rs = ir;
  i_stack = i*2000;
  for(j=0; j<num_layers; j++)
  {
    thetas = 0;
    i_layer = j*100;
    for(k=0; k<num_bands; k++)
    {
      nn[count] = i_stack + i_layer + k + 1;
      x[count] = rs * cos(thetas);
      y[count] = rs * sin(thetas);
      z[count] = zs;

      count++;

      thetas = thetas + dtheta;
    }

    rs = rs + dr;
```

```
    }

    zs = zs + dz;
  }

  map_to_flange(count, x, y, z);

  //output
  for(i=0; i<count; i++)
  {
    cout.setf(ios::scientific, ios::floatfield);
    cout<<nn[i]<<", "<<x[i]<<", "<<y[i]<<", "<<z[i]<<endl;
  }

  delete[] x;
  delete[] y;
  delete[] z;
  delete[] nn;
}

/*****************************************************************/
void map_to_flange(int nnn, double* xi, double* yi, double* zi)
//
//************ old interface definition *************//
//    (TowPtr layer, double ir1, double or1,
//       double ir2, double or2, double r2,
//       double filet_r1, double filet_r2)
//
{
  double ir1, or1, ir2, or2, r2, filet_r1, filet_r2;

  ir1 = 64.0/2;
  or1 = 74.0/2;
  ir2 = 50.0/2;
  or2 = 60.0/2;
```

```
r2 = 40.0;
filet_r1 = 10.0;
filet_r2 = 10.0;

double thick, r1, r, xp, zp, xq, zq;
double arc_st, arc_tu, arc_uv, arc_vw;

thick = or2 - ir2;
r1 = r2 - thick;
r = ir2 + thick/2.;

xp = ir1 - filet_r1;
zp = sqrt(r1*r1 - ir1*ir1 - 2*(r1 - ir1)*filet_r1);

xq = or2 + filet_r2;
zq = sqrt(r2*r2 - or2*or2 + 2*(r2 - or2)*filet_r2);

arc_st = zp;
arc_tu = (filet_r1 + thick/2)*atan(zp/xp);
arc_uv = (r1 + thick/2)*(atan(zq/xq) - atan(zp/xp));
arc_vw = (filet_r2 + thick/2)*atan(zq/xq);

//find mapping point in cylindrical coordinates;

double x, y, z;
double rr, phiphi, zz;
double xmap, ymap, zmap;

int iii;
for(iii=0; iii<nnn; iii++){

    x = xi[iii];
    y = yi[iii];
    z = zi[iii];
```

```
phiphi = atan2(x, y);

x = sqrt(x*x + y*y) - r;
y = 0.0;

if(z>=0 && z<zp)
  rr = r + x + ir1 -ir2;
else if(z>=zp && z<(arc_st + arc_tu))
  rr = (filet_r1 + thick/2 + x)*cos((z-zp)/(filet_r1 +
    thick/2)) + xp;
else if(z>=(arc_st + arc_tu) && z<(arc_st + arc_tu + arc_uv))
  rr = (r1 + thick/2 + x)*cos((z - arc_st - arc_tu)/(r1 +
    thick/2) + atan2(zp,xp));
else if(z >= (arc_st + arc_tu + arc_uv) &&
    z < (arc_st + arc_tu + arc_uv + arc_vw))
  rr = xq - (filet_r2 + thick/2 - x)*cos(atan2(zq,xq) -
    (z - arc_st - arc_tu - arc_uv)/(filet_r2 + thick/2));
else
  rr = r + x;

if(z>=0 && z<zp)
  zz = z;
else if(z>=zp && z<(arc_st + arc_tu))
  zz = (filet_r1 + thick/2 + x)*sin((z - zp)/(filet_r1 +
  thick/2)) + zp;
else if(z>=(arc_st + arc_tu) && z<(arc_st + arc_tu + arc_uv))
  zz = (r1 + thick/2 + x)*sin((z-arc_st-arc_tu)/(r1 + thick/2)
    + atan2(zp,xp));
else if(z >= (arc_st + arc_tu + arc_uv) &&
    z < (arc_st + arc_tu + arc_uv + arc_vw))
  zz = zq - (filet_r2 + thick/2 - x)*sin(atan2(zq,xq) -
    (z - arc_st - arc_tu - arc_uv)/(filet_r2 + thick/2));
else
  zz = zq + z - (arc_st + arc_tu + arc_uv + arc_vw);
```

```
      //phiphi = y/r;

      xmap = rr*cos(phiphi);
      ymap = rr*sin(phiphi);
      zmap = zz;

      xi[iii] = xmap;
      yi[iii] = ymap;
      zi[iii] = zmap;

  }
}
/*****************************************************************/
```

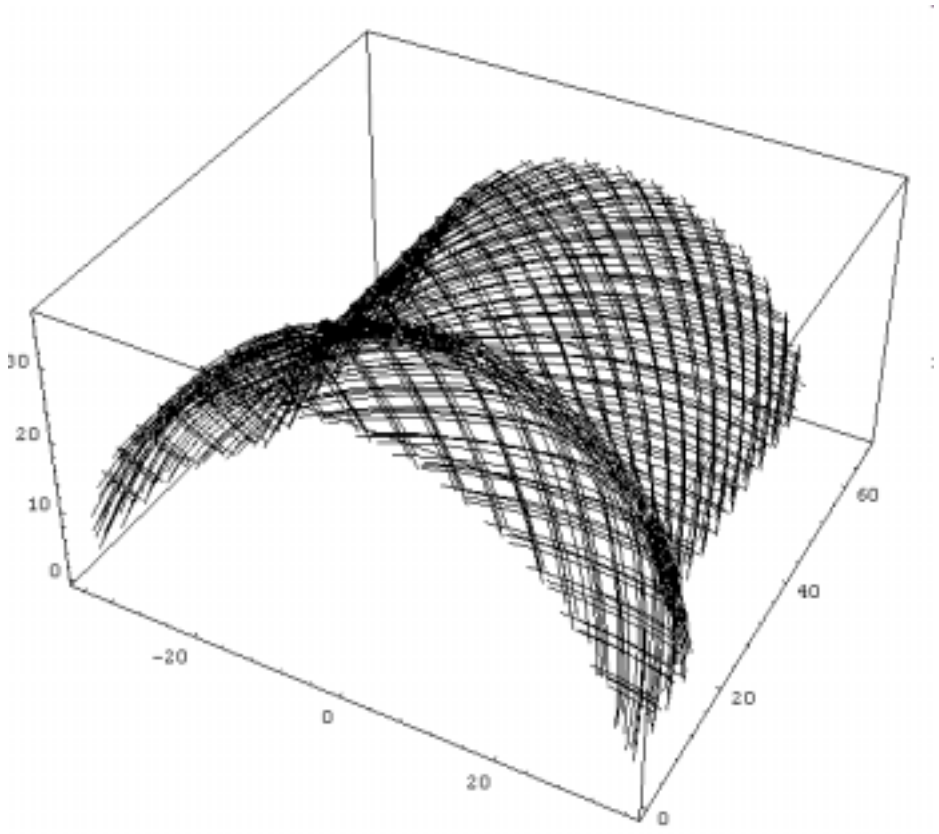

Figure C.1: Geodesic fiber path calculated by the code.

Appendix D

Vita

Xinyu Huang was born on April 1st 1972 in Tianjin China, the second child to Guozhu Huang and Xiujuan Chen. He grew up in a northern suburb of the city. After graduation from Tianjin No. 1 high school in 1987, he attended Beijing University of Aeronautics and Astronautics (BUAA). In 1993, he received his BS degree in aircraft design and applied mechanics. Then he joined the Institute of Solid Mechanics of BUAA, doing research on fatigue and fracture of aircraft structural components, at the same time taking graduate level courses in mathematics and mechanics. In 1996, he joined the department of Engineering Science and Mechanics of Virginia Polytechnic Institute and State University pursuing a PhD degree in applied mechanics.